ACOUSTOPHORESIS OF MICROPARTICLES AND CELLS IN MICROFLUIDIC DEVICES

A Dissertation

by

ZHONGZHENG LIU

Submitted to the Office of Graduate and Professional Studies of
Texas A&M University
in partial fulfillment of the requirements for the degree of

DOCTOR OF PHILOSOPHY

Chair of Committee,	Yong-Joe Kim
Committee Members,	Arum Han
	Luis San Andrés
	Hamm-Ching Chen
Head of Department,	Andreas A. Polycarpou

August 2016

Major Subject: Mechanical Engineering

ABSTRACT

Microfluidic acoustophoresis is a nonlinear acoustic phenomenon that can induce the motion of microparticles or cells under acoustic excitations in microfluidic devices. Existing acoustophoresis models, that are derived for “static” fluid media with “uniform” temperature distributions, have been mainly used for the design of acoustophoretic microfluidic devices. Therefore, it has been challenging to consider the effects of “moving” fluid media and spatial fluid medium temperature variation that significantly affect the acoustophoretic motion in a real microfluidic device. Here, it is proposed to develop a numerical modeling method that includes the effects of the moving fluid media and the temperature variation. Through the modeling analyses using the proposed numerical method, it was shown that the fluid medium flow and the temperature variation affected the acoustophoretic forces and the acoustic streaming significantly.

Around the cells or miroparticles, the acoustophoretic forces and acoustic streaming velocities induced by an ultrasonic excitation are of great interest in an extensive range of biomedical and mechanical applications. However, conventional methods to calculate the acoustic streaming require expensive computational costs and are inaccurate in the farfield of the cells or microparticles. A new analytical algorithm is proposed to significantly improve computational efficiency as well as computational accuracy in the farfield. The proposed algorithm is validated by comparing the results of the proposed method against those of a traditional method.

Based on the developed numerical and analytical modelling approaches, the following three applications have been investigated in this thesis.

1) The frequency responses of the acoustophoretic forces and acoustic streaming around the cells or microparticles were calculated and then the resonance frequencies were identified at the local maxima of the acoustic streaming velocities.

2) The trajectories of the cells or microparticles were analyzed by using the proposed modelling approach. By fitting experimental trajectories into the predicted one, the mechanical properties of the cells could be identified.

3) Based on the proposed modeling approach, a novel separation device design was proposed to separate the cells or microparticles depending on their subtle compressibility differences. The device consists of two stages where cells/microparticles are first aligned in the center of the microchannel and then separated depending on their subtle compressibility differences.

ACKNOWLEDGMENTS

I would like to express my deep gratitude to my advisor, Prof. Yong-Joe Kim, for his excellent guidance and encouragement on my research and study at the Acoustics and Signal Processing Laboratory of Texas A&M University. I would like to thank my committee members, Prof. Luis San Andrés, Prof. Arum Han, and Prof. Hamm-Ching Chen for their valuable suggestions and comments on my dissertation work.

Thanks also go to my friends and colleagues for making my time at Texas A&M University a great experience.

TABLE OF CONTENTS

Page

Page

Page

Page

LIST OF FIGURES

FIGURE Page

FIGURE Page

FIGURE Page

LIST OF TABLES

1. INTRODUCTION

1.1. Background on Label-Free, Acoustophoretic Cell/Microparticle Separation

It has been of great interest to separate cells and microparticles in the broad areas of industrial, chemical, and biomedical applications such as polymer particle manufacturing, developing drug delivery/encapsulated particles, and separating blood cells or rare cells (e.g., circulating tumor cells).[1-4] In recent years, label-free separations of different cells/microparticles based on their physical properties (e.g., size, compressibility, density, and electrical polarization) have gained significant interest since they do not require the tagging of samples with labels (e.g., fluorescent, magnetic, and radioactive labels).[5-7] These label-free separation methods can significantly reduce the cost and time associated with cumbersome sample preparation steps. For label-free separations, various different forces such as dielectrophoretic, magnetophoretic, and inertia forces, as well as simple mechanical sieving methods have been utilized. Dielectrophoretic separation utilizes differences in induced dielectric properties of cells under a non-uniform electric field and magnetophoretic separation is based on differences in the intrinsic magnetic properties of cells.[5-8] Inertia-force-based separation utilizes differences in entrance/transit time when cells/microparticles flow into narrow microstructures.[9,10] Simple microstructures have been also utilized in separating particles or cells based on their sizes, such as the case of deterministic lateral displacement.[11] However, these separation modalities have several drawbacks, such as low throughput, limited specificity, weak force, complicated microstructures, or need for

expensive instrumentation.

Label-free, acoustophoretic, microfluidic separation has drawn significant interest in the past few years due to its unique capabilities of separating cells and microparticles based on their vibro-acoustic properties with simple microfluidic structures and piezoelectric actuators. A microparticle in an acoustic standing wave generated by a resonant acoustic excitation experiences the acoustophoretic force that moves the microparticle either to the acoustic pressure nodes (*i.e.*, area of minimum pressure amplitude) or anti-nodes (*i.e.*, area of maximum pressure amplitude) of the standing wave depending on the physical properties of both the fluid medium and the microparticle. This principle has been used in microfluidic systems to separate cells and microparticles of different physical properties.[12-16] The acoustophoretic force generated by the resonant acoustic excitation is generally strong enough to be applied to the cell- or microparticle-suspended fluid medium "moving" at a relatively high speed. Also, the acoustic resonant excitation requires relatively low power consumption.[15] Therefore, this separation method can offer a continuous, high-throughput, high-efficient, and label-free separation.

The acoustophoresis phenomenon can be observed not only in a microchannel under a resonant acoustic excitation, but also around a cell/microparticle excited by an acoustic wave. If small particles distributed randomly around the cells/microparticles submerged in a fluid medium with an acoustic excitation are much smaller than the cells/microparticles, they are observed to be attracted to the surface of these cells/microparticles or repelled away from them[93-97] depending on the properties of both

the small particles and the cells/microparticles. This acoustophoresis can also provide a novel way to identify the vibro-acoustic properties of different cells/microparticles, which will be presented in this thesis.

1.2. Acoustophoresis in Microchannel and Around Cells/Microparticles

Due to the aforementioned advantages of the cell/microparticle separation based on the acoustophoresis, the acoustophoresis can be applied to various industrial, chemical, and biomedical applications. However, the theoretical investigation of the acoustophoresis has been limited to simplistic models. Thus, the long-term objective of this research are to investigate the acoustophoresis in the microchannels and around cells/microparticles by developing theoretical modeling approaches and to experimentally validate the theoretical approaches.

1.2.1. Acoustophoresis in Microchannels

The acoustophoretic force applied on microparticles in inviscid, static fluid media has been studied by King, Yosioka and Kawasima, Gorkov, Nyborg, and others.[17-22] The acoustophoretic force applied on spherical "rigid" microparticles was first studied by King.[17] Later, the integral form of the acoustophoretic force applied on spherical "compressible" microparticles was derived by Yosioka and Kawasima.[18] Gorkov[19] derived the simple derivative form of the three-dimensional (3-D) acoustophoretic force for compressible microparticles, presented in Eq. (1.1) below. Nyborg[20] also derived the acoustophoretic force on a rigid microparticle using a procedure similar to King's. Doinikov[23,24] utilized the spatial Fourier transformation in spherical coordinates for the research of acoustophoretic force on a compressible microparticles in a viscous fluid

medium, although this procedure required much more computational cost compared with the other procedures presented in Refs. [17-22].

Among these acoustophoretic force models, the acoustophoretic force equation derived by Gorkov in a three-dimensional (3-D), static, inviscid fluid medium has been widely used to design acoustophoretic, microfluidic separation devices. This 3-D analytical model[19] is represented as

$$\mathbf{F}_a = -V_p \nabla \left[\left(1 - \frac{\beta_p}{\beta_0} \right) \frac{1}{2\rho_0 c_0^2} \left\langle p_1^2 \right\rangle - \frac{3\left(\rho_p - \rho_0\right)}{2\left(2\rho_p + \rho_0\right)} \rho_0 \left\langle \mathbf{v}_1 \cdot \mathbf{v}_1 \right\rangle \right], \tag{1.1}$$

where $\langle\ \rangle$ means the time-averaging of an inner variable over one period from 0 to $2\pi/\omega$, and ω is the excitation angular frequency. In Eq. (1.1), c_0 is the sound speed in the fluid medium, ρ_0 and ρ_p are the densities of the fluid medium and microparticle, respectively, β_0 and β_p are the corresponding compressibilities, p_1 is the first-order acoustic pressure, $\mathbf{v}_1$ is the first-order acoustic particle velocity, and V_p is the microparticle's volume.

Eq. (1.1) is valid under the assumption that the microparticle radius is much larger than the acoustic diffusion length or viscous boundary layer thickness δ[24,25], represented as

$$\delta = \sqrt{\frac{2\eta}{\rho_0 \omega}}, \tag{1.2}$$

where η is the dynamic viscosity of the fluid medium. If the microparticle size is in the same order of magnitude as the acoustic diffusion length, the effects of fluid viscosity cannot be ignored and the equation modified by Settnes and Bruus[25] should be applied in place of Eq. (1.1).

In a one-dimensional (1-D), acoustic standing wave with an inviscid, static fluid medium, Eq. (1.1) can be simplified as[15,26]

$$F_a = -\left(\frac{\pi P_a^2 V_p \beta_0}{2\lambda}\right)\xi(\beta,\rho)\sin(2kx), \tag{1.3a}$$

$$\xi = \frac{5\rho_p - 2\rho_0}{2\rho_p + \rho_0} - \frac{\beta_p}{\beta_0}, \tag{1.3b}$$

where P_a is the first-order acoustic pressure amplitude of the resonant standing wave, λ is the wavelength, k is the wavenumber defined as $k = 2\pi/\lambda$, and x is the shortest distance from an acoustic pressure node.

The acoustophoretic force is calculated from the linear acoustic fields, inside the microchannel, which can be calculated based on the four nonlinear governing equations: the Mass, Momentum, and Energy Conservation Equations and the State Equation. The acoustic pressure and velocity fields calculated by using these nonlinear equations have both linear and nonlinear components. By taking a time-averaging of the resulting acoustic particle velocity, its linear components are then cancelled out due to its sinusoidal fluctuation, resulting in the nonlinear, steady, constant fluid flow, which is referred to as the "acoustic streaming".[27, 28]

In the microchannel, the acoustic streaming is driven by the viscous boundary layer due to the friction between the boundary (e.g., rigid or oscillating wall) and the fluid medium. In this case, a viscous acoustic layer is generated in the vicinity of the boundary, which can divide the fluid inside the boundary as the inner boundary layer and outside, as the outer boundary layer. Then, the acoustic streaming in the inner boundary

is known as “Schlichting streaming”, and outer boundary streaming is referred to as “Rayleigh streaming”,[29] which is illustrated in Fig. 1.1.

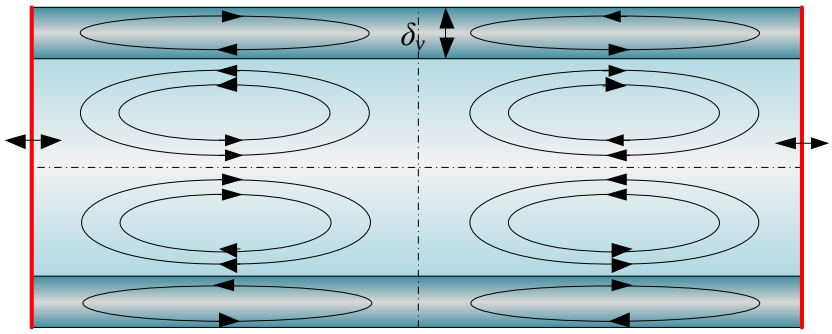

Fig. 1.1: Inner (Schlichting) streaming within viscous acoustic boundary layer of thickness δ (dark blue areas) and outer (Rayleigh) streaming vortices (light blue area) in microchannel. The vertical red lines represent the oscillating boundaries.

The acoustic streaming inside a microfluidic device has been studied for decades. As for the streaming inside a 2-D microchannel, Rayleigh studied the acoustic streaming of incompressible fluid medium between two parallel plates analytically in 1884,[30] and he mainly considered the streaming outside the viscous boundary layer (*i.e.*, the outer streaming). Then, Schilichting[31] investigated the streaming inside the viscous boundary layer (*i.e.*, the inner streaming). Westervelt[32] derived a vorticity equation and solved it to analyze the Rayleigh streaming. Nyborg[33] presented a series of theoretical investigation on the acoustic streaming, as well as provided examples of the boundary layer driven streaming between two parallel plates. In his work, the acoustic particle velocity was separated into both irrotational and divergence-free components. Hamilton[34] derived an analytical expression of the acoustic streaming generated by

standing waves in two-dimensional (2-D) channels and investigated later the effects of temperature on the acoustic streaming[35]. Based on the previous results of the acoustic streaming between parallel plates of infinite length, Muller[36] decomposed the streaming velocity into viscous component, inviscid particular component, and inviscid homogeneous component based on the viscous boundary layer and then derived a simple approximate analytical expression, of the acoustic streaming in the cross-section of a rectangular microchannel, that can be programmed for the fast computation of the streaming.

One major limiting factor with the analytical acoustophoretic force and acoustic streaming calculations is that they are based on the assumption of an acoustic field in an inviscid, "static" fluid medium. When there is a fluid medium flow, the effects of the flow need to be taken into consideration. The viscous boundary layers generated from no-slip conditions on the walls of a microfluidic device make microparticles move at different velocities depending on their positions relative to the wall. For example, a microparticle initially placed close to the wall of the device moves much slower than one placed in the middle due to the viscous boundary layer. This motion cannot be accurately evaluated by using the analytical model. Thus, the analytical model can be too simplistic to predict important physical phenomena such as the effects of the moving fluid media and viscous boundary layers.

2-D or 3-D modeling approaches for analyzing acoustophoretic phenomena in static fluid media have been previously reported in Refs. [19, 25, 26, 37]. However, in these models, the effects of the medium flow and the local temperature elevation

induced by piezoelectric actuators were not considered. For example, Hagsäter et al.[26, 37] performed a 2-D numerical analysis based on a modal approach in a microfluidic channel with a static fluid medium to obtain first-order, "linear" acoustic pressure and particle velocity distributions. Settnes and Bruus[25] presented a 3-D time-averaged acoustophoretic force model in a static, viscous fluid medium based on the work of Gorkov.

To estimate the effects of fluid medium flow and temperature variation on the acosutophoretic force and acoustic streaming, the acoustic governing equation are decomposed using a perturbation method. Then, the decomposed equations are solved by using quadratic mapping functions and a second-order finite difference method (FDM)[38] along with appropriate boundary and excitation conditions. The fluid medium flow and temperature distributions in a microfluidic device are proposed to be analyzed from the zeroth-order governing equations. The zeroth-order fluid medium flow and temperature solutions are then substituted into the first- and second-order governing equations. Thus, the effects of the zeroth-order variables can be considered in the higher-order equations. The acoustophoretic force applied to the microparticle is then calculated by substituting the first-order solutions obtained from the previous step into the Gorkov's Equation. The Newton's Equation of Motion is then solved by applying the fourth-order Runge-Kutta method[38] to obtain the position and velocity of the microparticle numerically when the acoustophoretic force, viscous drag force, and buoyancy and gravitational forces are applied to the microparticle. In this calculation step, the fluid medium and acoustic streaming velocities are also taken into account in

the viscous drag force term.

The proposed numerical modeling procedure has several advantages over existing analytical and numerical approaches. First, by using the mapping functions, the acoustic pressure and particle velocity fields in microfluidic devices of any shapes can be numerically predicted. Thus, the effects of 2-D or 3-D geometries including 2-D or 3-D acoustic fields can be easily considered. Second, the effects of the fluid medium flow on the acoustophoretic force and the acoustic streaming are included in the proposed numerical model. The effects of the fluid medium flow on the acoustophoretic motion can then be analyzed, resulting in an accurate prediction of the microparticle motion. Although Muller et al.[39] recently described that the acoustic streaming could be included in their modeling procedure implemented in a commercial software package, COMSOL Multiphysics®, they included only a static fluid medium condition. Lastly, the zeroth-order temperature is proposed to be calculated to study the effects of the heat generated by piezoelectric actuators on the first- and second-order acoustic fields.

1.2.2. Acoustophoresis Around Cells/Microparticles

The surface of a cell/microparticle oscillates in response to incident excitation waves depending on the properties of the incident wave and the cell/microparticle. The oscillation of the fluid medium consists of linear and nonlinear components. In Fig. 1.2, the scattered and transmitted waves are the linear components and can be calculated based on the properties of both the incident wave and particle. Then, due to the interaction of these linear waves, the time-averaged, “nonlinear” oscillation of the fluid medium, i.e., the acoustic streaming, can be further developed.

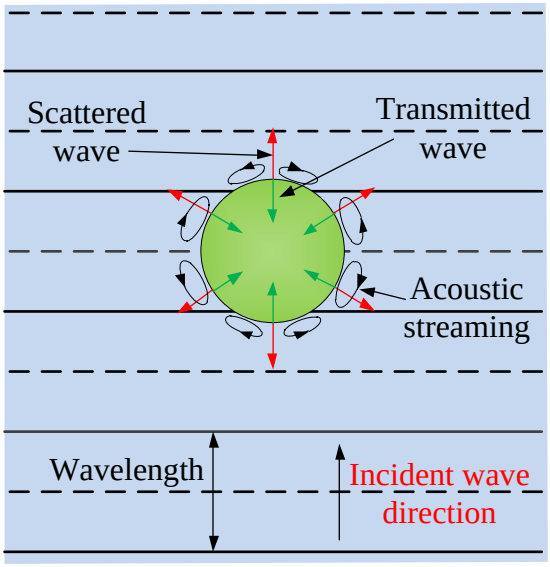

Fig. 1.2: Linear and nonlinear acoustic fields in planar ultrasonic wave. The scattered and transmitted waves are linear components, and the acoustic streaming velocities are nonlinear components.

In the past decades, there have been various models to describe the linear oscillatory behaviors of cells/microparticles under an acoustic excitation. The simplest model proposed by Lamb[40] is to analyze the oscillation of an inviscid droplet in an inviscid fluid medium under an acoustic excitation. Later, Ackerman[41-43] conducted a series of work to study the resonance phenomenon of cells in acoustic wave excitations by modeling a cell as a "rigid shell" filled with an incompressible fluid. Then, Reid[44] and Miller[45] investigated the oscillations of a viscous droplet in a viscous fluid medium. Evan studied the viscoelasticity of cell membranes in his papers[46, 47] and book[48]. Based on the Evan's work, Zinin[49, 50] proposed a cell model of a viscoelastic membrane with a compressible fluid medium inside, and analyzed the effects of cell parameters at its resonance frequencies. From a different perspective of view, Ford[51] modelled a

bacterium as an inviscid droplet, as proposed originally by Lamb[40] and a solid elastic particle by Pao & Mow[52] and compared the estimated resonance frequencies of both the models. Rodriguez et al.[53] gave a review on experimental and modeling approaches for the analyses of cell mechanics.

From the work done by these precursors, it is a good approximation to model a cell as a membrane enclosing a compressible fluid medium (fluid model)[49-51] or a simple solid elastic microparticle (solid model)[51, 52]. In previous studies, both the models are proposed to predict the resonant frequencies of cells or bacterium. For the membrane model, Zinin[49, 50] studied the effects of each of the surface tension and the surface compression and shear moduli on the resonance frequencies, while the coupling effects of these parameters were not considered. From the study presented in Chap. 4, it is shown that these parameters are coupled to create new resonance frequencies that are not equal to the resonance frequencies predicted by using the individual parameters.

Based on the linear oscillation of the fluid medium, the acoustic streaming can be calculated around the cell/microparticle. However, the computation of the acoustic streaming has been a challenging problem and investigated for more than a half century.

Raney *et al.*[54] and Holtsmark *et al.*[55] studied the acoustic streaming generated around an infinite-length cylinder under an acoustic wave excitation. Later, Lane[56] modified the Holtsmark's approach to be applied for the calculation of the acoustic streaming generated around a sphere. In this work, a vorticity equation in an incompressible viscous fluid medium was decomposed by using a perturbation method and then solved by assuming an acoustic streaming solution similar to a flow streamline

function under the spherical axisymmetric condition. Nyborg[33] developed a general method to calculate the acoustic streaming near an arbitrarily-shaped boundary with the assumption of the thin acoustic boundary layer. Wang[57] analyzed the acoustic streaming after decomposing it into inner and outer ones of an acoustic boundary layer generated on a sphere. Riley[58] also calculated the inner and outer streaming around a sphere from the vorticity equation. Lee and Wang applied the Nyborg's method for the calculation of the acoustic streaming pattern, near a small sphere, induced by two orthogonal standing waves at a single frequency.[59] They also applied the same method to calculate the outer streaming around a sphere placed between the pressure node and antinode of a single standing wave.[60] Later, Sadhal *et al*.[61, 62] studied the acoustic streaming around a droplet, a gas bubble, and a solid elastic particle. All the aforementioned approaches for the calculation of the acoustic streaming around a spherical object were based on the assumption that the object is smaller than the excitation wavelength, which makes it possible to obtain the analytical expression of the acoustic streaming.

Doinikov[23] proposed a method to solve the acoustic streaming around a particle of arbitrary size. In this method, the spherical Bessel Functions were used to decompose the governing equation based on the orders of the spherical Bessel Functions and then each decomposed equation was solved independently. The accuracy of this solution approach depends on the total number of the orders involved. By using this method, the acoustic streaming around a gas bubble and an encapsulated particle were investigated.[63, 64] Although this method is powerful, enabling the calculation of the

acoustic streaming around the particle of arbitrary size, it requires a long computational time and its results are not accurate in the farfield of solid particles and liquid droplets as discussed in Chap. 5.

Here, the Doinikov's approach has been improved by decomposing the acoustic streaming into compressional and shear components depending on the inside and outside the viscous boundary layer around a microparticle of arbitrary size to accurately and computationally efficiently calculate the acoustic streaming. Then, the governing equations of the acoustic streaming are decomposed into the homogenous and particular ones for the calculation of the compressional and shear components, respectively. The decomposed governing equations are then solved separately. The total acoustic streaming is then obtained by combining both the compressional and shear components.

Since the acoustic streaming induced by a cell/microparticle is strongly correlated to the properties of the cell/microparticle, it is expected that the mechanical properties of the cells/microparticles can be identified by measuring the acoustic streaming velocities around the cell/microparticle and matching the experiment results with the modeling ones.

1.3. Applications of Proposed Acoustophoresis Modeling Approaches

The proposed acoustophoresis modeling approaches can be applied to a wide range of industrial and laboratory applications. In this dissertation, three novel applications are investigated as follows: (1) Identification of the resonance frequencies of cells/microparticles, (2) Identification of the density and compressibility of cells/microparticles, and (3) Novel design of a microfluidic device for the label-free,

high-throughput, high-resolution separation of cells/microparticles with subtle property differences. These three applications are discussed below in detail.

1.3.1 Identification of Resonant Frequencies of Cells/Microparticles

The resonance frequencies of cells/microparticles are important intrinsic mechanical properties and can be used to distinguish different cells/microparticles. In addition, since the resonance frequencies of cells/microparticles are strongly correlated to their mechanical properties, these frequencies can then be used to calculate the mechanical properties.

Ackerman measured the first resonance frequency of erythrocytes by exciting these cells with a range of different frequencies.[43] In this experiment, the number of dead cells were counted and the frequency coincident to the maximum death count was identified as the resonance frequency of the erythrocytes. This method requires a lot of experimental data, at all the excitation frequencies, which makes the count of the death cells challenging. Marston and Apfel applied an optical interferometry to measure the deformation of a xylene droplet to determine its resonance frequencies.[65, 66] This approach can only be used to identify the first resonant frequency of liquid droplet and gas bubble. Additionally, this individual droplet measurement approach requires high costs to test a large number of samples. By using an Atomic Force Microscope (AFM), Pelling et al.[67] and Jelinek et al.[68] measured the resonance frequencies of yeast cells. In this approach, the force applied by the sharp AFM tip on the cell surface and the local deformation at the contact point can modify the actual resonance frequencies of the cells. Similar to the measurement using the optical interferometry, the AFM measurement is

also expensive and slow with a large number of samples since it requires the labor intensive alignment of the AFM tip on the individual cell.

Here, a novel method to measure the resonance frequencies of cells/microparticles with no mechanical contact is proposed. By using the proposed model to analyze the acoustophoresis around cells/microparticles, it is shown that the resonance frequencies of the cells/microparticles can be identified at excitation frequencies where the acoustic streaming velocities around the cells/microparticles are maximized. The maximum acoustic streaming velocities can be measured by using a relatively inexpensive microscope along with an inexpensive video camera. Unlike the optical interferometry or AFM based measurements, this method does not require precise alignment of the equipment to individual cells/microparticles, which can make possible to test a large number of samples relatively faster than the existing approaches. In addition, it requires no mechanical contact, making it possible to measure accurate resonance frequencies.

1.3.2 Identification of Density and Compressibility of Cells/Microparticles

The density, compressibility, size of cells/microparticles are important mechanical properties in various industries and research fields. For example, in polymer manufacturing, the density of polymer particles is a crucial factor to identify the porosity of the polymer particles. In chemical or biomedical engineering fields, various cells/microparticles can be separated based on their mechanical properties. As for human health, for example, the compressibility of cancer cells can be an important biomarker, potentially indicating the metastasis of the cells.

In order to identify the mechanical properties of cells/microparticles, conventional

methods use mechanical (e.g., AFM[69, 92] and micropipette aspiration[70, 92]), optical (e.g., optical tweezer[71, 92]), or magnetic (e.g., magnetic twisting cytometry[72, 92]) forces to cause mechanical deformation to the cells/microparticles. Then, such deformations are measured to characterize the mechanical properties. However, these methods require laborious operations and expertise and are thus inherently low throughput and not suitable for diagnosis.

Based on the microfluidic acoustophoresis technique, it is possible to measure the density and compressibility of cells without a mechanical contact at high throughput by tracking the cell's acoustophoretic movement in acoustic fields. Currently, only few researchers have investigated the measurement of cell/microparticle's properties using the acoustophoresis. Weiser and Apfel[73] used an acoustic levitation force, which is the acoustophoretic force applied on a microparticle in balance with its gravity force, to calculate the compressibility of the microparticle. Hartono[74] extracted the compressibility of polystyrene (PS) beads and various benign and cancer cells by matching the recorded trajectories of the cells/microparticles with the trajectories predicted by using a "1-D" analytical model in a microchannel. However, in these two methods, the cell density was assumed as a value reported in other reference papers to extract the compressibility, which may cause large compressibility variations since the density was not measured directly from the samples. Barnkob[75] successfully applied an micro Particle Image Velocimetry (PIV) to measure the local acoustic pressure in a microchannel under an acoustic excitation. Later, Barnkob[76]] investigated the calibration of acoustic fields in a "2-D" microchannel using PS beads and melamine

resin particles and then the extraction of cell/microparticle's density and compressibility simultaneously from the recorded acoustophoretic motion of the cells/microparticles. However, the expensive micro-PIV equipment used for calibrating acoustic pressures limits the wide applications of this approach.

In addition to the drawbacks of the aforementioned methods in their applications, they cannot be used to consider the effects of both channel walls and acoustic streaming on the motion of cells/microparticles. In reality, the acoustic streaming has significant effects on the motion of cells/microparticles, in particular, under the high level acoustic resonance excitation. Besides, it has been observed that as the cells/microparticles approach the channel walls closely, the motion of the cells/microparticles gets slower due to the viscous drag force induced by the walls, which is referred to as the wall effects[86].

Here, a novel acoustophoresis based method including the wall effects and the acoustic streaming for the accurate identification of the mechanical properties of cells/microparticles is proposed. In addition, the motion of cells/microparticles in both the vertical and horizontal directions is considered so that the density and compressibility of cells can be identified simultaneously in microchannels. In the proposed method, a multi-frequency excitation is also utilized to levitate the cells/microparticles to the middle plane of the microchannel in the vertical direction before the cells/microparticles start to move to pressure nodal lines. Therefore, the initial vertical locations of cells/microparticles are controlled to be at the middle of the microchannel depth, which significantly improves the accuracy of the density

estimation.

The proposed method to accurately measure the density and compressibility of the cells/microparticles has several advantages over existing approaches. First, the acoustic streaming and the wall effects are considered in predicting the motion of the cells/microparticles, which can significantly improve the identification accuracy. Second, the multi-frequency excitation is used to align the cells at the known initial positions so that the density can be accurately estimated. Third, the experimental setup for the proposed procedure is simpler than the previous ones (e.g., one with the expensive micro-PIV), significantly reducing the experimental cost.

1.3.3. Novel Design of Microfluidic Separation Device

It has gained significant attention to separate the cancer cells based on their subtle mechanical property differences without tagging labels at high throughput. Thus, it is of great interest to develop a microfluidic device to conduct continuous, high-throughput, label-free, mechanical-property-based microparticle/cell separation. By using the acoustophoresis phenomena, various microfluidic devices have been proposed and used for the conduction of separation experiments.[12-16] However, the separation resolution of these devices is generally not high enough to separate the cells/microparticles with subtle mechanical property differences.

Here, a novel, acoustophoretic, microfluidic device is proposed to conduct the continuous, high-throughput, label-free separation of the cells/microparticles depending on their subtle mechanical property differences. In an acoustophoretic, microfluidic channel, there are two main force applied to the cells/microparticles inside the channel:

i.e., the acoustophoretic force induced by the resonant acoustic excitation and the viscous drag force caused by the fluid medium flow. Then, the final position of acoustically-excited cells/microparticles is determined where both the acoustophoretic force and the viscous drag force are in balance. The basic idea to realize the high-resolution separation device is then to split the main fluid medium flow into two right angled flow streams with a large flow speed difference. Then, the viscous drag force has a large gradient in the separation area. Thus, a small acoustophoretic force difference induced by the subtle mechanical property difference makes the resultant force applied to the cells/microparticles in balance at one of the two flow streams.

In this device, the main working channel consists of a focus segment and a separation segment. When the cells/microparticles flow into the main channel, they are first aligned in the middle of the channel inside the focus segment and then separated in the following segment. By using a numerical model, the dimensions of the microchannel are further optimized for given cell/microparticle properties. Therefore, the separation performance in terms of separation resolution and accuracy is improved significantly by using the innovative design idea and the optimization. In Chap. 7, the optimization of the designed device is presented. The performance of the optimally designed microchannel is then investigated experimentally.

1.4. Brief Overview of Chapters

In Chap. 2, the general acoustic governing equations are briefly presented. By applying a perturbation method to the governing equations, the perturbed governing equations for the calculation of both the linear acoustic fields and the nonlinear acoustic

streaming are then derived.

In Chap. 3, a numerical solution approach using a second-order Finite Difference Method (FDM) is presented to solve the perturbed governing equations. Once the linear acoustic fields and the nonlinear acoustic streaming are calculated from the perturbed governing equations, a fourth-order Runge-Kutta method is applied to these solutions to analyze the acoustophoretic motion of a cell/microparticle suspended in a "moving" viscous fluid medium with spatially distributed temperature inside the microchannel.

In Chap. 4, the cells/microparticles are modelled as fluid and solid spheres in a planar acoustic wave. The frequency responses of the acoustic pressure scattered around these models are investigated in this chapter.

In Chap. 5, the acoustophoretic force and acoustic streaming induced by a spherical cell/particle when excited by a plane wave is derived. Based on the linear acoustic solutions derived in Chap. 4, the frequency responses of the acoustophoretic force and streaming are studied.

In Chap. 6, the acoustophoretic motion of cells/microparticles is predicted by using the proposed modeling approach. By fitting the experimental trajectories to the predicted ones, the density and compressibility of the cells/microparticles are identified. In particular, the mechanical properties, of breast, head, and neck cancer cells, identified by using the proposed method are presented in this chapter.

In Chap. 7, a novel design of the continuous, label-free, high-throughput microparticle separation device is proposed. Then, the dimensions of the proposed device are numerically optimized. The separation performance of the optimally

designed devoice is then tested experimentally.

2. GOVERNING EQUATIONS OF ACOUSTOPHORESIS IN MICROFLUIDIC CHANNELS

Acoustophoresis is a nonlinear acoustic phenomenon that induces a microparticle/cell under an acoustic wave excitation to move from one location to other and that consists of both acoustophoretic force and acoustic streaming. The basic governing equations for analysing the acoustophoresis are the Mass, Momentum, and Energy Conservation Equations and the State Equation. By using a perturbation method, these nonlinear governing equations are decomposed into a series of equations in the different orders of magnitude. Then, the decomposed equations up to the second-order one that is high enough to accurately analyze the acoustophoresis in microfluidic channels are considered in this thesis.

From the decomposed equations, the acoustophoretic force applied on a microparticle as well as the acoustic streaming can be derived and analysed. In this thesis, the harmonic excitation at a single frequency is considered and only steady state solution is of interests since the transient solution in the beginning of an acoustic excitation is so short that its effects on the acoustophoretic motion can be ignored.

2.1. Governing Equations

The acoustic fields generated by an ultrasonic excitation in a moving fluid medium can be calculated from the Mass, Momentum, and Energy Conservation Equations and the State Equation. A piezoelectric actuator that is generally used to excite the acoustic fields in the fluid medium can generate heat. The resulting temperature distribution can

change acoustic resonance frequencies, which requires retuning of the resonant excitation frequency. Here, the effects of the heat generated by the actuator on the acoustophoretic motion are investigated by considering the Energy Conservation Equation along with temperature boundary conditions at the excitation areas.

The four governing equations in a compressible, viscous Newtonian fluid medium can be represented as[27]

$$\frac{\partial \rho}{\partial t} = -\nabla \cdot (\rho \mathbf{v}), \tag{2.1a}$$

$$\rho\left[\frac{\partial \mathbf{v}}{\partial t} + (\mathbf{v} \cdot \nabla \mathbf{v})\right] = -\nabla p + \eta \nabla^2 \mathbf{v} + \beta \eta \nabla (\nabla \cdot \mathbf{v}), \tag{2.1b}$$

$$\rho T\left[\frac{\partial s}{\partial t} + (\mathbf{v} \cdot \nabla s)\right] = \kappa \nabla^2 T + \Psi, \tag{2.1c}$$

$$p = p(s, \rho), \tag{2.1d}$$

where ρ is the fluid density, $\mathbf{v}$ is the fluid velocity vector ($\mathbf{v} = [v_x\ v_y\ v_z]^T$), p is the pressure, s is the entropy, T is the temperature, κ is the thermal conductivity, η is the dynamic viscosity, β is the dimensionless viscosity ratio defined as $\beta = \eta_b/\eta + 1/3$, η_b is the bulk viscosity, and Ψ is the viscous dissipation function.[27] In general, the parameters of the fluid medium (e.g., ρ, κ, η, and β) are the functions of temperature T. When the temperature variation is insignificant, which is true for all the cases in this thesis, these parameters can be considered as constants. For example, when the temperature of a water medium increases from 20°C to 22°C (5% change), the thermal conductivity is changed from κ = 0.599 W/(m·K) to 0.6025 W/(m·K) (0.58% change) and the dynamic viscosity is varied from η = 0.001 Pa·s to 0.00096 Pa·s (4%

change).[27,77]

2.2. Perturbation Method

When carrying out a perturbation expansion in the problem of interest in this thesis, the acoustic Mach number ε is usually used as a perturbation coefficient, which is defined as the ratio of the peak acoustic particle velocity at a representative location to the speed of sound c_0.[28] Based on the assumption of a small acoustic Mach number, each variable y in Eq. (2.1) ($y = p$, ρ, s, T or $\mathbf{v}$) can be expanded to be a summation of a series of acoustic terms $y = y_0 + \varepsilon y_1' + \varepsilon^2 y_2' + \cdots$ where y_n' is the expansion coefficient, $n = 0, 1, 2, \cdots$. Further, the perturbation coefficient ε is expressed implicitly, and then, $y = y_0 + y_1 + y_2 + \cdots$ where $y_n = \varepsilon^n y_n'$. Finally, the acoustic variables are expressed as

$$p = p_0 + p_1 + p_2 + \cdots, \tag{2.2a}$$

$$\mathbf{v} = \mathbf{v}_0 + \mathbf{v}_1 + \mathbf{v}_2 + \cdots, \tag{2.2b}$$

$$\rho = \rho_0 + \rho_1 + \rho_2 + \cdots, \tag{2.2c}$$

$$T = T_0 + T_1 + T_2 + \cdots, \tag{2.2d}$$

$$s = s_0 + s_1 + s_2 + \cdots, \tag{2.2e}$$

The subscript "0", "1" and "2" means the zeroth-, first-, and second-order variables, respectively.[27,28] Here, the subscript "0" represents the variables of the static fluid flow. The subscripts "1" and "2" represent the first- and second-order dynamic variables, respectively and the nth-order ($n > 1$) terms are an order of magnitude smaller than the terms of order n-1 due to the small magnitude of the perturbation coefficient ε.

Since the contribution of the third- and higher-order acoustic components to the

acoustophoretic motion of microparticles is much smaller than that of the zeroth-, first-, and second-order variables, the third- and higher-order acoustic variables are ignored in the proposed numerical procedure. Then, Eq. (2.1) can be decomposed into the zeroth-, first- and second-order equations, by using this perturbation method, which are presented in the sections below.

By using Taylor series expansion, Eq. (2.1d) can be represented as

$$p = p_0 + (\rho - \rho_0)\left.\frac{\partial p}{\partial \rho}\right|_s + (s - s_0)\left.\frac{\partial p}{\partial s}\right|_\rho + \frac{1}{2}(\rho - \rho_0)^2 \left.\frac{\partial^2 p}{\partial \rho^2}\right|_s + \frac{1}{2}(s - s_0)^2 \left.\frac{\partial^2 p}{\partial s^2}\right|_\rho, \quad (2.3a)$$

By plugging the expansions of ρ and s, and keeping up to the second-order terms in Eq. (2.3a), Eq. (2.3a) can rewritten as

$$p = p_0 + \rho_1 c_0^2 + \rho_2 c_0^2 + \frac{1}{2}\frac{B}{A}\frac{c_0^2}{\rho_0}\rho_1^2 + (s_1 + s_2)\left.\frac{\partial p}{\partial s}\right|_\rho + \frac{1}{2}s_1^2 \left.\frac{\partial^2 p}{\partial s^2}\right|_\rho, \quad (2.3b)$$

where c_0 is the sound speed in fluid medium , $c_0 = (\partial p/\partial \rho)^{1/2}|_s$, and B/A is the nonlinear parameter $B/A = (\rho_0/c_0^2 \cdot \partial^2 p/\partial \rho^2)|_s$, e.g., B/A = 5 for distilled water at 20 °C.[28] Here, both c_0 and B/A are based on the isentropic condition. In particular, the fourth term in Eq. (2.3a) can be derived to the fourth term in Eq. (2.3b) up to the second-order small term by using

$$\frac{1}{2}(\rho - \rho_0)^2 \left.\frac{\partial^2 p}{\partial \rho^2}\right|_s = \frac{1}{2}(\rho_1 + \rho_2)^2 \frac{c_0^2}{\rho_0}\left(\frac{\rho_0}{c_0^2}\left.\frac{\partial^2 p}{\partial \rho^2}\right|_s\right) = \frac{1}{2}\frac{c_0^2}{\rho_0}\frac{B}{A}\rho_1^2. \quad (2.3c)$$

2.2.1. Zeroth-Order Governing Equations

In order to investigate the relation between the pressure, density, temperature, and

entropy, the thermodynamic relations between these four variables can be expressed as[39]

$$d\rho = \gamma\beta_0\rho dp - \alpha_v\rho dT\,, \tag{2.4a}$$

$$ds = \frac{C_p}{T}dT - \frac{\alpha_v}{\rho}dp\,, \tag{2.4b}$$

where γ is the specific heat capacity ratio, β_0 is the compressibility, α_v is the thermal expansion coefficient, and C_p is the specific heat capacity at constant pressure. For water at 20 °C, the specific heat capacity ratio is γ = 1.014, the compressibility is β_0 = 4.55×10^{-10} Pa^{-1}, the ambient density is ρ_0 = 998 kg/m^3, the specific heat capacity is C_p = 4183 J/(kg·K), and the thermal expansion coefficient is $\alpha_v = 2.067\times10^{-4}$ K^{-1}.[77] Then, the zeroth-order terms of Eq. (2.4) at 20 °C can be rewritten as $d\rho_0 = 4.60\times10^{-6}dp_0 - 0.206dT_0$ and $ds_0 = 14.27dT_0 - 2.071\times10^{-7}dp_0$. It can be thus concluded that the variation of ρ_0 and s_0 are mainly dependent on the variation of T_0 since the coefficients of dp_0 is so small to be ignored. In other words, the fluid media of interest in this thesis are mainly water or other fluids of which properties are similar to water. Then, the media can be assumed to be incompressible, in which the static (or zeroth-order) pressure variation cannot change the static density or entropy. Then, the zeroth-order equations can be obtained as

$$\nabla\cdot\mathbf{v}_0 - \alpha_v\mathbf{v}_0\cdot\nabla T_0 = 0\,, \tag{2.5a}$$

$$-\nabla p_0 + \eta\nabla^2\mathbf{v}_0 + \beta\eta\nabla\left(\nabla\cdot\mathbf{v}_0\right) = \rho_0\left(\mathbf{v}_0\cdot\nabla\right)\mathbf{v}_0\,, \tag{2.5b}$$

$$\mathbf{v}_0 \cdot \nabla T_0 = \frac{\kappa}{\rho_0 C_p} \nabla^2 T_0 . \tag{2.5c}$$

The fluid medium temperature T_0 can be calculated from Eq. (2.5) where the equation parameters associated with the fluid medium are also dependent on the temperature. Note that the perturbed zeroth-order equations in Eq. (2.5) are nonlinear. In Eq. (2.5c), the viscous dissipation term Ψ presented in Eq. (2.1c) is ignored due to its small magnitude. The viscous fluid medium flow and the boundary layers are considered in Eq. (2.5) by including the viscosity coefficient along with appropriate boundary conditions such as the no-slip condition on walls.

2.2.2. First-Order Governing Equations

In the first-order acoustic fields, the acoustic time scale (e.g., $t_a = 1/10^6 = 10^{-6}$ s at a 1 MHz acoustic excitation) is very short when compared with the time scale of heat conduction $t_c = w^2/\alpha = 0.07$s in a microchannel with a channel width of $w = 100$ μm. Here, the thermal diffusivity is approximately $\alpha = \kappa/\rho_0/C_p = 1.434\times10^{-7}$ m^2/s for water at 20 °C and the thermal characteristic length can then be $L = (t_a\alpha)^{1/2} = 0.151$ μm, for the same time scale as the acoustic wave, that is extremely short compared with the dimension of microfluidic devices. Then, the effects of the thermal conduction can be ignored (*i.e.*, $\kappa = 0$) in the first-order acoustic fields. If there is extremely slow or no flow, the time-derivative of the first-order entropy can be assumed to be zero (*i.e.*, $ds_1/dt = 0$) by setting $\kappa = 0$ and ignoring the small viscous dissipation function Ψ in the first-order, perturbed equation of Eq. (2.1c). Since s_1 should be an oscillating term, $ds_1/dt = 0$ leads to the result that the term s_1 is equal to zero. Therefore, it is concluded that the

first-order temperature is mainly dependent on the corresponding first-order acoustic pressure as shown in Eq. (2.4b) and the order-of-magnitude analysis gives

$$T_1 \sim \frac{\alpha_v T_0}{\rho_0 C_p} p_1, \tag{2.6}$$

where $\alpha_v T_0/\rho_0 C_p$ = 1.451×10^{-8} for water at 20°C. The magnitude of the first-order acoustic pressure p_1 is experimentally measured to be in the order of 10^5 Pa and the magnitude of T_1 is then calculated as 10^{-3} °C from Eq. (2.6). Then the first- and second-order temperature is extremely small to be ignored, which can be also shown by solving the first-order equations including the first-order temperature as in Ref. [39]. Therefore, the first- and second-order entropy equation can be ignored, and the last two terms in the right hand side (RHS) of Eq. (2.3b) can be ignored. Since the temperature variation generated by piezoelectric actuators is usually small, the viscosity of the fluid medium (i.e., η and β) is considered to be constant. However, the zeroth-order temperature still affects the wave propagation speed of the fluid medium that is critical in solving the first- and second-order equations, and thus should be considered in these higher-order equations.

By ignoring the entropy equation as explained above and using the perturbation method, the first-order governing equations are represented as

$$\frac{\partial \rho_1}{\partial t} + \rho_0 \nabla \cdot \mathbf{v}_1 + \rho_1 \nabla \cdot \mathbf{v}_0 + \mathbf{v}_0 \cdot \nabla \rho_1 = 0, \tag{2.7a}$$

$$\begin{aligned} &\rho_0 \frac{\partial \mathbf{v}_1}{\partial t} + \nabla p_1 + \rho_1 (\mathbf{v}_0 \cdot \nabla)\mathbf{v}_0 + \rho_0 (\mathbf{v}_1 \cdot \nabla)\mathbf{v}_0 \\ &+ \rho_0 (\mathbf{v}_0 \cdot \nabla)\mathbf{v}_1 - \eta \nabla^2 \mathbf{v}_1 - \beta\eta \nabla (\nabla \cdot \mathbf{v}_1) = 0 \quad , \end{aligned} \tag{2.7b}$$

$$p_1 - c_0^2 \rho_1 = 0 . \tag{2.7c}$$

Eq. (2.7c) is a well-known linear acoustic equation for the speed of sound. The zeroth-order, fluid medium velocity vector $\mathbf{v}_0$ is input to the first-order, linear equations in Eq. (2.7). Then, the first-order, acoustic solutions are obtained from the first-order equations for a given external acoustic excitation and acoustic boundary conditions (e.g., rigid, non-reflective, or impedance acoustic boundary conditions).

2.2.3. Second-Order Governing Equations

Similarly, the second-order governing equations are written as

$$\frac{\partial \rho_2}{\partial t} + \rho_0 \nabla \cdot \mathbf{v}_2 + \rho_2 \nabla \cdot \mathbf{v}_0 + \mathbf{v}_0 \cdot \nabla \rho_2 = -\nabla \cdot \rho_1 \mathbf{v}_1 , \tag{2.8a}$$

$$\begin{aligned} &\rho_0 \frac{\partial \mathbf{v}_2}{\partial t} + \nabla p_2 + \rho_2 (\mathbf{v}_0 \cdot \nabla)\mathbf{v}_0 + \rho_0 (\mathbf{v}_2 \cdot \nabla)\mathbf{v}_0 \\ &+ \rho_0 (\mathbf{v}_0 \cdot \nabla)\mathbf{v}_2 - \eta \nabla^2 \mathbf{v}_2 - \beta \eta \nabla (\nabla \cdot \mathbf{v}_2) = \\ &-\rho_0 (\mathbf{v}_1 \cdot \nabla)\mathbf{v}_1 - \rho_1 (\mathbf{v}_0 \cdot \nabla)\mathbf{v}_1 - \rho_1 (\mathbf{v}_1 \cdot \nabla)\mathbf{v}_0 - \rho_1 \frac{\partial \mathbf{v}_1}{\partial t}, \end{aligned} \tag{2.8b}$$

$$p_2 - c_0^2 \rho_2 = \frac{1}{2} \frac{B}{A} \frac{c_0^2}{\rho_0} \rho_1^2 . \tag{2.8c}$$

Eq. (2.8c) is a nonlinear acoustic equation. The linear operators in the left hand side (LHS) of Eq. (2.8) are exactly the same as in Eq. (2.7), although the unknown variables are of first- and second-orders in Eqs. (2.7) and (2.8), respectively. The RHS terms in Eq. (2.8) represent the inhomogeneous acoustic source terms that are composed of the first-order variables. Thus, once the first-order solutions are determined from the first-order equations in Eq. (2.7), the second-order equations in Eq. (2.8) become linear as in Eq. (2.7).

For a harmonic excitation of frequency ω, the first-order solution is also oscillating harmonically with the same frequency ω as the excitation source. For the second-order equation, the only excitation source is the nonlinear excitation source shown in the RHS of Eq. (2.8) that is composed of the first-order solution (e.g., $p_1 \cdot p_1$). This nonlinear, harmonic excitation source consists of "time-independent" component (*i.e.*, DC offset) as well as "time-dependent" component with the frequency of 2ω: e.g., $\sin^2\omega t = 1/2 - 1/2\cos(2\omega t)$. Thus, the second-order solution can be written as the summation of both the time-independent and time-dependent components. An acoustic variable is then expressed as $y_2 = y_{20} + y_{22}$ where y represents p, ρ or $\mathbf{v}$, and the subscript "20" and "22" mean the second-order time-independent (*i.e.*, frequency of 0 rad/s) and time-dependent (frequency of 2ω) terms, respectively.

2.3. Acoustic Streaming and Acoustophoretic Force Governing Equations

The second-order, time-independent acoustic particle velocity $\mathbf{v}_{20}$, referred to as acoustic streaming[27,28], can be calculated from the time-averaged, second-order equations. By taking time-averaging of Eq. (2.8),

$$\rho_0 \nabla \cdot \mathbf{v}_{20} + \rho_{20} \nabla \cdot \mathbf{v}_0 + \mathbf{v}_0 \cdot \nabla \rho_{20} = -\left\langle \nabla \cdot \rho_1 \mathbf{v}_1 \right\rangle, \tag{2.9a}$$

$$\begin{aligned} &\nabla p_{20} + \rho_{20}\left(\mathbf{v}_0 \cdot \nabla\right)\mathbf{v}_0 + \rho_0\left(\mathbf{v}_{20} \cdot \nabla\right)\mathbf{v}_0 \\ &+\rho_0\left(\mathbf{v}_0 \cdot \nabla\right)\mathbf{v}_{20} - \eta\nabla^2\mathbf{v}_{20} - \beta\eta\nabla\left(\nabla \cdot \mathbf{v}_{20}\right) = \\ &-\left\langle \rho_0\left(\mathbf{v}_1 \cdot \nabla\right)\mathbf{v}_1 \right\rangle - \left\langle \rho_1\left(\mathbf{v}_0 \cdot \nabla\right)\mathbf{v}_1 \right\rangle - \left\langle \rho_1\left(\mathbf{v}_1 \cdot \nabla\right)\mathbf{v}_0 \right\rangle - \left\langle \rho_1 \frac{\partial \mathbf{v}_1}{\partial t} \right\rangle, \end{aligned} \tag{2.9b}$$

$$p_{20} - c_0^2 \rho_{20} = \left\langle \frac{1}{2}\frac{B}{A}\frac{c_0^2}{\rho_0}\rho_1^2 \right\rangle, \tag{2.9c}$$

where "⟨ ⟩" indicate the time-averaging of the inside equation. By solving the above equations, the acoustic streaming can be obtained. However, the zeroth-order fluid medium flow makes Eq. (2.9) complicated to be solved analytically. As described in Chap. 3, Eq. (2.9) will then be solved by using a numerical method.

An acoustic boundary layer is generated by the interaction between a boundary and a fluid medium. The thickness of this boundary layer is known as the acoustic diffusion length or the viscous penetration depth, defined as $\delta = (2\eta/\rho_0/\omega)^{1/2}$ in Eq. (1.2). Due to this viscous boundary layer, the fluid outside the boundary is divided into the inner boundary layer and the outer boundary layer. Then, the acoustic streaming is spatially divided into inner streaming, known as the "Schlichting streaming", and outer streaming referred to as the "Rayleigh streaming".

Under the condition of no mean flow or slow flow, Eq. (2.9) can be simplified. When the acoustic streaming $\mathbf{v}_{20}$ is of main interest, only Eqs. (2.9a) and (2.9b) are sufficient enough to solve for p_{20} and $\mathbf{v}_{20}$ with Eq. (2.9c) ignored. Therefore, we have

$$\nabla \cdot \mathbf{v}_{20} = -\frac{1}{\rho_0}\left\langle \nabla \cdot \rho_1 \mathbf{v}_1 \right\rangle, \tag{2.10a}$$

$$\nabla p_{20} - \eta \nabla^2 \mathbf{v}_{20} - \beta\eta \nabla\left(\nabla \cdot \mathbf{v}_{20}\right) = -\left\langle \rho_0 \left(\mathbf{v}_1 \cdot \nabla\right)\mathbf{v}_1 \right\rangle - \left\langle \rho_1 \frac{\partial \mathbf{v}_1}{\partial t} \right\rangle . \tag{2.10b}$$

As shown in Eq. (2.10a), the acoustic streaming is highly correlated with the time-averaged mass flux $\langle \rho_1 \mathbf{v}_1 \rangle$, which can be used to analyze the order of magnitude of the acoustic streaming velocity. Furthermore, by using vector identities, Eq. (2.10) can be manipulated as (See Appendix A)

$$\vec{\nabla}\cdot\mathbf{v}_{20} = -\frac{1}{\rho_0}\vec{\nabla}\cdot\left\langle\rho_1\mathbf{v}_1\right\rangle, \tag{2.11a}$$

$$\nabla^2\left(\vec{\nabla}\times\mathbf{v}_{20}\right) = \frac{\rho_0}{\eta}\vec{\nabla}\times\left\langle\left(\mathbf{v}_1\cdot\vec{\nabla}\right)\mathbf{v}_1\right\rangle + \left\langle\mathbf{v}_1\left(\vec{\nabla}\cdot\mathbf{v}_1\right)\right\rangle. \tag{2.11b}$$

Eq. (2.11) is commonly used for the calculation of the acoustic streaming for isentropic, viscous, and homogeneous fluid media with an excitation frequency ω. It is noted that Eqs. (2.11a) and (2.11b) are the time-averaged Mass and Momentum Conservation Equation under a single-frequency excitation. The right-hand-side (RHS) results from the time-averaged mass and momentum transports induced by the first-order acoustic variables, which can be considered as excitation sources for the acoustic streaming. The acoustophoretic force applied on a compressible microparticle is obtained by considering the rate of change in momentum flowing into and out of the volume occupied by the microparticle, represented as

$$f_k = \int_{s_0}\left\langle -p\delta_{ij} - \rho_0 v_i v_j + \eta\left(\partial_j v_i + \partial_i v_j\right) + \left(\beta - 1\right)\eta\left(\partial_k v_k\right)\delta_{ij} + \right\rangle ds, \tag{2.12a}$$

where s_0 represents the microparticle's surface. The first and second terms of the integrand are the rate of change in momentum due to pressure forces and convection of momentum. The third and fourth terms are the rate of change in momentum due to viscous forces. Here, the acoustic terms are considered up to the second order, and thus Eq. (2.12a) can be expressed in the vector form as

$$\mathbf{F} = \int_{s_0}\left\langle\begin{matrix} -\rho_0\mathbf{v}_1\left(\mathbf{v}_1\cdot\mathbf{n}\right) - \mathbf{n}p_{20} + 2\eta\left(\mathbf{n}\cdot\vec{\nabla}\right)\mathbf{v}_{20} \\ +\eta\mathbf{n}\times\left(\vec{\nabla}\times\mathbf{v}_{20}\right) + \left(\beta - 1\right)\eta\mathbf{n}\cdot\left(\vec{\nabla}\cdot\mathbf{v}_{20}\right)\end{matrix}\right\rangle ds. \tag{2.12b}$$

where **n** is the normal vector on the microparticle surface. Under the condition of $\delta_v << a << \lambda$, Eq. (1.1) is derived which is used widely. If the particle radius a is comparable to the viscous boundary layer thickness δ_v and smaller than the wavelength λ, the viscosity of the fluid medium has to be considered. Settnes and Bruus [25] did research on this problem and derived an analytical expression for the acoustophoretic force

$$\mathbf{F} = -V_p \left[\frac{\beta_p}{2} \mathrm{Re}\left(f_1 p_{in}^* \nabla p_{in} \right) - \frac{3\rho_0}{4} \mathrm{Re}\left(f_2^* \mathbf{v}_{in}^* \cdot \vec{\nabla} \mathbf{v}_{in} \right) \right], \tag{2.13a}$$

where

$$f_1 = 1 - \frac{\beta_p}{\beta_0}, \tag{2.13b}$$

$$f_2 = \frac{2\left[1 - \gamma\left(\tilde{\delta}\right)\right]\left(\tilde{\rho} - 1\right)}{2\tilde{\rho} + 1 - 3\gamma\left(\tilde{\delta}\right)}, \tag{2.13c}$$

$$\gamma\left(\tilde{\delta}\right) = -\frac{3}{2}\left[1 + i\left(1 + \tilde{\delta}\right)\right]\tilde{\delta}, \tag{2.13d}$$

$$\tilde{\delta} = \frac{\delta_v}{a}, \tag{2.13e}$$

$$\tilde{\rho} = \frac{\rho_p}{\rho_0}. \tag{2.13f}$$

Eqs. (1.1) and (1.3) are special cases of Eq. (2.13). In most cases, they are able to generate accurate results using less computational time. Otherwise, Eq. (2.13) has to be used.

3. NUMERICAL MODELING OF ACOUSTOPHORESIS IN MICROFLUIDIC CHANNELS*

In this chapter, a numerical method is proposed to analyse the motion of microparticles/cells under the acoustophoretic forces in microfluidic channels. The effects of fluid medium flow and the temperature elevated by piezoelectric actuators on the acoustic streaming and the acoustophoretic forces are also studied by using the proposed numerical modeling approach.

Here, the decomposed equations in the previous chapter are solved by using quadratic mapping functions and a second-order finite difference method (FDM)[38] along with appropriate boundary and acoustic excitation conditions. In this chapter, the fluid medium flow and temperature distributions in a microfluidic device are proposed to be analyzed from the zeroth-order governing equations. The zeroth-order fluid medium flow and temperature solutions are then substituted into the first- and second-order governing equations. Thus, the effects of the zeroth-order variables can be considered in the higher-order equations. The acoustophoretic force applied to the microparticle is calculated by substituting the first-order solutions obtained from the previous step into the Gorkov's Equation. The Newton's Equation of Motion is then solved by applying the fourth-order Runge-Kutta method[38] to obtain the position and velocity of the cell/microparticle numerically when the acoustophoretic force, viscous drag force, and

* Portions of this chapter have been reprinted with the permission of the Acoustical Society of America from Z. Liu, H. Wang, A. Han and Y.-J. Kim, "Effects of fluid medium flow and spatial temperature variation on acoustophoretic motion of microparticles in microfluidic channels," *J. Acoust. Soc. Am.*, 2016, **139**, 332-349.[101] Copyright 2016 Acoustical Society of America.

buoyancy and gravitational forces are applied to the cell/microparticle. In this calculation step, the fluid medium and acoustic streaming velocities are also taken into account in the viscous drag force term.

3.1. Overall Procedure of Numerical Modeling

The proposed numerical modeling method for analyzing the motion of compressible microparticles suspended in microfluidic devices with moving viscous fluid media under resonant acoustic excitations is overviewed in Fig. 3.1. In the following sections, each step in this overview is described in detail.

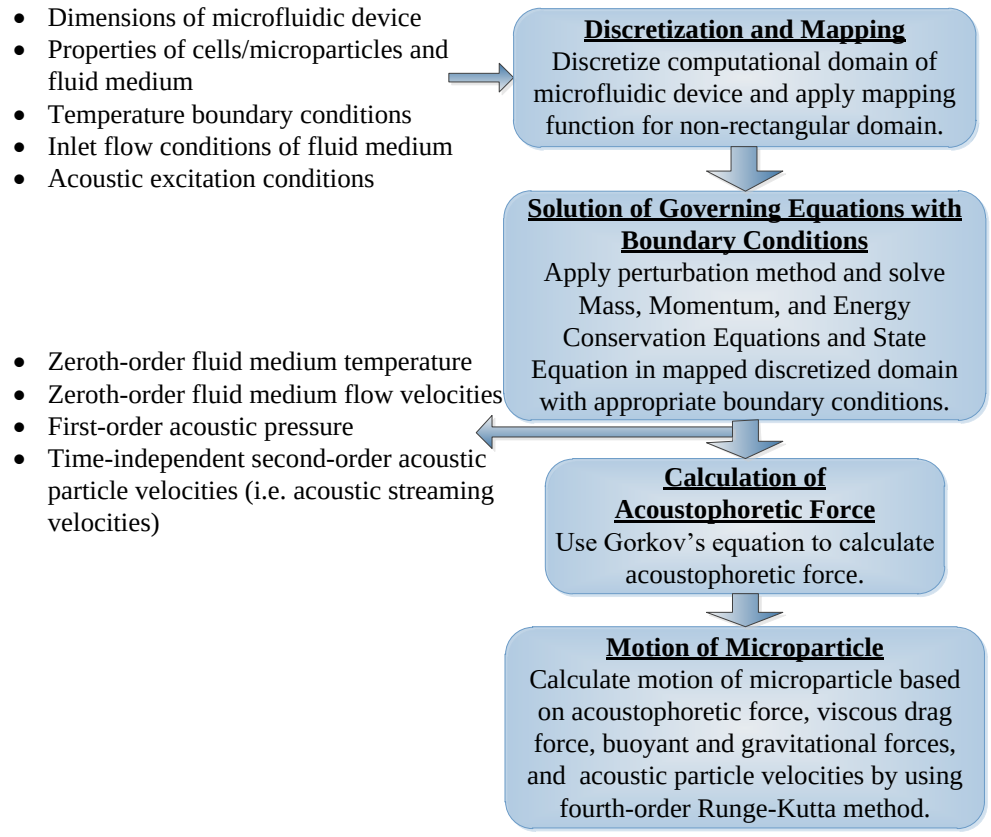

Fig. 3.1: Overview of proposed modeling procedure for numerically analyzing acoustophoretic motion of microparticles in microfluidic devices.[101]

3.1.1. Discretization and Mapping

When a microfluidic device is thin in the thickness direction (i.e., *z*-direction) relative to the minimum wavelength, the acoustic variation in this thickness direction can be ignored and the acoustic pressure and particle velocities in the length and width directions (i.e., *x*- and *y*-directions) are then only of interest. In this case, this microfluidic device can be considered to be 2-D.

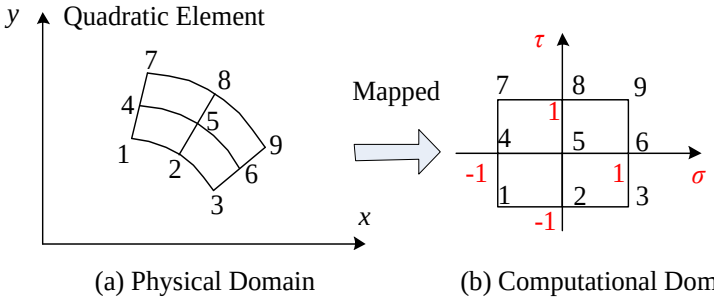

Fig. 3.2: Mapping of single quadratic element with nine nodes from physical to computational domains.[101]

In order to calculate the acoustic fields inside the 2-D microfluidic devices, the computational domain is discretized and a second-order FDM is applied to the perturbed governing equations in Eqs. (2.5), (2.7) and (2.8) in the discretized computational domain. By applying the mapping function, a non-rectangular-shaped physical domain can be mapped into a rectangular computational domain. For example, Fig. 3.2 illustrates a quadratic element with nine nodes mapped from physical domain to computational domain. Therefore, a microfluidic device of any shape can be discretized and mapped into regularly-meshed quadratic elements by using the mapping function.

This mapping function that relates the physical coordinates (x, y) and the computational coordinates (σ, τ) can be expressed as

$$x(\sigma,\tau)=\sum_{i=1}^{i=9}x_i\varepsilon_i, \quad y(\sigma,\tau)=\sum_{i=1}^{i=9}y_i\varepsilon_i\,, \tag{3.1}$$

where ε_i is the quadratic mapping function.[78] The spatial derivatives in both the domains are related by using the chain rule in a matrix form as

$$\begin{bmatrix}\dfrac{\partial}{\partial x}\\ \dfrac{\partial}{\partial y}\end{bmatrix}=[J]^{-1}\begin{bmatrix}\dfrac{\partial}{\partial \sigma}\\ \dfrac{\partial}{\partial \tau}\end{bmatrix} \tag{3.2a}$$

or

$$\begin{aligned}\frac{\partial}{\partial x}&=J_{11}^{-1}\frac{\partial}{\partial \sigma}+J_{12}^{-1}\frac{\partial}{\partial \tau}\\ \frac{\partial}{\partial y}&=J_{21}^{-1}\frac{\partial}{\partial \sigma}+J_{22}^{-1}\frac{\partial}{\partial \tau}\,,\end{aligned} \tag{3.2b}$$

where $[J]$ is the Jacobian matrix and J_{ij}^{-1} is the (i, j) element of the inverse Jacobian matrix $[J]^{-1}$, see Appendix B.

3.1.2. Quadratic Finite Difference Method

At a nodal point (x_m, y_m) in a single quadratic element where m is the node number, for example, m = 1, 2, …, or 9 as shown in Fig. 3.2, an acoustic solution is assumed to be represented as ζ_m ($\zeta = v_x$, v_y, ρ or p). An acoustic solution vector is then defined as $\boldsymbol{\zeta}$ = $[\zeta_1\ \zeta_2\ \ldots\ \zeta_9]^{\mathrm{T}}$. For the square element in the computational domain in Fig. 3.2(b), the finite difference operators that approximate the first spatial derivatives in the perturbed governing equations are defined as $\mathbf{D}_{1\sigma}$ and $\mathbf{D}_{1\tau}$ by using the Kronecker Product "⊗"[38]

as

$$\frac{d\zeta}{d\sigma} \rightarrow \mathbf{D}_{1\sigma}\zeta = (\mathbf{I}_3 \otimes \mathbf{D}_1)\zeta, \tag{3.3a}$$

$$\frac{d\zeta}{d\tau} \rightarrow \mathbf{D}_{1\tau}\zeta = (\mathbf{D}_1 \otimes \mathbf{I}_3)\zeta, \tag{3.3b}$$

where $\mathbf{I}_3$ is the 3 by 3 identity matrix, and $\mathbf{D}_1$ is the first-order finite difference operator in a 1-D space defined as

$$D_1 = \begin{bmatrix} -1.5 & 2 & -0.5 \\ -0.5 & 0 & 0.5 \\ 0.5 & -2 & 1.5 \end{bmatrix}. \tag{3.3c}$$

For the quadratic element, the finite difference operators for the first and second derivatives in the physical coordinate system can be then expressed as

$$\frac{\partial\zeta}{\partial x} \rightarrow \mathbf{D}_{1x}\zeta = \left(\left[J_{11}^{-1}\right]\mathbf{D}_{1\sigma} + \left[J_{12}^{-1}\right]\mathbf{D}_{1\tau}\right)\zeta, \tag{3.4a}$$

$$\frac{\partial\zeta}{\partial y} \rightarrow \mathbf{D}_{1y}\zeta = \left(\left[J_{21}^{-1}\right]\mathbf{D}_{1\sigma} + \left[J_{22}^{-1}\right]\mathbf{D}_{1\tau}\right)\zeta, \tag{3.4b}$$

$$\frac{\partial^2\zeta}{\partial x^2} \rightarrow \mathbf{D}_{2x}\zeta = (\mathbf{D}_{1x}\mathbf{D}_{1x})\zeta, \tag{3.4c}$$

$$\frac{\partial^2\zeta}{\partial y^2} \rightarrow \mathbf{D}_{2y}\zeta = \left(\mathbf{D}_{1y}\mathbf{D}_{1y}\right)\zeta, \tag{3.4d}$$

$$\frac{\partial^2\zeta}{\partial x\partial y} \rightarrow \mathbf{D}_{1xy}\zeta = \left(\mathbf{D}_{1x}\mathbf{D}_{1y}\right)\zeta, \tag{3.4e}$$

where $[J_{ij}^{-1}]$ is the matrix composed of the inverse Jacobian element J_{ij}^{-1} corresponding to each node shown in Fig. 3.2. By applying Eq. (3.4) to Eqs. (2.5), (2.7) and (2.8), the discretized governing equations for a single element are obtained in a matrix form. Then,

the individual matrices are assembled to form a global matrix.[78,79] Based on this global assembly procedure, the zeroth-order governing equations in Eq. (2.5) are then represented as

$$\mathbf{Q}_0\mathbf{U}_0 = \mathbf{F}_0\left(\mathbf{U}_0\right), \tag{3.5}$$

where $\mathbf{U}_0$ is the discretized solution vector defined as $\mathbf{U}_0 = [\mathbf{v}_{0x}{}^{\mathrm{T}}\ \mathbf{v}_{0y}{}^{\mathrm{T}}\ \mathbf{p}_0{}^{\mathrm{T}}\ \mathbf{T}_0{}^{\mathrm{T}}]^{\mathrm{T}}$, $\mathbf{Q}_0$ is the discretized matrix form of the LHS operators in Eq. (2.5), and $\mathbf{F}_0$ is the discretized "nonlinear" excitation vector of the RHS functions in Eq. (2.5). Boundary conditions such as no slip condition (i.e., zero velocities at the walls), inlet fluid medium velocity condition, and temperature distribution on the surfaces of piezoelectric actuators are applied to Eq. (3.5) (Fig. 3.3(a)). : i.e.,

$$v_{0x} = \begin{cases} \dfrac{6v_{0\_avg}\,y\left(w-y\right)}{w^2} \text{ at the inlet of } x = 0 \\ 0 \text{ at the side walls of } y = 0 \text{ and } y = w \end{cases}, \tag{3.6a}$$

$$v_{0y} = 0 \text{ at the inlet of } x = 0 \text{ and at the side walls of } y = 0 \text{ and } y = w, \tag{3.6b}$$

$$p_0 = 0 \text{ at the outlet of } x = L, \tag{3.6c}$$

$$T_0 = \begin{cases} \text{Specified value at the piezoelectric} \\ \text{actuator surface of } x = x_0 \text{ to } x_1 \text{ and } y = 0 \\ 20\ ^{o}C \text{ at all the boundary except the} \\ \text{piezoelectric acuator surface} \end{cases}, \tag{3.6d}$$

where v_{0_avg} is the mean flow speed of the fluid medium. The boundary conditions presented in this chapter can be changed depending on the conditions of a specific microfluidic channel. When the outlets of a microfluidic channel are connected to sample collectors where the gauge pressure can be assumed as $p_0 = 0$, Eq. (3.6c) can be

an appropriate boundary condition. In general, the flow speed at the outlet is not monitored although the inlet flow speed is controlled by a pump.

In order to solve the nonlinear FDM equation in Eq. (3.5), an iteration method[80] is proposed: i.e.,

$$\mathbf{U}_0^{l+1} = \alpha_r \mathbf{Q}_0^{-1} \mathbf{F}_0 \left(\mathbf{U}_0^l \right) + \left(1 - \alpha_r \right) \mathbf{U}_0^l , \tag{3.7}$$

where l is the iteration index (l = 0, 1, 2, ···) and α_r is the relaxation factor ($0 < \alpha_r \leq 1$) that can be used to control the convergence of Eq. (3.7). The equation is repetitively solved until $\mathbf{U}_0$ converges to a solution vector with an assumed initial solution vector $\mathbf{U}_0^0$ at l = 0 that satisfies the boundary conditions. Here, a convergence error is defined as $e = |\mathbf{U}_0^{l+1} - \mathbf{U}_0^l| / |\mathbf{U}_0^l|$. When the error e becomes smaller than a given small convergence constant, the iteration stops and the final $\mathbf{U}_0$ is considered as the solution of Eq. (3.5).

Similar to Eq. (3.5), the first- and second-order governing equations in Eqs. (2.7) and (2.8) can be discretized as

$$\frac{\partial \mathbf{U}_1}{\partial t} - \mathbf{Q}\mathbf{U}_1 = \mathbf{0} , \tag{3.8a}$$

$$\frac{\partial \mathbf{U}_2}{\partial t} - \mathbf{Q}\mathbf{U}_2 = \mathbf{F}_2 , \tag{3.8b}$$

where the first- and second-order solution vectors are $\mathbf{U}_1 = [\mathbf{v}_{1x}{}^{\mathrm{T}}\ \mathbf{v}_{1y}{}^{\mathrm{T}}\ \mathbf{p}_1{}^{\mathrm{T}}]^{\mathrm{T}}$ and $\mathbf{U}_2 = [\mathbf{v}_{2x}{}^{\mathrm{T}}\ \mathbf{v}_{2y}{}^{\mathrm{T}}\ \mathbf{p}_2{}^{\mathrm{T}}]^{\mathrm{T}}$, respectively, and $\mathbf{Q}$ is the discretized version of the linear operators in the LHS of Eqs. (2.7) and (2.8) including the zeroth-order fluid medium velocity vectors, $\mathbf{v}_{0x}$ and $\mathbf{v}_{0y}$ with the coefficients dependent on the zeroth-order fluid medium temperature vector $\mathbf{T}_0$. When an excitation to the system is harmonic (e.g., sinusoidal excitation with

an excitation frequency of ω), the transient response of the system, induced by its initial conditions, exponentially decays out due to the fluid medium damping. Then, the system reaches to a steady state. Since the transient response is generally short and not of importance for analyzing the acoustophoretic motion, it is of interest to find only steady-state solutions in this thesis. For Eq. (3.8a), the first-order acoustic boundary conditions are expressed as

$$v_{1x} = \begin{cases} 0 \text{ at the side walls of } y = 0 \text{ and } y = w \\ \dfrac{p_1}{\rho_1 c_0} \text{ at the inlet and outlet of the channel of } x = 0 \text{ and } x = L \end{cases}, \tag{3.9a}$$

$$v_{1y} = \begin{cases} 0 \text{ at the side walls of } y = 0 \text{ and } y = w \\ \text{Excitation velocity at the piezoelectric} \\ \text{actuator surface of } x = x_0 \text{ to } x_1 \text{ and } y = 0 \end{cases}. \tag{3.9b}$$

The first-order, linear acoustic solution is obtained from the first-order equation in Eq. (3.8a) for a given external acoustic excitation, acoustic boundary conditions (e.g., see Fig. 3.3(b)), and both the zeroth-order, fluid medium velocity and temperature solution vectors. The solution for this linear equation includes the same frequency component as the excitation.

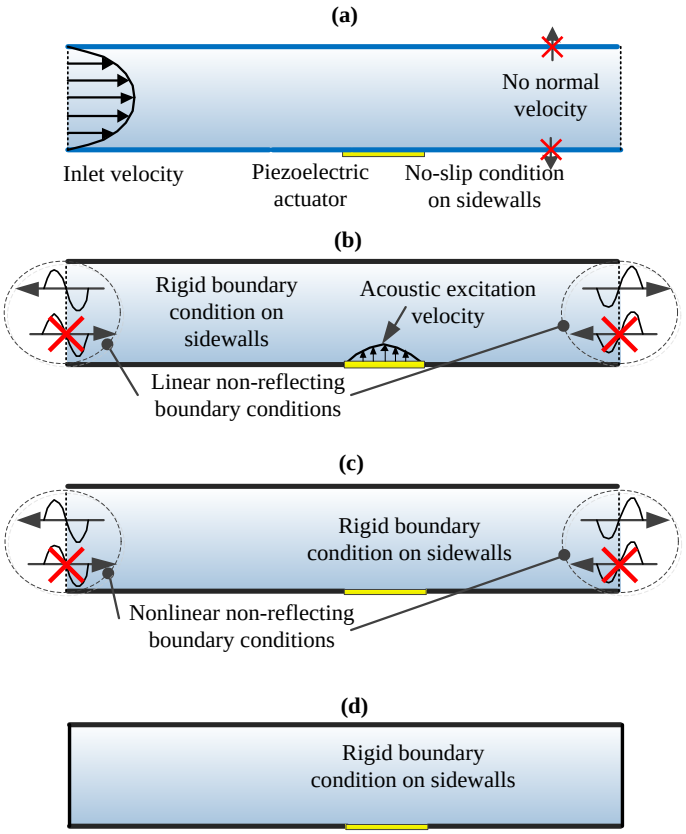

Fig. 3.3: Example of boundary conditions in microchannel with piezoelectric actuator. (a) Boundary conditions for zeroth-order equations. (b) Boundary conditions for first-order equations. (c) Boundary for second-order, time-dependent equations. (d) Boundary conditions for second-order, time-independent equations.[101]

By substituting the first-order linear solution to $\mathbf{F}_2$ in the second-order matrix equation of Eq. (3.8b), the second-order acoustic solution is obtained. Thus, the second-order solution vector can be written as the summation of both the time-independent and time-dependent components. Then, Eq. (3.8b) can be further decomposed into two equations (see Eqs. (2.8) and (2.9)) as

$$-\mathbf{Q}\mathbf{U}_{20} = \mathbf{F}_{20}\,, \tag{3.10a}$$

$$\frac{\partial \mathbf{U}_{22}}{\partial t} - \mathbf{Q}\mathbf{U}_{22} = \mathbf{F}_{22}, \tag{3.10b}$$

where $\mathbf{U}_{20}$ and $\mathbf{U}_{22}$ are the second-order, time-independent and time-dependent solution vectors, respectively (i.e., $\mathbf{U}_2 = \mathbf{U}_{20} + \mathbf{U}_{22}$) and $\mathbf{F}_{20}$ and $\mathbf{F}_{22}$ are the time-independent and time-dependent components of the nonlinear excitation function, respectively (i.e., $\mathbf{F}_2 = \mathbf{F}_{20} + \mathbf{F}_{22}$). By applying the acoustic boundary conditions, e.g., shown in Figs. 3.3(c) and 3.3(d), Eqs. (3.10a) and (3.10b) can be solved for the second-order, time-independent and time-dependent acoustic fields excited by the first-order acoustic variables. The mathematical expressions of the corresponding boundary conditions are represented as

$$v_{22x} = \begin{cases} 0 \text{ at the side walls of } y = 0 \text{ and } y = w \\ \dfrac{p_{22}}{\rho_{22} c_0} \text{ at the inlet and outlet of } x = 0 \text{ and } x = L \end{cases}, \tag{3.11a}$$

$$v_{22y} = 0 \text{ at all the boundary}, \tag{3.11b}$$

$$v_{20x} = v_{20y} = 0 \text{ at all the boundary}. \tag{3.11c}$$

The boundary conditions of $v_{1x} = p_1/(\rho_1 c_0)$ in Eq. (3.9a) and $v_{22x} = p_{22}/(\rho_{22} c_0)$ in Eq. (3.11a) are the non-reflective boundary conditions for the first- and second-order governing equations, Eqs. (3.8) and (3.10), respectively. These non-reflective boundary conditions are useful when a small x-direction length of the microfluidic channel is selected for computationally-efficient numerical analyses as in Fig. 3.4(a). Then, the non-reflective conditions result in acoustic solutions that include the effects of a larger channel than the selected length. In case that there are rigid walls at $x = 0$ and $x = L$ and the fluid medium is pumped through small tubes connected to the bottom or top of the

channel, the zero velocity conditions of $v_{1x} = v_{22}x = 0$ at $x = 0$ and $x = L$ may be more appropriate than the non-reflective boundary conditions. The second-order, time-independent acoustic particle velocities obtained from Eq. (3.10a) is referred to as the acoustic streaming velocities.

3.1.3. Motion of Microparticle

For a single microparticle suspended in a moving fluid medium excited by a resonant acoustic wave, there are mainly four forces exerted on the microparticle: i.e., acoustophoretic force, viscous drag force, gravity force, and buoyancy force.[15,16] For 2-D microfluidic devices, the gravity and buoyancy forces in the vertical direction (i.e., the thickness direction) are assumed not to affect the microparticle's motion in the 2-D horizontal plane. When the motion of microparticles occur in the cross-section of a microfluidic device including the vertical direction, both the constant gravity and buoyancy forces can be considered in the procedure presented below.

Here, the acoustophoretic force is obtained by applying the first-order acoustic pressure and particle velocities to the Gorkov's equation. Since the acoustic pressure or particle velocity is a function of microparticle's position and time, the acoustophoretic force is also the function of the microparticle's position and time: i.e.,

$$\mathbf{F}_a = \mathbf{F}_a\left(\mathbf{r}_p, t\right), \tag{3.12}$$

where the acoustophoretic force has two directional components in a 2-D microchannel, i.e., $\mathbf{F}_a = [F_{ax}\ F_{ay}]^{\mathrm{T}}$ and $\mathbf{r}_p$ is the location vector of the microparticle defined as $\mathbf{r}_p = [r_{px}\ r_{py}]^{\mathrm{T}}$.

For a low Reynolds Number flow (e.g., Re < 1), the viscous drag force is proportional to the velocity difference (or the relative velocity) between the microparticle and the fluid medium:[27] i.e.,

$$\mathbf{F}_v = -6\pi\eta a\left(\mathbf{v}_p - \mathbf{v}_m\right) = -6\pi\eta a\mathbf{v}_p + 6\pi\eta a\mathbf{v}_m, \tag{3.13}$$

where $\mathbf{F}_v = [F_{vx}\ F_{vy}]^{\mathrm{T}}$, a is the microparticle's radius at the static equilibrium state (i.e., undeformed radius), $\mathbf{v}_m$ is the medium velocity vector, $\mathbf{v}_m = [v_{mx}\ v_{my}]^{\mathrm{T}}$ including the zeroth-order medium velocities ($\mathbf{v}_{0x}$ and $\mathbf{v}_{0y}$) and the acoustic streaming velocities ($\mathbf{v}_{20x}$ and $\mathbf{v}_{20y}$), and $\mathbf{v}_p$ is the velocity vector of the microparticle, $\mathbf{v}_p = [v_{px}\ v_{py}]^{\mathrm{T}}$. In the medium velocity vector, the first-order particle velocities and the second-order, time-dependent velocities are not considered since their time-averaged velocities are zero.

The acoustophoretic force in Eq. (1.1), the viscous drag force in Eq. (3.13), and the buoyancy and gravity forces are used to calculate the microparticle's motion from the Newton's Equation of Motion: i.e.,

$$\frac{\partial \mathbf{U}_p}{\partial t} = \mathbf{Q}_p\mathbf{U}_p + \mathbf{F}_p\left(\mathbf{U}_p, t\right), \tag{3.14}$$

where m_p is the mass of the microparticle included in $\mathbf{Q}_p$ and $\mathbf{F}_p$, $\mathbf{U}_p$ is the vector of the microparticle's position and velocity defined as $\mathbf{U}_p = [v_{px}\ v_{py}\ r_{px}\ r_{py}]^{\mathrm{T}}$, and the matrices, $\mathbf{Q}_p$ and $\mathbf{F}_p$ are represented as

$$\mathbf{Q}_p = \begin{bmatrix} -\dfrac{6\pi\eta a}{m_p} & 0 & 0 & 0 \\ 0 & -\dfrac{6\pi\eta a}{m_p} & 0 & 0 \\ 1 & 0 & 0 & 0 \\ 0 & 1 & 0 & 0 \end{bmatrix} \tag{3.15a}$$

and

$$\mathbf{F}_p = \begin{bmatrix} \dfrac{F_x}{m_p} + \dfrac{6\pi\eta a v_{mx}}{m_p} & \dfrac{F_y}{m_p} + \dfrac{6\pi\eta a v_{my}}{m_p} & 0 & 0 \end{bmatrix}^{\mathrm{T}}. \tag{3.15b}$$

The resultant force components are $F_x = F_{ax} + F_{bx} + F_{gx}$ and $F_y = F_{ay} + F_{by} + F_{gy}$ where the subscripts of *a*, *b*, and *g* represent the acoustophoretic, buoyant, and gravitational forces, respectively. Here, the subscript "*x*" and "*y*" can be changed to "*y*" and "*z*" depending on the plane where the microparticle moves. It is proposed that Eq. (3.14) is solved for the microparticle's position and velocity vectors by using the fourth-order Runge-Kutta method.

3.1.4. Modified, One-Dimensional Analytical Model

In this thesis, the proposed modeling procedure is compared with the commonly used 1-D analytical model in Eq. (1.3). For this comparison, the 1-D analytical model in a static fluid medium is modified to include the effects of the fluid medium flow. The 1-D analytical acoustophoretic force F_{ay_1D} in the *y*-direction for a compressible microparticle in a static fluid medium is given in Eq. (1.3). In this 1-D analytical model, the *x*-direction acoustophoretic force, F_{ax_1D} is equal to zero. Then, the second term in the RHS of Eq. (3.14), F_p can be modified as

$$\mathbf{F}_p = \left[\frac{F_{x\_1D}}{m_p} + \frac{6\pi\eta a v_{mx}}{m_p} \quad \frac{F_{y\_1D}}{m_p} + \frac{6\pi\eta a v_{my}}{m_p} \quad 0 \quad 0 \right]^{\mathrm{T}}, \tag{3.16}$$

where the resultant force components are $F_{x\_1D} = F_{bx} + F_{gx}$ and $F_{y\_1D} = F_{ay\_1D} + F_{by} + F_{gy}$, and the fluid medium flow is considered in the velocity terms of the first two non-zero elements. The other terms except the force term in Eq. (3.14) remain unchanged in the modified 1-D analytical model.

3.2. Simulation Results and Discussion

By using the proposed modeling method, microparticle trajectories in three representative microfluidic device configurations were simulated and compared to those obtained from the modified 1-D analytical model, a model developed by using COMSOL Multiphysics, and an experiment. The three microfluidic device configurations are (1) a 2-D, shallow, rectangular microchannel, (2) a circular microfluidic chamber, and (3) a 2-D rectangular cross-sectional model of a microchannel.

For the cases of the circular chamber and rectangular cross-section models, the sidewall boundaries for the first-order acoustic fields are set to be rigid except the excitation areas. For analyzing acoustophoretic microparticle motion in the shallow rectangular microchannel, acoustic variations in the thickness direction (i.e., the *z*-direction) were ignored as discussed in Section 3.1.1 and thus it is considered as a 2-D microchannel. The specific boundary conditions for the zeroth-, first-, and second-order governing equations are shown in Fig. 3.3.

In order to understand the effects of both the fluid medium velocity and the heat

generated by the piezoelectric actuator on the acoustophoretic forces and the acoustic streaming, various fluid medium velocity and temperature boundary conditions were considered separately in the shallow, rectangular microchannel.

As the baseline unless specified otherwise, the diameter and density of the microparticles were set to 10 μm and 1050 kg/m^3, respectively. The compressibility of the microparticle and fluid medium were set to 2.25×10^{-10} Pa^{-1} and 4.55×10^{-10} Pa^{-1}, respectively.

In both the 2-D, shallow microchannel model and the rectangular cross-section model, the acoustic diffusion length is δ_{rect} = 0.39 μm and the microparticles are larger than 2.5 μm in radius. In the circular chamber model, the acoustic diffusion length is δ_{circle} = 0.52 μm and the oil droplet is 7 μm in radius. Therefore, these simulation conditions satisfy the assumption of the small particles compared to the acoustic diffusion length to apply the Gorkov's acoustophoretic force equation in Eq. (1.1) to these simulations.

3.2.1. Simulated Acoustic Fields for 2-D, Shallow, Rectangular Microchannel with Uniform Temperature Distribution

Figure 3.4 shows the baseline simulation configuration of the shallow, rectangular microchannel with the uniform temperature distribution, the predicted acoustophoretic forces for the baseline microparticle, and the acoustic streaming. The temperature was set to 20°C uniformly in the entire physical domain and thus the first half-wavelength resonance excitation frequency in the y-direction was $f = c_0/2/L_y$ = 2.117 MHz for the microchannel with the width of L_y = 0.35 mm. The inlet fluid velocity profile is set to be

a parabolic shape with the spatially-averaged speed of 14 mm/s at the upstream boundary (see Fig. 3.4(a)). As shown in Fig. 3.4(a), the acoustic excitation weighted with a Hanning-windowed velocity profile was applied at the excitation area on the sidewall where the piezoelectric actuator was placed. The maximum amplitude ratio of the second-order time-dependent and first-order acoustic pressure are 0.07 that satisfies the requirement of the perturbation method in Section 2.2.

Although a localized acoustic excitation over a small range (i.e., only 2 mm in length as indicated in Fig. 3.4(a)) was applied, a significant length of the microchannel was affected by this excitation as in the acoustophoretic forces in the *x*- and *y*-directions and the acoustic streaming (Figs. 3.4(b) – 3.4(d)). However, the effects of the excitation diminished quickly as the distance from the excitation center increased. Thus, the force and acoustic fields in Fig. 3.4 show "2-D" distributions that cannot be predicted accurately by using the 1-D analytical model. Since the microparticles have positive contrast factors, they are forced to y = 0.175 mm in the *y*-direction while in the *x*-direction they are pushed away from x = 20 mm as shown in Fig. 3.4(b) and (c). The acoustophoretic force in the *y*-direction F_{ay} is about 23 times stronger than that in the *x*-direction F_{ax} in magnitude.

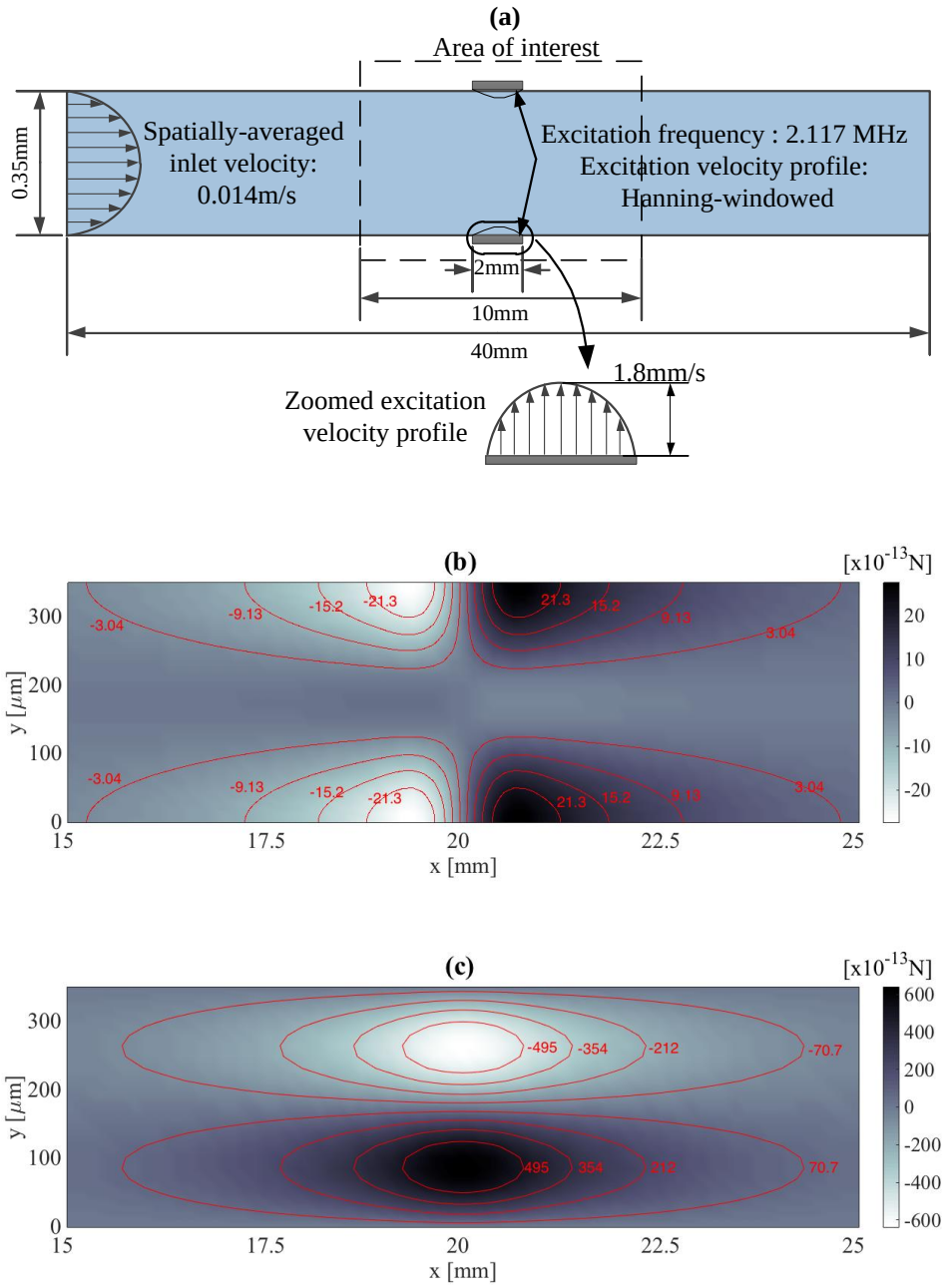

Fig. 3.4: Numerically predicted acoustic fields with uniform temperature distribution for baseline simulation setup case. (a) Baseline simulation setup. (b) Time independent acoustophoretic force in *x*-direction. (c) Time independent acoustophoretic force in *y*-direction. (d) Second-order, time-independent acoustic velocity (the background gray map plot represents the magnitude of the acoustic streaming velocity).[101]

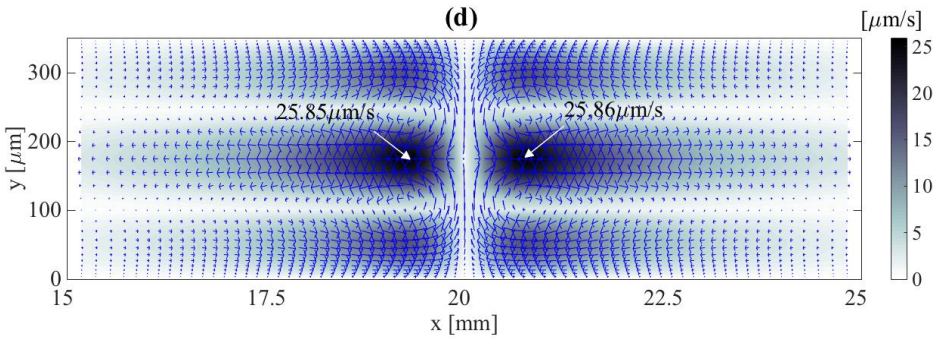

Fig. 3.4: Continued

In Fig. 3.4(d), the four vortexes can be observed in the microchannel, where the *x*-direction acoustic streaming velocity components v_{20x} are larger than the *y* components v_{20y}. The acoustic streaming seems to be symmetric with respect to the x = 20 mm location. In Fig. 3.4(d), the maximum positive and negative acoustic streaming velocities are almost the same and thus the small fluid mean flow speed 0.014 m/s does not affect the acoustic streaming significantly. In the *x*-direction, both the acoustophoretic force and the acoustic streaming push microparticles away from center location (x, y) = (20mm, 0.175mm). Therefore, microparticles suspended in a static fluid medium can gradually aggregate away from the location (20 mm, 0.175 mm).

3.2.2. Comparison Between 2-D Numerical Model and 1-D Analytical Model

In order to conduct a numerical simulation that resembles the 1-D analytical model case, a simulation setup was generated as in Fig. 3.5(a). Here, a numerical model with 1-D plane-wave-like acoustic fields in the *y*-direction was developed by using a large excitation area (i.e., 100 mm in length). The amplitude of the first-order acoustic pressure calculated by using the proposed numerical model was used as the pressure input P_1 in Eq. (1.3) for calculating the particle trajectory based on the modified 1-D

analytical model in Section 3.1.4. In both the models, the same parabolic velocity profile in the *x*-direction are assumed as the zeroth-order, inlet fluid medium velocity condition and the same viscous drag force model are considered as described in Section 3.1.3. Figure 3.5(b) shows that the simulated particle trajectories obtained from both the proposed numerical model and the modified 1-D analytical model are almost identical to each other, with a maximum position difference of 7 μm. This difference comes from the 2-D effects that always exist although the excitation boundary is much larger than the areas of interest. The small trajectory difference confirms that the proposed numerical model is valid when compared to the modified 1-D analytical model.

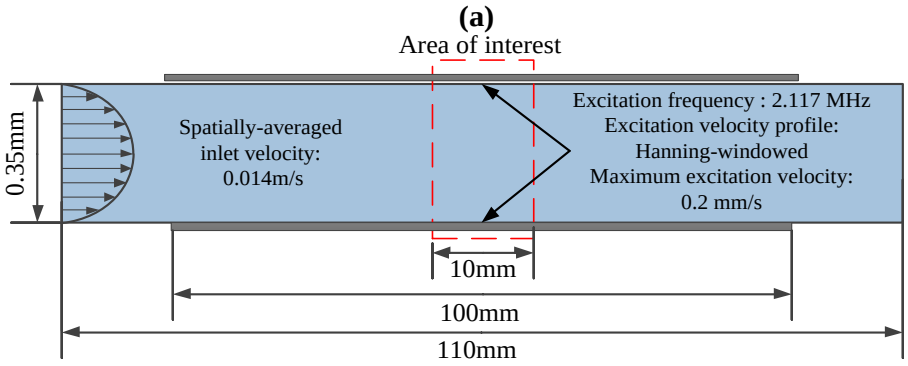

Fig. 3.5: Comparison between proposed 2-D numerical model and modified 1-D analytical model. (a) Simulation setup. (b) Comparison between simulated particle trajectories of 2-D numerical and 1-D analytical models.[101]

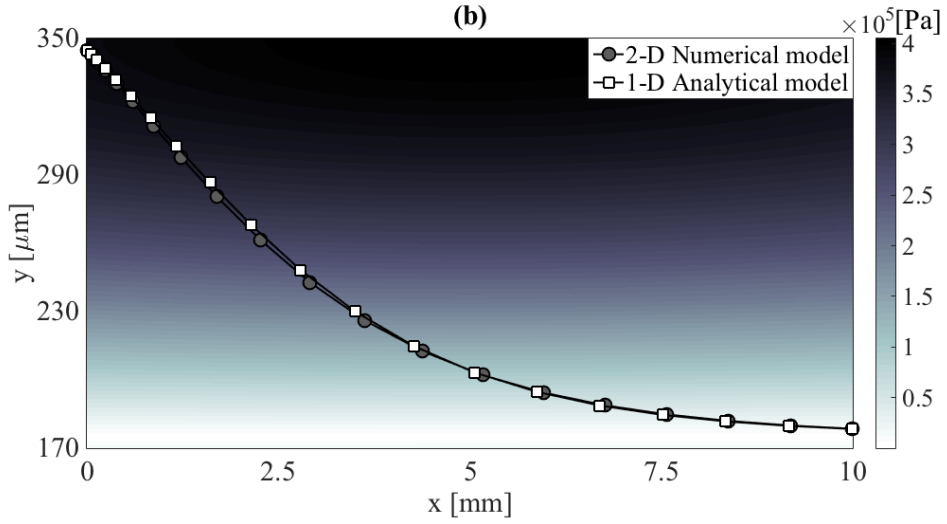

Fig. 3.5: Continued.

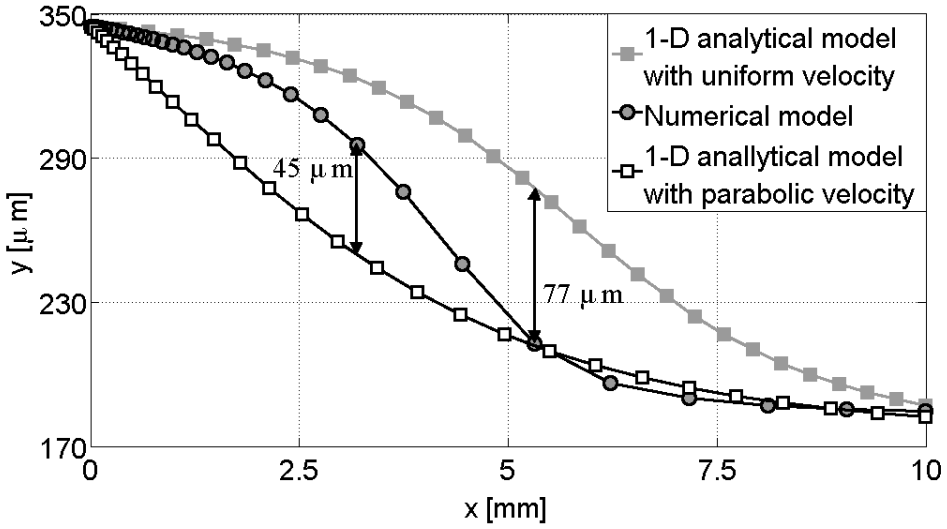

Fig. 3.6: Simulated trajectories of microparticles calculated by using 2-D numerical and 1-D analytical models for baseline simulation configuration in Fig. 3.4(a).[101]

In practice, it is challenging to generate a uniform excitation in a large area that can result in 1-D, plane-wave-like acoustic fields inside a microchannel. In this respect, the localized excitation model that also includes the parabolic flow profile (i.e., the 2-D

numerical model in Fig. 3.4(a)) closely resembles "real" microfluidic systems. Additionally, the 1-D analytical model in Eq. (3.16) can be modified to consider the effects of either uniform or parabolic velocity profile. As can be seen in Fig. 3.6, the particle trajectory including the effects of the 2-D acoustic fields when compared to that of the modified 1-D analytical model with the parabolic velocity profile shows the maximum 45 μm difference in the *y*-direction location. When comparing the simulated trajectory of the 2-D numerical model to that of the modified 1-D analytical model including the uniform velocity profile, this difference is even more significant, showing the maximum 77 μm difference. This difference is significantly pronounced in Fig. 3.6 since the microparticle's initial location is close to the sidewall where the *x*-direction medium velocity is almost zero for the parabolic velocity profile. In general, the parabolic medium velocity is more realistic than the uniform flow due to the viscous boundary layers along the sidewalls. Through the results in Fig. 3.6, it is shown that the proposed 2-D numerical model can be used to more accurately predict the motion of microparticles in the acoustic standing wave than the simple 1-D model.

3.2.3. Simulated Motion of Microparticles in 2-D Rectangular Cross-Section of Microchannel and Comparison with COMSOL Multiphysics Model

In addition to the horizontal motion of microparticles, they can move in the vertical direction due to the acoustophoretic force, gravity, buoyancy, and acoustic streaming in the vertical direction. Figure 3.7(a) shows a 2-D cross-sectional simulation setup where the sidewalls are sinusoidally excited and the water medium is static (i.e., in no motion). The acoustic streaming on the rectangular cross-section is shown in Fig.

3.7(b). In this figure, there are the four acoustic streaming vortices, which is similar to the acoustic streaming in Fig. 3.4(d), although the magnitude and direction are different. The almost identical acoustic streaming pattern is also predicted by using the modeling method, proposed by Muller et al.[39], that implemented in a commercial software package, COSMOL Multiphysics. Regarding the predicted first-order acoustic pressure, the proposed FDM model shows the maximum pressure of 1.033×10^5 Pa, while the COMSOL model shows the maximum pressure of 1.019×10^5 Pa, resulting in approximately 1.4% difference. The maximum magnitudes of the acoustic streaming velocities for both the FDM and COMSOL models are 1.018 μm/s and 1.057 μm/s, respectively, showing approximately 2.2% difference.

The predicted microparticle trajectories are also compared. Figure 3.7(c) shows the trajectories of 10 μm polystyrene (PS) beads from three different initial *z*-locations when they are subject to the acoustophoretic, gravity, buoyancy, and viscous drag forces. In the simulations, the gravitational force was applied in the negative *z*-direction. When there is no acoustic streaming and no acoustic pressure variation in the *z*-direction, these microparticles should be moving at the same speed regardless of the *z*-direction height differences when starting from the same *y*-location. However, as in Fig. 3.7(c), the velocities of these microparticles are dependent on their initial *z*-locations due to the acoustic streaming. The microparticle trajectories of both the models are in line with each other with the maximum trajectory distance of 6 μm. The small differences in the simulated acoustic fields and the microparticle trajectories indicate that the proposed modeling method is valid when compared with the modeling method proposed by

Muller et al.[39]

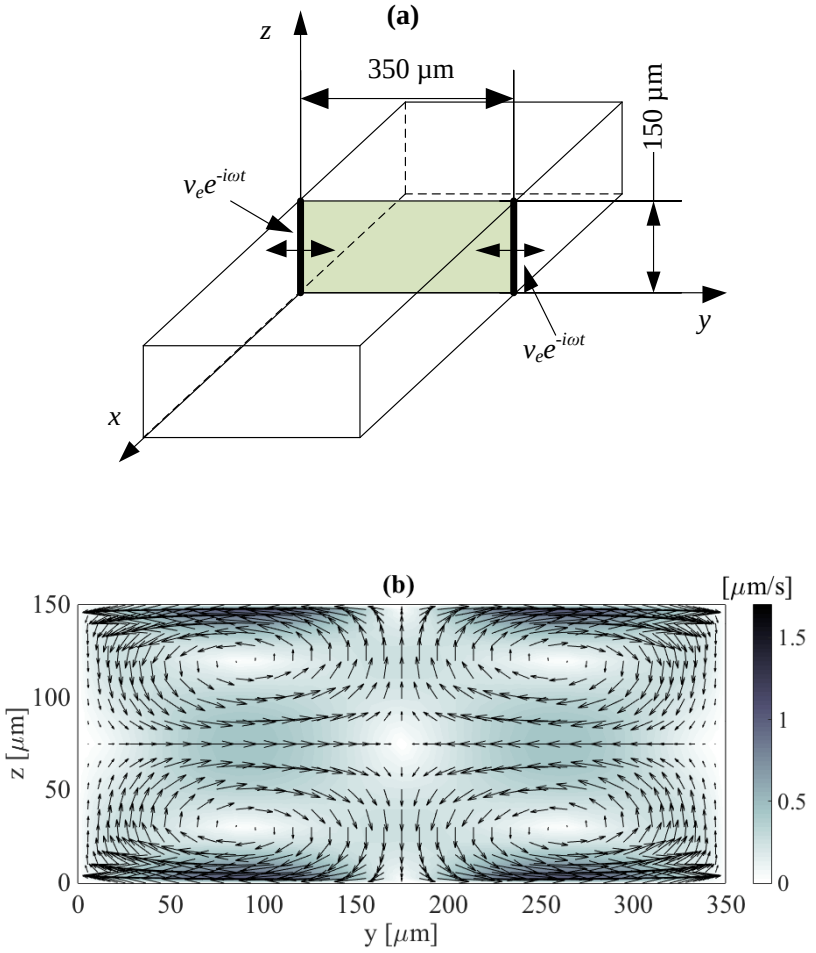

Fig. 3.7: Numerically predicted acoustic streaming and microparticles motion in cross-section of microchannel. (a) Simulation setup (v_e = 0.2 mm/s). (b) Acoustic streaming velocity vectors and amplitudes predicted by using proposed FDM method. (c) Trajectories of microparticles under gravity, buoyancy, viscous drag force, and acoustophoretic force. The white and gray lines represent the microparticle trajectories simulated by using the proposed FDM model and COMSOL model, respectively. The diameter, density and compressibility of the microparticle are 10 µm, 1100 kg/m^3, and 2.25×10^{-10} Pa^{-1}, respectively. The vertical dotted lines in Fig. 3.7(c) indicate the same time step lines, when all of the microparticles start to move at t = 0 and y = 0.01 mm.[101]

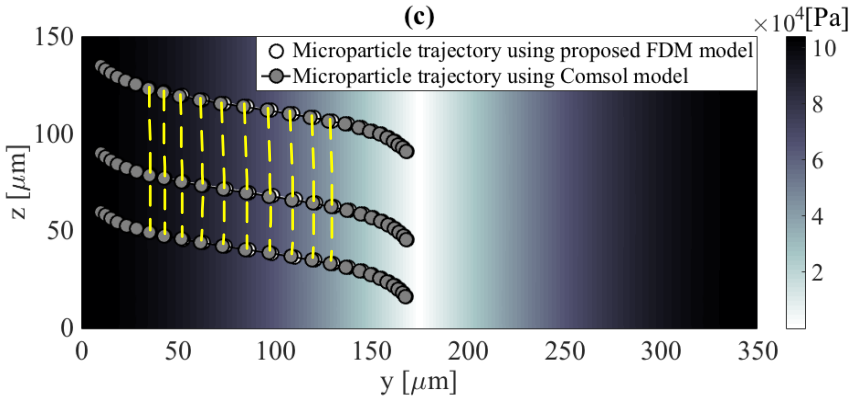

Fig. 3.7: Continued.

3.2.4. Simulated Motion of Oil Droplets in Circular Chamber and Comparison with Experimental Data

By using the mapping functions described in Section 3.1.1, the acoustophoretic motion of microparticles in non-rectangular microfluidic devices can be analyzed. For example, a microchannel with a circular chamber can be designed to trap microparticles in certain areas of the chamber.[81] For a simulation and an experiment, the dimensions of the circular chamber are shown in Fig. 3.8(a). The radius of the circular chamber is r = 0.373 mm and the channel width at the inlet and outlet is 0.125 mm. This radius determines 1.1 MHz as the first resonance frequency to trap crude oil (Midland, Texas) droplets in water inside the circular chamber. Due to the negative acoustic contrast factor of the oil droplets, they move towards the chamber's sidewalls where the acoustic pressure anti-nodes are formed in the resonant standing wave. The microfluidic channel was fabricated in silicon to a depth of 100 µm, and anodically bonded to a borofloat cover glass. A cylindrical piezoelectric transducer with the height and diameter of 15 mm and 25 mm (Model: PZ26, Ferroperm Piezoceramics A/S, Denmark) was attached

to the bottom of the microchip using wax, and actuated with a function generator (DG4102, Rigol Technologies Inc., OH) via a 40 dB power amplifier (406L, Electronic Navigation Industries Inc., NY). The oil droplets of 14 μm in diameter were generated by an off-chip T-junction droplet generator[81], and injected into the microfluidic channel with a syringe pump (Pico Plus, Harvard Instruments). Using a microscope (Eclipse LV100, Nikon Instruments Inc, NY) and camera (DS-2MV, Nikon Instruments Inc, NY), the motion of an oil droplet was recorded and the recorded motion was processed with an in-house Matlab program to automatically extract the trajectory of the oil droplet as a function of time.

Based on the experimental conditions, the simulation setup of the microchannel is shown in Fig. 3.8(a). For simplification, the boundary of the chamber (i.e., the circumferential sidewalls represented in the thick lines in Fig. 3.8(a)) is considered as the sinusoidal excitation boundary. In Fig. 3.8(a), the *y*-direction excitation velocity was optimally identified to v_e = 0.66 mm/s by fitting experimental and predicted trajectories of the oil droplet. The spatially-averaged fluid medium velocity at the inlet was 2.22 mm/s that was measured by timing the flow volume of the water medium and the oil droplets. For the oil droplet, the density and compressibility were measured as 880 kg/m^3 and 6.6×10^{-10} Pa^{-1}, respectively.

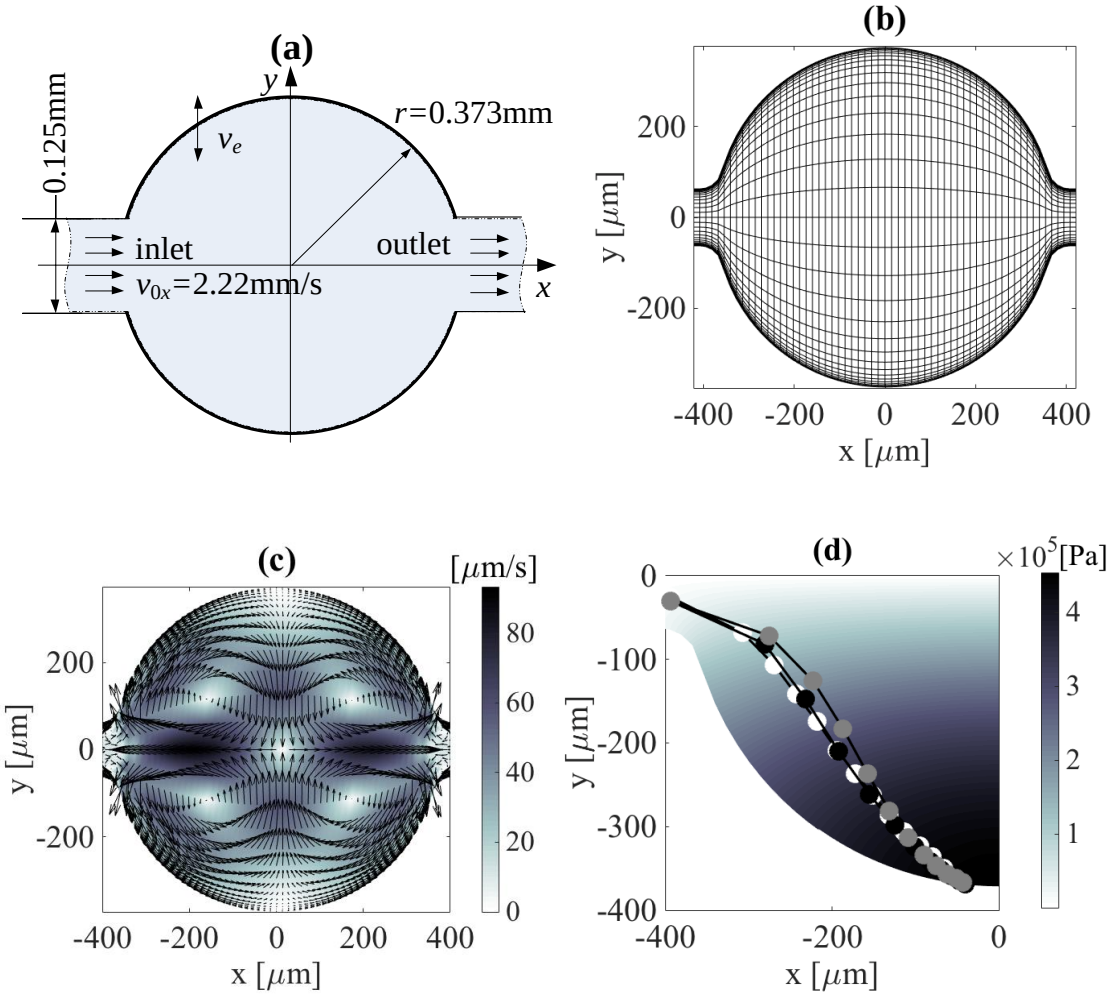

Fig. 3.8: Numerical and experimental analyses of oil droplet trajectories in circular microchannel. (a) Simulation setup. (b) FDM meshes. (c) Acoustic streaming velocity field. (d) Absolute amplitude of first-order, linear acoustic pressure field at first resonance frequency (1.162 MHz) overlaid with experimental and simulated oil droplet trajectories (the black and gray lines represent the simulated oil droplet trajectories with and without the inclusion of the acoustic streaming, respectively and the white one represents the experimental trajectory).[101]

Using the FDM model, the first resonant excitation frequency is identified at $f_1 = c_0/r/3.40 = 1.162$ MHz, agreeing with the experimental resonance frequency of 1.1 MHz.

The predicted acoustic streaming velocity and acoustic pressure fields are shown in Figs. 3.8(c) and 3.8(d), respectively. For this first resonant excitation case, the first-order acoustic pressure field has an acoustic pressure nodal line in the middle and two anti-nodes at the sidewalls. Due to the slow flow velocity close to the sidewalls, the oil droplets stay stationary once they approach close to the sidewall, being trapped at the sidewall. In Fig. 3.8(d), the white line represents the experimental oil droplet trajectory and the black and gray ones do the numerically predicted trajectories with and without the acoustic streaming included, respectively. The simulated oil droplet trajectory is matched well with the experimental one including the acoustic streaming, validating the numerical model of the circular trapping chamber. However, the predicted trajectory without the acoustic streaming included has the short distance difference from the experimental one, indicating that the acoustic streaming cannot be ignored for analyzing the acoustophoretic motion of the oil particle in the circular chamber.

3.2.5. Effects of Fluid Flow Velocity on Acoustophoretic Forces and Acoustic Streaming in 2-D, Shallow, Rectangular Microchannel

In order to investigate the effects of the fluid medium flow on the acoustophoretic forces as well as the acoustic streaming velocities, the mean flow speed of the fluid medium, v_{0_avg} is varied from 0 m/s to 10 m/s. Here, the maximum speed of 10 m/s is selected as a limit case, which may be rarely used in a real microfluidic device. For the microchannel with the width of w = 0.35 mm and the depth of h = 0.15 mm, the hydraulic diameter is $D_{hydr} = 2wh/(w+h)$ = 0.21 mm and the corresponding Reynolds number is $Re = \rho D_{hydr} v_{0\_avg}/\eta$ = (1000 kg/m^3×0.21 mm × 10 m/s) / (0.001 Pa·s) = 2100

at the maximum flow speed of 10 m/s. Thus, in the selected flow speed range, the fluid medium flow can be considered as a laminar flow.

Figures 3.9(a) and 3.9(b) show the acoustophoretic forces at v_{0_avg} = 10 m/s and Fig. 3.9(c) shows the acoustic streaming velocities at v_{0_avg} = 10 m/s. The maximum acoustophoretic forces in the *x*- and *y*-directions are reduced 5.8% and 9.7%, respectively, when compared with the results in Fig. 3.4, and the maximum acoustic streaming velocity is reduced 85.3%. Figs. 3.10(a) and 3.10(b) shows the spatially averaged percentage errors of the acoustophoretic forces and the acoustic streaming velocities as a function of the flow speed. The spatially averaged errors are calculated by using Eq. (3.17) below with reference to the acoustophoretic force and acoustic streaming velocity in the case of no fluid medium flow and no temperature variation (i.e., uniform temperature distribution at 20 °C).

$$\mathrm{E}_r = \frac{\sum_{m=1}^{m=N}\sum_{n=1}^{n=M}\left|\mathbf{q}\left(x_m, y_n\right) - \mathbf{q}_{ref}\left(x_m, y_n\right)\right|}{\sum_{m=1}^{m=N}\sum_{n=1}^{n=M}\left|\mathbf{q}_{ref}\left(x_m, y_n\right)\right|} \times 100, \tag{3.17}$$

where $\mathbf{q}$ is the acoustophoretic force vector or acoustic streaming velocity vector, and $\mathbf{q}_{ref}$ is the reference, (x_m, y_n) is the data location vector, and *N* and *M* are the numbers of the data points in the *x*- and *y*-directions, respectively. For each data point in Fig. 3.10, the domain for the spatial average is from *x* = 15 mm to *x* = 25 mm.

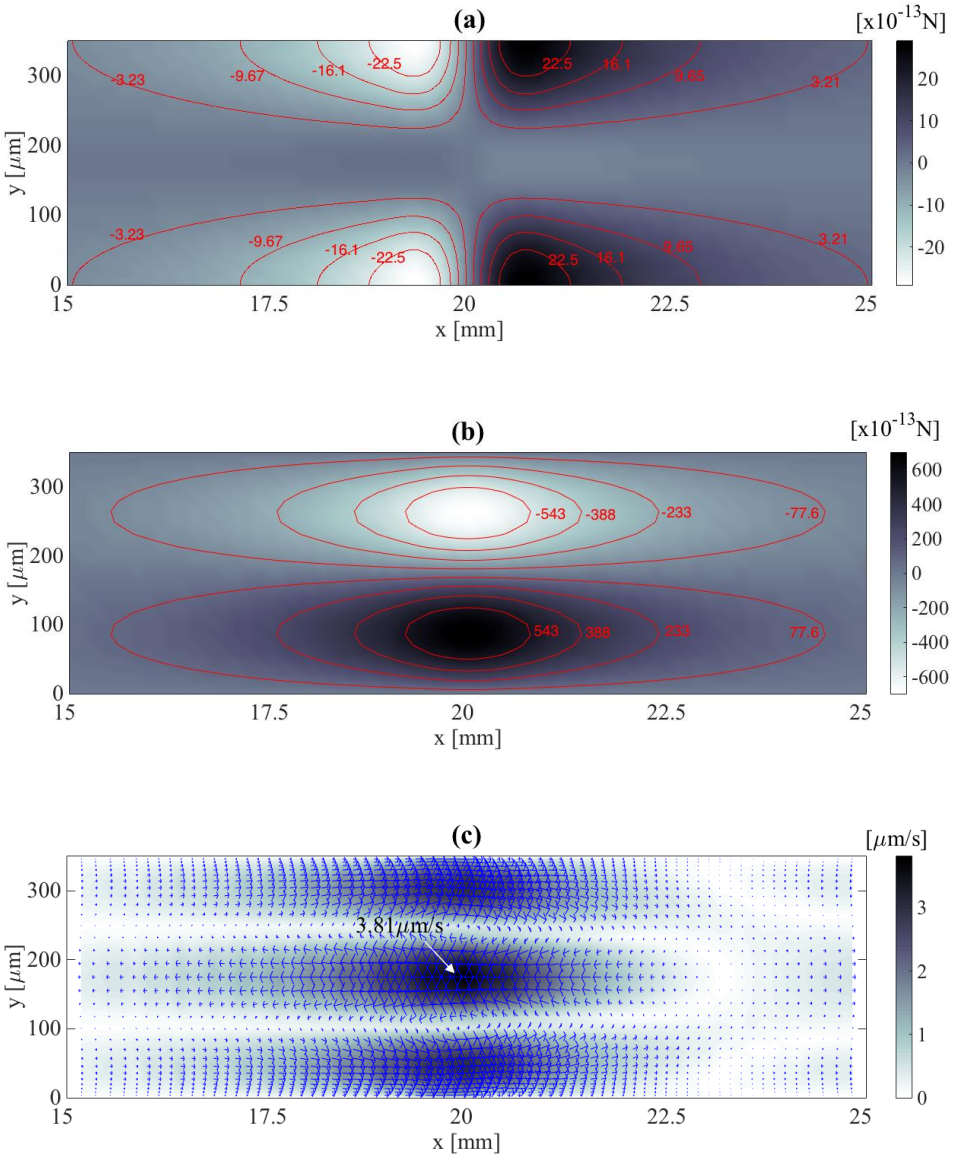

Fig. 3.9: Numerically predicted acoustic fields with mean flow speed of 10 m/s. (a) Time-independent acoustophoretic force in *x*-direction. (b) Time-independent acoustophoretic force in *y*-direction. (c) Second-order, time-independent acoustic velocity (the background gray map plot represents the magnitude of the acoustic streaming velocity).[101]

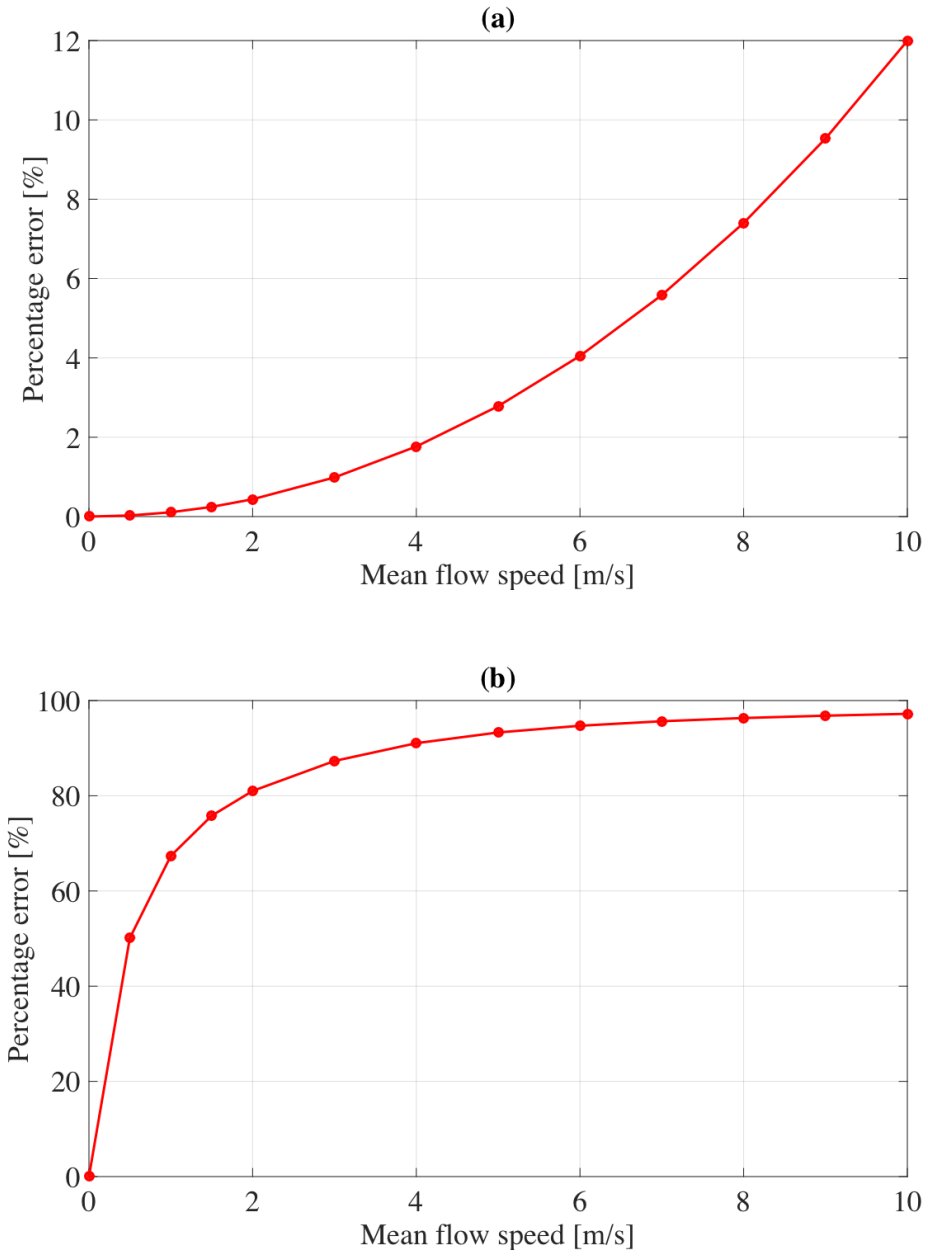

Fig. 3.10: Effects of fluid medium speed on acoustophoretic force and acoustic streaming. (a) Spatially averaged percentage error of acoustophoretic forces as function of fluid medium mean flow speed. (b) Spatially averaged percentage error of acoustic streaming velocities as function of fluid medium mean flow speed. The percentage errors are referenced at the condition of no fluid medium flow and no spatial temperature variation.[101]

As shown in Figs. 3.9(a) and 3.9(b), the spatial pattern of the acoustophoretic force is not significantly affected by the fluid medium flow speed, although the magnitudes of the acoustophoretic force are changed noticeably. The force magnitude increases as the mean flow speed v_{0_avg} increases with the maximum change of approximately 12.0% at v_{0_avg} = 10 m/s as shown in Fig. 3.10(a). For v_{0_avg} = 1 m/s, the maximum percentage change of the acoustophoretic force is merely 0.11%. Therefore, in the microchannel with the low mean flow speed of v_{0_avg} < 1 m/s, the effects of the fluid medium velocity on the acoustophoretic forces can be ignored.

In contrast, as shown in Fig. 3.10(b), the effects of the flow speed on the acoustic streaming velocities are much more significant than those on the acoustophoretic forces, even in the low flow speed. In particular, from 0 m/s to 2 m/s in Fig. 3.10(b), the spatially averaged percentage error increases significantly to 81.0% and then the error slope becomes slow, and then reaches to the maximum percentage error of approximately 97.2% at v_{0_avg} = 10 m/s. The dramatic change of the acoustic streaming velocities at the low fluid medium speed can be caused by the convection of the zeroth-order fluid flow as shown in Fig. 3.9(c) where the acoustic streaming velocities are pushed and stretched along the direction of the flow when compared to Fig. 3.4(d).

3.2.6. Effects of Local Temperature Elevation on Acoustophoretic Forces and Acoustic Streaming in 2-D, Shallow, Rectangular Microchannel

For the case of the elevated temperature boundaries along the excitation areas, the temperature was set from 20 ^{o}C to 25 ^{o}C at the excitation boundaries where the piezoelectric actuators were placed and 20 °C at the other boundaries. This temperature

range is selected based on the temperature changes observed in real microfluidic channels with the dimensions similar to those in Fig. 3.4(a). The fluid medium was static and the excitation frequency was set to be the same as in Fig. 3.4(a) (i.e., 2.117 MHz).

Figure 3.11(a) shows the zeroth-order temperature distribution due to the heat generated from the piezoelectric actuator. Since the spatial temperature distribution affects the thermal and acoustic parameters of the fluid medium, it can be seen that the resulting acoustophoretic forces and acoustic streaming are significantly different (Figs. 3.11(b) – 3.11(d)) from those without considering the elevated temperature in Fig. 3.4. In Figs. 3.11(b) – 3.11(d), the acoustophoretic forces and acoustic streaming are more focused at the excitation areas from x = 19 mm to x = 21 mm where the temperature is higher than the other areas. The magnitudes of the acoustophoretic forces in Figs. 3.11(b) – 3.11(c) were reduced significantly (e.g., 96.2% reduction at x = 20 mm for the acoustophoretic force in the y-direction) under the same excitation condition, although there was only a temperature difference of 5 °C between the heat source (i.e., piezoelectric actuator) and the other boundaries. The amplitude reduction is caused by the half-wavelength resonance frequency shifted by the heat. The heat can increase the wave speed in the fluid medium and then decrease the half-wavelength resonance frequency for the given channel width. As shown in Fig. 3.11(d), the maximum acoustic streaming velocity was also changed (approximately 36.1% reduction) by the heat when compared to the acoustic streaming results without temperature increase in Fig. 3.4(d).

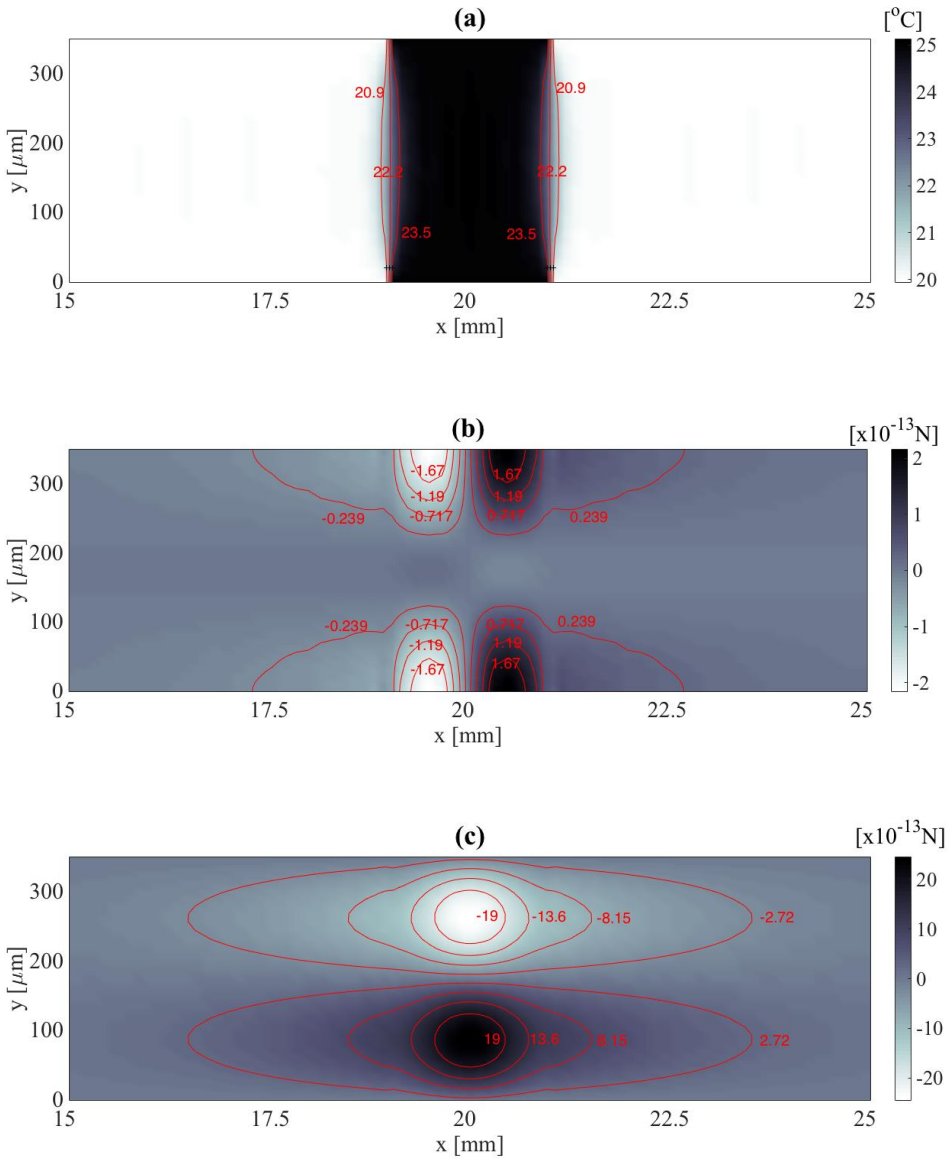

Fig. 3.11: Numerically-predicted acoustic fields with elevated temperature boundary condition of 25 ºC at excitation areas. (a) Amplitude of zeroth-order temperature. (b) Time-independent acoustophoretic force in *x*-direction. (c) Time-independent acoustophoretic force in *y*-direction. (d) Second-order, time-independent acoustic velocity (the background gray map plot represents the magnitude of the acoustic streaming velocity).[101]

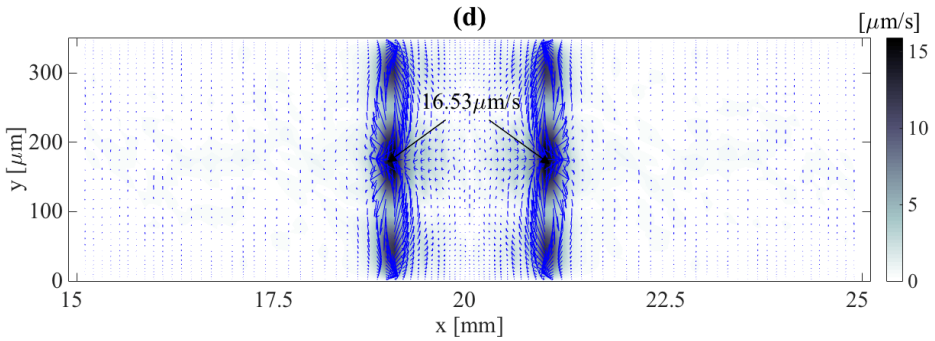

Fig. 3.11: Continued.

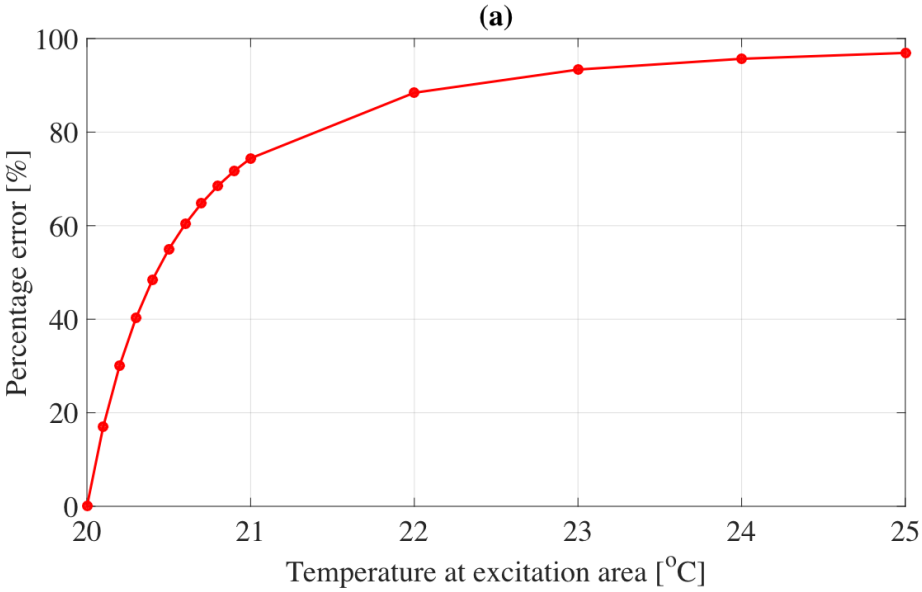

Fig. 3.12: Effects of temperature at excitation areas on acoustophoretic force and acoustic streaming. (a) Spatially averaged percentage error of acoustophoretic forces as function of temperature at excitation areas. (b) Spatially averaged percentage error of acoustic streaming velocities as function of temperature at excitation area. The reference values are those under the conditions of no zeroth-order medium flow and no temperature variation.[101]

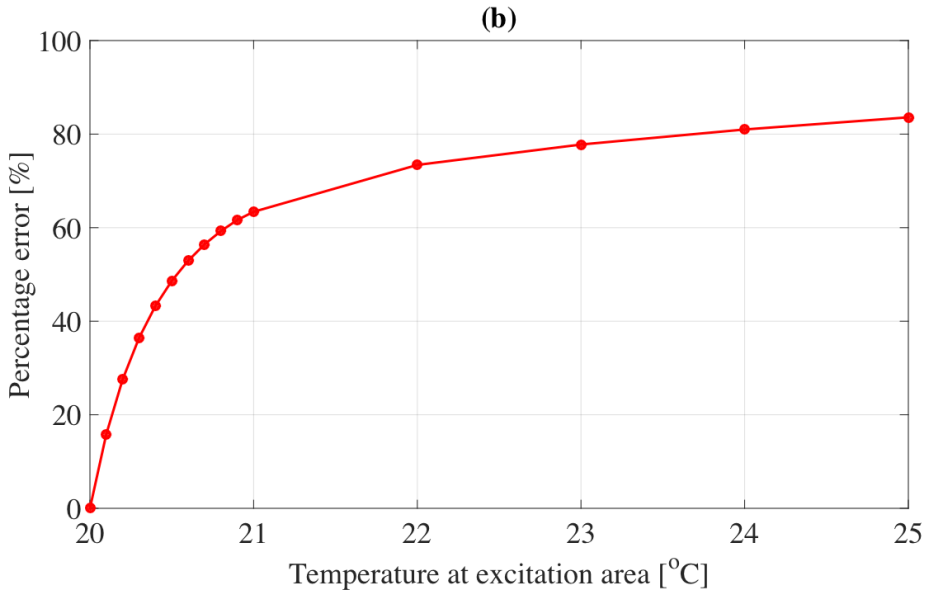

Fig. 3.12: Continued.

Figure 3.12 shows the spatially averaged percentage errors, of the acoustophoretic forces and the acoustic streaming velocities, caused by the local temperature elevation. These errors are defined in Eq. (3.17) and referenced on the baseline case in Fig. 3.4. In Fig. 3.12, the significant changes of the acoustophoretic forces and the acoustic streaming can be observed when the temperature T_e increases from 20 °C with the maximum errors of the acoustophoretic forces and acoustic streaming velocities of 96.9% and 83.6%, respectively. Here, the spatial patterns of the acoustophoretic forces at the different piezoelectric actuator temperatures are similar to Figs. 3.11(b) and 3.11(c) and thus not shown. Even at the temperature elevation by 2 °C from 20 °C (i.e., 10 % change), there are the significant acoustophoretic force and streaming errors of 88.4% and 73.4% induced by the change of the wave propagation speed. From T_e = 20 °C to T_e = 22 °C, both the acoustophoretic forces and the acoustic streaming have large

changes with the corresponding percentage errors of 88.4% and 73.4%, respectively. In the temperature range from T_e = 22 ^{o}C to T_e = 25 ^{o}C, the percentage errors for both are insignificant. Thus, when tuning the resonant excitation frequency, the temperature change, even one or two degrees, will cause significant changes of the acoustophoretic forces and the acoustic streaming and thus it is important to control the temperature elevation induced by the piezoelectric actuator or retune the resonant excitation frequency.

3.3. Conclusion

The numerical modeling procedure was presented that can accurately predict the acoustophoretic motion of compressible microparticles in microfluidic devices. By applying the mapping function, the second-order FDM, and the acoustic boundary conditions to the perturbed equations, the fluid medium flow and temperature and the acoustic pressure and particle velocity fields could be predicted. Based on the acoustophoretic force model proposed by Gorkov, these numerically-calculated flow, temperature, and acoustic fields could then be used to accurately predict the motion of microparticles. This numerical modeling procedure includes the effects of the viscous boundary layers, the fluid medium flow and temperature, and the various microchannel geometries. The proposed numerical modeling procedure was validated by comparing its results to those of the modeling method proposed by Muller et al. as well as by comparing the microparticle trajectories obtained from both the proposed procedure in the 1-D plane-wave-like excitation case and the corresponding 1-D analytical model modified to include the medium flow effects. The modeling procedure was also

validated by comparing the predicted trajectory of oil droplets to the experimentally recorded trajectory in the circular flow-through chamber.

In the 2-D, shallow, rectangular microchannel, it is found that with the increasing fluid medium flow speed, the acoustophoretic forces applied on a microparticle is increased gradually and the spatially-averaged force estimation error was 12% at the mean flow speed of 10 m/s. Due to the convective effects of the fluid medium flow, the pattern of the acoustic streaming was changed significantly as the flow speed was increased. The acoustic streaming vortexes were stretched along the direction of the flow, and their velocity magnitudes were decreased significantly. For the fast moving flow, the effects of the flow cannot be ignored, where the spatially-averaged acoustic streaming velocity estimation error was 97.2% at the mean flow speed of 10 m/s.

Due to the elevated temperature around the piezoelectric actuator, the acoustophoretic force was reduced significantly since this local temperature elevation could shift the resonant frequency. The acoustic streaming was also significantly affected by the spatial gradient of the first-order acoustic pressure and particle velocity affected by the local temperature elevation. Even for a local temperature change of 0.5 ^{o}C, the significant changes in the acoustic streaming with the error of 20.5% could be observed.

The proposed FDM-based numerical modeling procedure can be used both to accurately predict acoustophoretic particle motion in microchannels and to optimally design acoustophoresis-based microfluidic systems in the near future.

The proposed numerical modeling procedure has several advantages over existing

analytical and numerical approaches. First, by using the mapping functions, the acoustic pressure and particle velocity fields in microfluidic devices of any shapes can be numerically predicted. Thus, the effects of 2-D or 3-D geometries including 2-D or 3-D acoustic fields can be easily considered. Second, the effects of the fluid medium flow on the acoustophoretic force and the acoustic streaming are included in the proposed numerical model. The effects of the fluid medium flow on the acoustophoretic motion can then be analyzed, resulting in an accurate prediction of the microparticle motion. Although Muller et al.[39] recently described that the acoustic streaming could be included in their modeling procedure implemented in a commercial software package, COMSOL Multiphysics, they included only a static fluid medium condition. Lastly, the zeroth-order temperature is proposed to be calculated to study the effects of the heat generated by piezoelectric actuators on the first- and second-order acoustic fields.

4. MODELING OF CELLS IN PLANAR ACOUSTIC WAVE

The typical structure of a human cell consists of cell membrane, nucleus, cytoplasm, and cytoskeleton. In this chapter, the cell is assumed to be a sphere in geometry, modelled as a membrane enclosing a compressible fluid medium (i.e., referred to as the fluid model)[49-51] or a simple, uniform, solid elastic sphere (i.e., the solid model)[51,52]. The fluid model can be further classified as a simple fluid model (e.g., no membrane with only fluid such as liquid droplets), or a complex fluid model (i.e., a viscoelastic membrane enclosing a viscous fluid medium). Once the complex fluid model is developed, it can be reduced to the simple fluid model by specifically adjusting some modeling parameters.

To simplify the derivation of these two cell models, the excitation wave incident to the cell is assumed to be planar, and the waves scattered from and transmitted through the cell surface are expressed analytically by using the superposition of the spherical harmonic functions in the spherical coordinate system. Based on the first-order velocity and stress boundary conditions on the cell surface, a characteristic equation for the cell model is constructed and solved for the unknown spherical harmonic coefficients of the scattered and transmitted waves. Then, the dynamic responses of various cells/microparticles with different mechanical properties to the planar, incident acoustic wave are investigated as presented in the following sections.

4.1. Oscillation of Cells/Microparticle's Surface

The planar, incident acoustic wave interacts with the surface of a cell or

microparticle, generating scattered and transmitted waves as shown in Fig. 4.1. This interaction is characterized with the properties of both the cell/microparticle and the fluid medium. Then, it is of great interest to investigate the effects of the cell/microparticle's properties on the scattered and transmitted waves. The overall procedure to calculate the scattered and transmitted waves is shown in Fig. 4.1.

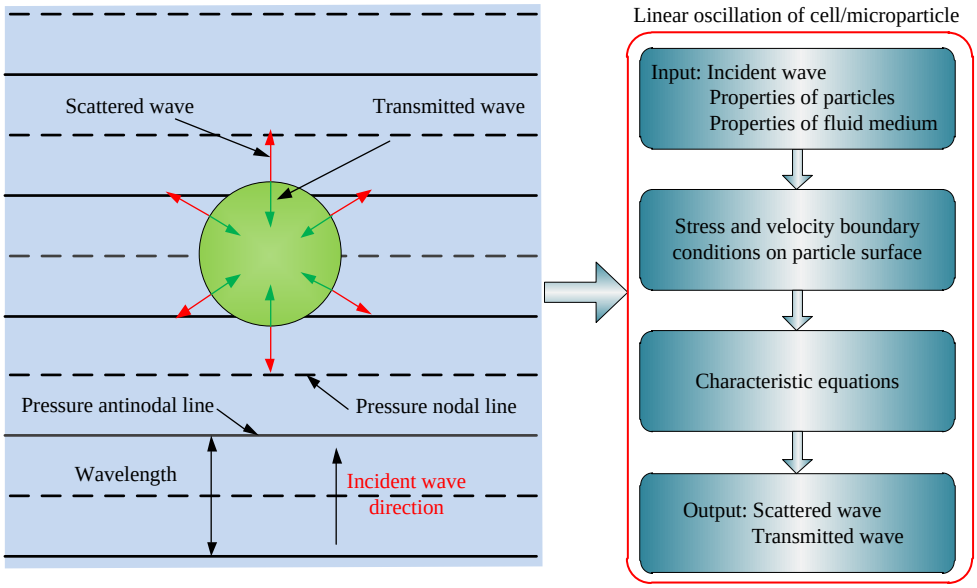

Fig. 4.1: Overall procedure for calculating scattered and transmitted waves generated by interaction between planar incident wave and surface of cell/microparticle.

The spherical coordinates are defined in Fig. 4.2. To simplify the derivation process of the cell model, the planar incident wave at a single frequency of ω is assumed to be incident in the z-direction. Thus, the oscillation of the cell/microparticle is axisymmetric with respect to the z-axis.

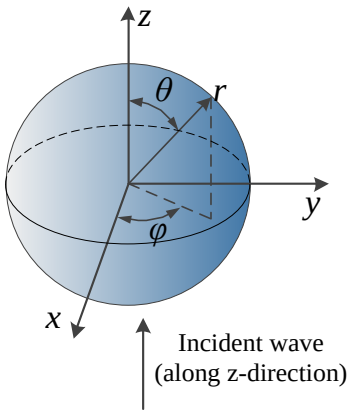

Fig. 4.2: Definition of spherical coordinates. The incident wave is incident in the positive *z*-direction and the cell's oscillation is then axisymmetric about the *z*-axis.

In the Cartesian coordinate system, a planar wave can be expressed in the form of either a standing wave $P_a\cos(kz)e^{-i\omega t}$ or a propagating wave $P_a e^{-i\omega t+ikz}$. In the spherical coordinate system, both the standing and propagating waves are represented by the superposition of the Spherical Bessel Functions as

$$p_1 = \sum_{n=0}^{\infty} C_{pn} j_n\left(kr\right) P_n\left(\cos\theta\right). \tag{4.1a}$$

For the standing wave, the superposition coefficients can be represented as

$$C_{pn} = P_a \,\mathrm{Re}\left(i^n e^{ikz_0}\right)\left(2n+1\right), \tag{4.1b}$$

and for the propagating wave,

$$C_{pn} = P_a \left(i^n e^{ikz_0}\right)\left(2n+1\right), \tag{4.1c}$$

where z_0 is the origin of the spherical coordinate system (i.e., the center of the cell/microparticle). In Eq. (4.1a), the maximum number n is generally limited, e.g., to $n < 15$ and the truncated series gives a good approximation in the near field of the origin.

Thus, this truncated series is sufficient enough for the study of the acoustic fields near the particle surface.

4.2. Cell Model with Membrane Enclosing Viscous Compressible Fluid Medium

Figure 4.3 shows the cell model with the membrane surrounding the viscous fluid medium. Here, the membrane can be considered to be viscoelastic, simply viscous, or purely inviscid depending on the specific cell type of interest, and the characteristics of the membrane are described by surface tension, surface compression modulus, surface shear modulus, surface compression viscosity, and surface shear viscosity[46-50]. The fluid medium enclosed by the membrane is considered to be homogeneous, viscous, and compressible, and the corresponding properties of interest are density, sound speed, and dynamic viscosity. It is also assumed that the fluid medium outside the membrane is compressible and viscous.

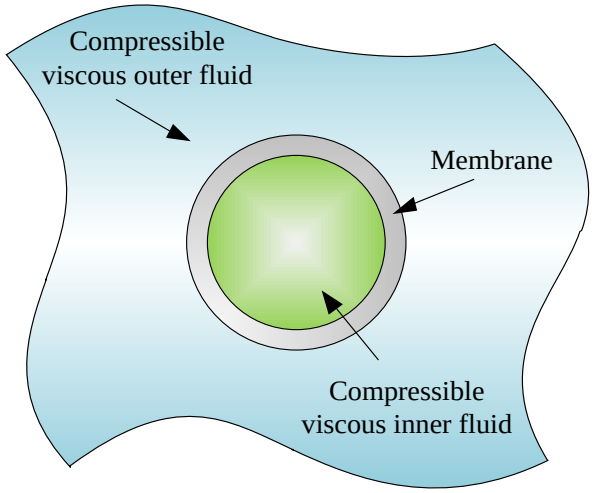

Fig. 4.3: Fluid model of cell with membrane enclosing compressible viscous fluid medium. Outside the membrane, the fluid medium is viscous and compressible.

4.2.1. Expression of Waves in Spherical Coordinate

Inside and outside the cell membrane, the linear, first-order acoustic waves can be decomposed into normal and shear components. These longitudinal and shear components are then expressed by the first-order, scalar velocity potential ϕ_1 and vector velocity potential $\mathbf{\Psi}_1$, respectively. In the axisymmetric case, the vector potential $\mathbf{\Psi}_1$ has only the φ-component. Therefore, the incident velocity potential ϕ_{inc} and the scalar and vector velocity potentials ϕ_1 and $\mathbf{\Psi}_1$ for the scattered wave (with the subscript of "*s*") and the transmitted wave (with the subscript of "*t*") are expressed as

$$\phi_{inc} = \sum_{n=0}^{\infty} A_n j_n\left(k_o r\right) P_n\left(\cos\theta\right) e^{-i\omega t}\,, \tag{4.2a}$$

$$\phi_{1s} = \sum_{n=0}^{\infty} B_n h_n\left(k_o r\right) P_n\left(\cos\theta\right) e^{-i\omega t}\,, \tag{4.2b}$$

$$\mathbf{\Psi}_{1s} = \hat{e}_{\varphi} \sum_{n=0}^{\infty} C_n h_n\left(\chi_o r\right) P_n^1\left(\cos\theta\right) e^{-i\omega t}\,, \tag{4.2c}$$

$$\phi_{1t} = \sum_{n=0}^{\infty} C_n j_n\left(k_i r\right) P_n\left(\cos\theta\right) e^{-i\omega t}\,, \tag{4.2d}$$

$$\mathbf{\Psi}_{1t} = \hat{e}_{\varphi} \sum_{n=0}^{\infty} E_n j_n\left(\chi_o r\right) P_n^1\left(\cos\theta\right) e^{-i\omega t}\,, \tag{4.2e}$$

where j_n is the Spherical Bessel Functions, h_n is the Spherical Hankel Functions, $P_n(\cos\theta)$ is the Legendre Polynomial, $^1_n(\cos\theta)$ is the Associate Legendre Polynomial that has the relation of $^1_n(\cos\theta) = dP_n(\cos\theta)/d\theta$, k and χ are the longitudinal and shear wave numbers, respectively, A_n, B_n, C_n, D_n, and E_n are the series expansion coefficients of the incident, scattered, and transmitted potentials inside and outside the cell. By using the Euler's

Equation and the expression of the particle velocity in terms of the scalar potential, A_n is calculated as $A_n = \omega/(i\rho_{00}^2 k^2)C_{pn}$ where C_{pn} is represented in Eq. (4.1). Additionally, the outer and inner velocity potentials can be defined as $\phi_1^o = \phi_{inc} + \phi_{1s}$, $\overset{\text{i}}{1} = \phi_{1t}$, $\overset{\text{i}}{1} = \mathbf{\Psi}_{1s}$, and $\overset{\text{o}}{1} = \mathbf{\Psi}_{1t}$ where the superscripts "*i*" and "*o*" mean variables inside and outside the cell, respectively. In the following sections of this chapter, unless specified otherwise, no superscript of "*i*" or "*o*" indicates the acoustic variables applicable to both the inside and outside cell.

The longitudinal and shear wave numbers are defined as $k = \omega/c$ and $\chi = (i\omega\rho/\eta)^{1/2}$ [23, 50] in the fluid media both inside and outside the cell. Here, the definition of the shear wave number indicates that the shear wave is inversely dependent on the dynamic viscosity of the fluid media: i.e., the larger dynamic viscosity means the larger wave length. If the fluid is inviscid, there is no shear wave. The linear acoustic pressure p_1 and particle velocity $\mathbf{v}_1$ for a planar wave are expressed by using the Euler's equation and the definition of the velocity potentials as

$$p_1 = \frac{i\rho_0 c_0^2 k^2}{\omega}\phi_1, \tag{4.3a}$$

$$\mathbf{v}_1 = \nabla\phi_1 + \vec{\nabla}\times\mathbf{\Psi}_1, \tag{4.3b}$$

where $\mathbf{v}_1 = [v_{1r}\ v_{1\theta}]^{\mathrm{T}}$. Both the equations above are applicable for the acoustic variables inside and outside the cell.

4.2.2. Stress and Velocity Boundary Conditions

For the axisymmetric oscillation with respect to *z*-axis, the φ-direction stress

tensors at the cell surface are ignored, and thus only the stresses in the θ- and r-directions, i.e., $\sigma_{r\theta}$ and σ_{rr}, are considered. Figure 4.4 shows all the stresses applied on an infinitesimal piece of the cell membrane with a radius of a. The surface tension applied on the boundaries in the θ- and φ-direction are T_θ and T_φ, respectively. The surface displacement of a cell is defined as $\mathbf{u} = [u_r \; u_\theta]^T$ where u_r and u_θ are the displacements of the cell membrane in the r- and θ-direction, respectively. For the harmonic excitation used in this thesis, the corresponding cell surface velocities in the r- and θ-direction are calculated as $v_r = \partial u_r/\partial t = -i\omega u_r$ and $v_\theta = \partial u_\theta/\partial t = -i\omega u_\theta$, respectively.

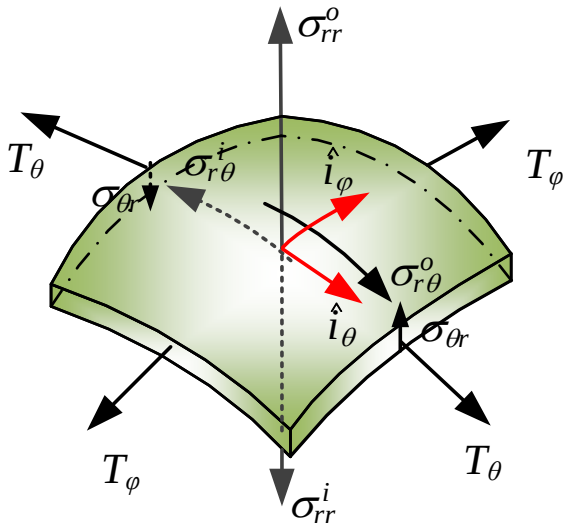

Fig. 4.4: Stresses and tensions applied on infinitesimal piece of cell membrane. In the φ-direction, the stresses are ignored due to the axisymmetric condition.

Based on the stress and tension diagram in Fig. 4.4 and the assumption of the linear oscillation of the cell surface, the first-order stress equilibrium equations in the r-

and θ-directions at the cell membrane are derived as[49,50]

$$\sigma_{rr}^{o} - \sigma_{rr}^{i} - \left(\frac{T_\theta}{R_\theta} + \frac{T_\varphi}{R_\varphi} \right) = 0 \text{ at } r = a, \tag{4.4a}$$

$$\sigma_{r\theta}^{o} - \sigma_{r\theta}^{i} + \frac{1}{a}\left(\frac{\partial T_\theta}{\partial \theta} + \cot\theta \left(T_\theta - T_\varphi \right) \right) = 0 \text{ at } r = a, \tag{4.4b}$$

where R_θ and R_φ are the principal radii of curvature, defined as[49,50]

$$\frac{1}{R_\theta} \approx \frac{1}{a}\left(1 - \frac{u_r}{a} - \frac{1}{a}\frac{\partial^2 u_r}{\partial \theta^2} \right), \tag{4.5a}$$

$$\frac{1}{R_\varphi} \approx \frac{1}{a}\left(1 - \frac{u_r}{a} - \frac{\cot\theta}{a}\frac{\partial u_r}{\partial \theta} \right). \tag{4.5b}$$

The stress tensors σ_{rr} and $\sigma_{r\theta}$ consist of the pressure and viscous stress tensors, expressed as[49,50]

$$\sigma_{rr} = -p_1 + 2\eta \frac{\partial v_{1r}}{\partial r} + (\beta - 1)\eta \vec{\nabla} \cdot \mathbf{v}_1, \tag{4.6a}$$

$$\sigma_{r\theta} = \eta \left[\frac{1}{a}\frac{\partial v_{1r}}{\partial \theta} + \frac{\partial v_{1\theta}}{\partial r} - \frac{v_{1\theta}}{a} \right], \tag{4.6b}$$

where these two equations are applicable to the fluid media inside and outside the cell. At the cell membrane, the fluid medium velocity inside and outside the cell should be continuous, providing the velocity boundary conditions at $r = a$ as

$$v_{1r}^{i}\big|_{r=a} = v_{1r}^{o}\big|_{r=a} = -i\omega u_r, \tag{4.7a}$$

$$v_{1\theta}^{i}\big|_{r=a} = v_{1\theta}^{o}\big|_{r=a} = -i\omega u_\theta. \tag{4.7b}$$

In Eq. (4.4), the surface tensions T_θ and T_φ consist of both static and dynamic

components. The static equilibrium surface tension T_0 is a constant value, and the dynamic surface tension is derived from the strain and surface moduli. Then, the surface tensions can be represented as[49,50]

$$T_\theta = T_0 + K_A\left(e_{\theta\theta} + e_{\varphi\varphi}\right) + \mu_A\left(e_{\theta\theta} - e_{\varphi\varphi}\right), \tag{4.8a}$$

$$T_\varphi = T_0 + K_A\left(e_{\theta\theta} + e_{\varphi\varphi}\right) - \mu_A\left(e_{\theta\theta} - e_{\varphi\varphi}\right), \tag{4.8b}$$

where K_A and μ_A are the surface compression and shear moduli, respectively, and $e_{\theta\theta}$ and $e_{\varphi\varphi}$ are the normal strain in the θ- and φ-directions, respectively, defined as

$$e_{\theta\theta} = \frac{1}{a}\left(u_r + \frac{\partial u_\theta}{\partial\theta}\right), \tag{4.8c}$$

$$e_{\varphi\varphi} = \frac{1}{a}\left(u_r + \cot\theta u_\theta\right). \tag{4.8d}$$

In order to consider the damping in the oscillating cell, the surface compression and shear viscosity constants η_k and η_μ are considered: i.e.,

$$\tilde{K}_A = K_A - i\omega\eta_k, \tag{4.9a}$$

$$\tilde{\mu}_A = \mu_A - i\omega\eta_\mu. \tag{4.9b}$$

The real number of the surface moduli K_A and μ_A are modified as the complex ones in Eq. (4.9) and then are substituted into Eq. (4.8).

By substituting Eqs. (4.2), (4.3), (4.5), (4.6), and (4.8) into Eqs. (4.4) and (4.7), the equation to calculate the unknown coefficients for the spherical harmonic superposition in Eq. (4.2) can be obtained as

$$\mathbf{G}_f \begin{bmatrix} B_n \\ C_n \\ D_n \\ E_n \end{bmatrix} = -A_n \mathbf{b}_f \,, \tag{4.10}$$

where the matric $\mathbf{G}_f$ and $\mathbf{b}_f$ are defined in Appendix C, and the subscript "f" represents the "fluid" media. By solving Eq. (4.10), the scattered and transmitted waves for the fluid model of the membrane enclosing the inner fluid medium can be obtained.

4.3. Cell Model of Solid Elastic Sphere

As for the model of the solid elastic sphere, the motion of the solid elastic material inside the cell or particle is described by displacement potentials, rather than the velocity potentials in the previous modeling case, while the waves outside the particle are the same as Eqs. (4.2a), (4.2b), and (4.2c). Here, the displacement vector $\mathbf{u}_1^i$ and corresponding potentials inside the particle are expressed

$$\mathbf{u}_1^i = \nabla \phi_1^i + \vec{\nabla} \times \mathbf{\Psi}_1^i \,, \tag{4.11a}$$

$$\phi_1^i = \sum_{n=0}^{\infty} D_n j_n \left(k_i r\right) P_n \left(\cos\theta\right) e^{-i\omega t} \,, \tag{4.11b}$$

$$\mathbf{\Psi}_1^i = \hat{i}_\varphi \sum_{n=0}^{\infty} E_n j_n \left(\chi_i r\right) P_n^1 \left(\cos\theta\right) e^{-i\omega t} \,, \tag{4.11c}$$

where ϕ_1^i and ψ_1^i are the longitudinal and shear displacement potentials inside the solid sphere. For the solid elastic material, the longitudinal and shear wave numbers k_i and χ_i are defined as[52]

$$k_i = \omega \sqrt{\frac{\rho_i}{\lambda + 2\mu}} \,, \tag{4.11d}$$

$$\chi_i = \omega\sqrt{\frac{\rho_i}{\mu}}\,, \tag{4.11e}$$

where λ is the Lamé's First Parameter and μ is the shear modulus. In the solid, similar to the dynamic viscosity in a fluid medium, the structural damping is an important parameter, which mainly controls the vibration amplitudes at resonant frequencies. Here, the isotropic material is assumed and thus the "complex" Young's modulus is defined as[82]

$$E^* = E\left(1 - i\eta_s\right), \tag{4.12a}$$

where η_s is the structural damping coefficient and E is the Young's modulus. The Lamé's Parameter λ and the shear modulus μ are then represented by the Young's modulus E or E^* and the Poisson's ratio ν as[52]

$$\lambda = \frac{E\nu}{\left(1+\nu\right)\left(1-2\nu\right)}, \tag{4.12b}$$

$$\mu = \frac{E}{2\left(1+\nu\right)}. \tag{4.12c}$$

At the surface of the solid elastic sphere, neither surface elastic modulus nor surface viscosity exist unlike the previous fluid cell model. The surface tension is so small that it can be ignored. Then, at the spherical surface $r = a$, the stress and velocity equilibrium equations are expressed as

$$\sigma_{rr}^{o} - \sigma_{rr}^{i} = 0 \text{ at } r = a\,, \tag{4.13a}$$

$$\sigma_{r\theta}^{o} - \sigma_{r\theta}^{i} = 0 \text{ at } r = a\,, \tag{4.13b}$$

$$v_{1r}^{i} = v_{1r}^{o} \text{ at } r = a, \tag{4.13c}$$

$$v_{1\theta}^{i} = v_{1\theta}^{o} \text{ at } r = a, \tag{4.13d}$$

where the linear stresses inside the sphere σ_{rr}^{i} and $\sigma_{r\theta}^{i}$ are defined as[52]

$$\sigma_{rr}^{i} = \lambda \vec{\nabla} \cdot \mathbf{u}_1^{i} + 2\mu \frac{\partial u_{1r}^{i}}{\partial r}, \tag{4.14a}$$

$$\sigma_{r\theta}^{i} = \mu \left[\frac{1}{a} \frac{\partial u_{1r}^{i}}{\partial \theta} + \frac{\partial u_{1\theta}^{i}}{\partial r} - \frac{u_{1\theta}^{i}}{a} \right], \tag{4.14b}$$

By substituting Eqs. (4.2a)-(4.2c), (4.3), (4.6), (4.11), and (4.14) into Eq. (4.13), the following equation is obtained.

$$\mathbf{G}_s \begin{bmatrix} B_n \\ C_n \\ D_n \\ E_n \end{bmatrix} = -A_n \mathbf{b}_s, \tag{4.15}$$

where the matrix $\mathbf{G}_s$ and vector $\mathbf{b}_s$ are defined in Appendix D, and the subscript "*s*" represents the "solid". By solving Eq. (4.15), the scattered and transmitted waves for the solid elastic sphere model can be calculated.

4.4. Frequency Responses of Two Models to Incident Plane Waves

The two models of the membrane enclosing the fluid medium and the solid elastic sphere can be used to describe the dynamic behavior of not only cells but also other liquid or solid microparticles such as gas bubbles, liquid droplets, PS beads and so on, by adjusting their modeling parameters.

Basically, a cell or microparticle has its own specific resonance frequencies. If the

acoustic waves with different frequencies are incident to the cell, the resonances with large responses are expected to be observed at the resonance frequencies, and thus the resonance frequencies can be identified for this cell. Since the resonance frequencies are highly correlated to the mechanical properties of the cell, it is possible to calculate the mechanical properties from the identified resonance frequencies. In this chapter, cancer cells with the propagating, incident plane wave are analyzed by using the developed model in the first place. Then, liquid droplets and a solid particle are investigated in this chapter.

In the following simulation to obtain the frequency responses of the cell/particle, the radius of the cell/particle is set to be a = 10 μm and the fluid medium outside the cell/particle is distilled water that is commonly used in experiments. The propagating plane wave with an acoustic pressure amplitude of 10^5 Pa is used as the excitation wave otherwise specified. The excitation frequency is normalized as ka where k is the wavenumber so that the normalized frequency is independent of the particle size.

4.4.1. Components Analysis of Plane Wave

In the study of the frequency responses, the characteristic equations in Eqs. (4.10) and (4.15) show that the resonant frequencies can be related to the spherical harmonic series number n: i.e., the n-th resonance frequency is dependent on the n-th component of the incident wave. For the standing excitation wave, the wave components are depending on the location of the particle from a pressure nodal. Therefore, for the calculation of the frequency responses, the propagating wave is used unless otherwise specified.

In Fig. 4.5, the maximum amplitude of the propagating plane wave component pressure, $C_{pn}j_n(kr)$ in Eq. (4.1) is presented. The pressure amplitude is also normalized by the incident pressure amplitude P_a. The spherical harmonic components investigated in Fig. 4.5 are n = 0, 1, 2, and 3. In the figures below, the domain of the incident acoustic pressure field is from the particle surface of $r = a$ to $r = 5a$ unless specified otherwise.

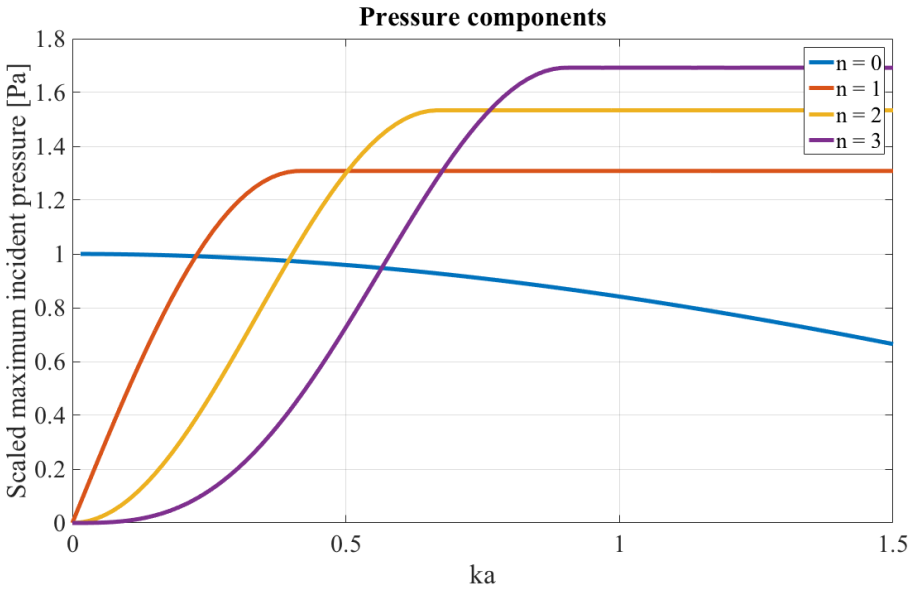

Fig. 4.5: Scaled maximum acoustic pressure components of propagating, incident plane wave. The domain for the acoustic pressure is from the sphere surface of $r = a$ to $r = 5a$.

As shown in Fig. 4.5, the pressure component for n = 0 is dominant for $ka << 1$. For example, at ka = 0.1, the scaled maximum pressure amplitudes for n = 0 and n = 1 are 0.9983 and 0.4876, respectively. Since the pressure component of n = 0 makes up the majority of the total pressure in the low frequency range of $ka << 1$, it might be difficult to observe the higher mode resonances (i.e., $n > 0$) in this frequency range. For

ka > 0.2, the acoustic pressure components of n = 1, 2 and 3 are increased rapidly and comparable to that of n = 0. Therefore, it is expected that the higher mode resonances can be observed in this frequency range.

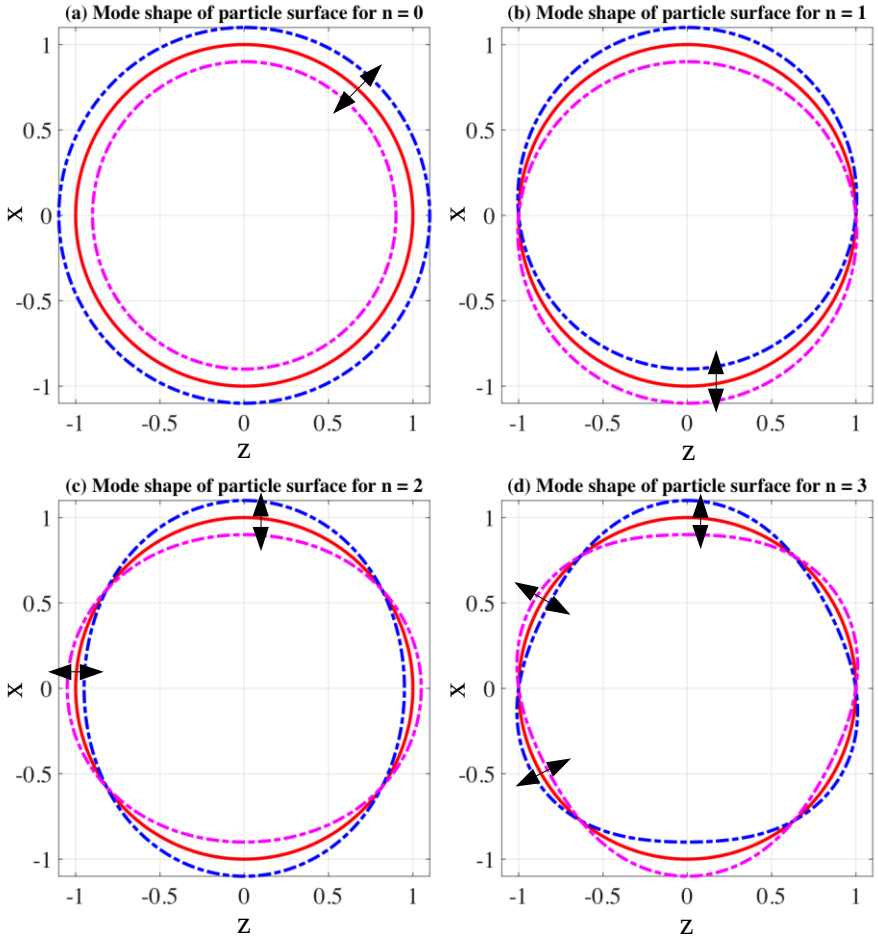

Fig. 4.6: Mode shapes of cell/microparticle surface for n = 0, 1, 2 and 3. The red solid lines represent the undeformed, original shapes and the blue and pink dashed lines represent oscillating surfaces. Here, the cell/microparticle radius is set to be 1 and the oscillation amplitude is assumed to be 0.1.

The first three mode shapes (i.e., n = 1 to 3) of the vibrating cell/microparticle

surface are shown in Fig. 4.6. For n = 0, the surface oscillates uniformly in the radial direction. For n = 1, 2 and 3, there are nodes (where the vibration amplitude is always zero) at the surface. In general, the compressibility of cells/microparticles is mainly related to the mode shape of n = 0 since the volume change associated with the mode shapes of n = 1, 2 and 3 can be ignored. Here, the surface oscillation amplitudes can be determined by using the excitation acoustic pressure components.

4.4.2. Model of Solid Elastic Sphere

For the rough but simple prediction of human cancer cells' resonances, the solid elastic sphere model can be used for the prediction of the cancer cells' dynamic behaviors although the fluid model may result in more accurate prediction than the solid elastic sphere model. This model has also been be used to study other cells or some small bacteria[51] which can be properly modeled as a solid elastic sphere. In addition, artificial solid particles can be analyzed well by this model.

As shown in Fig. 4.7, one typical human breast cancer cell, MCF-7, modeled as a solid elastic sphere is studied here. Although this solid elastic model cannot be used to accurately describe the dynamic behavior of the cell, this simple model can give some insights on the dynamic behavior, which will be presented below. According to Ref. 83, the Young's modulus and Poisson's ratio of this cell are approximately 1.1×10^3 Pa and 0.5, respectively. The density of MCF-7 is reported as 1068 kg/m^3.[74] In order to avoid the singularity at the Poisson's ratio of 0.5, the value of 0.49 is used here instead of 0.5. Since the structural damping for this cell model is not well known, three structural damping values of 0.001, 0.005, and 0.01 are used in this study.

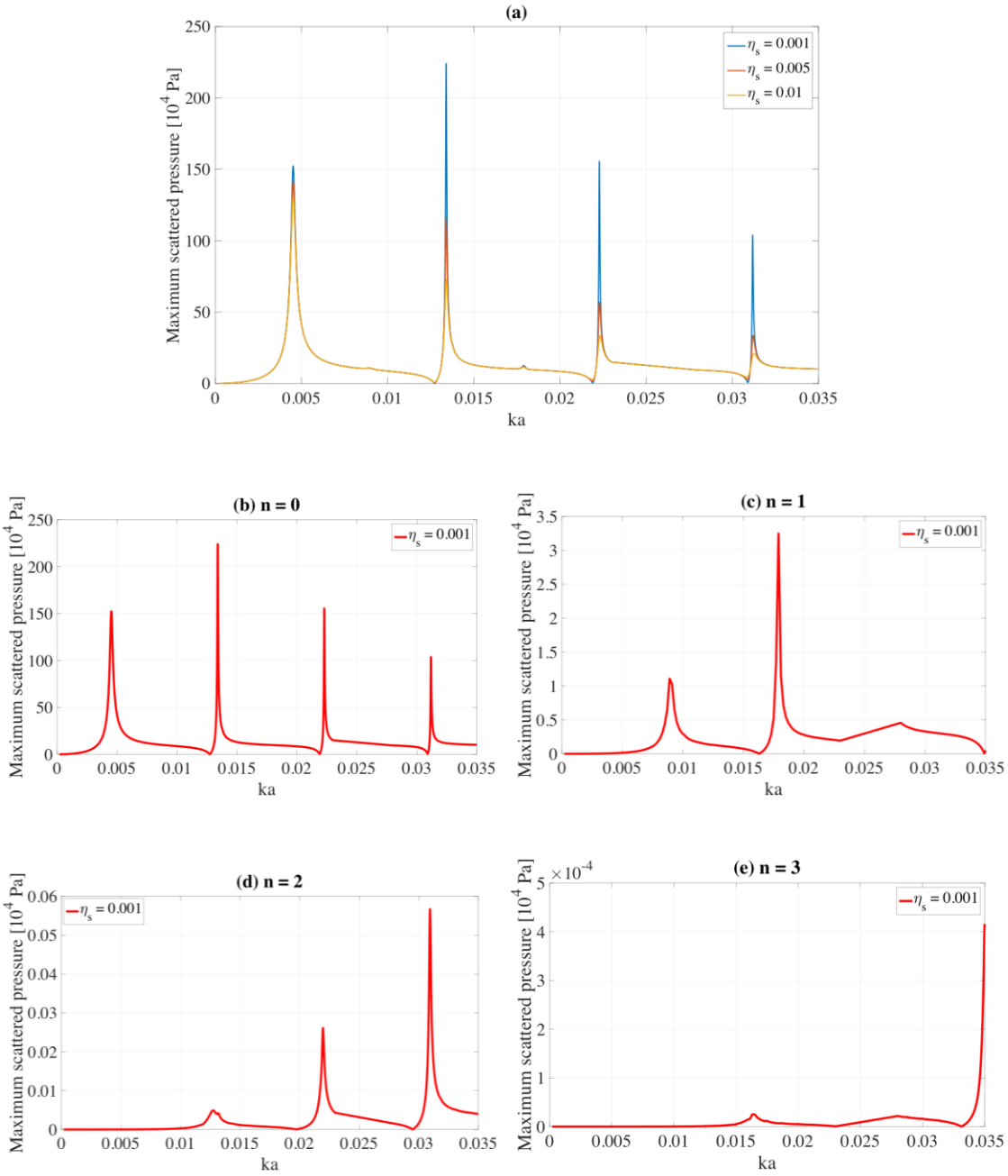

Fig. 4.7: Maximum scattered acoustic pressure of MCF-7 human breast cancer cell modeled as solid elastic sphere. (a) Maximum scattered acoustic pressure amplitudes for structural damping coefficients of 0.001, 0.005, and 0.01. (b)-(e) Amplitudes of maximum scattered acoustic pressure components for n = 0, 1, 2, and 3.

As shown in Fig. 4.7(a), the larger structural damping coefficient η_s results in the smaller acoustic pressure amplitude at a resonance frequency while the resonance frequencies remain unchanged. For a small η_s, the acoustic pressure amplitudes at the resonant frequencies can be identified easily due to their high quality factors, while for a large η_s, it is difficult to clearly observe the resonance frequencies, in particular, in the high frequency region. In Fig. 4.7(a), the resonances are observed at ka = 0.00433, 0.01284, 0.02137, and 0.0299 which are corresponding to f = 102.1, 302.7, 503.8, and 705.0 kHz, respectively. From the results in Figs. 4.7(b) - 4.7(e), it can be observed that the resonances occur at all the components of interest (i.e., n = 0, 1, 2, and 3). However, the resonant acoustic pressures for n = 1, 2 and 3 are very small in their magnitudes when compared with that of n = 0. Thus, it can be concluded that the resonances in Fig. 4.7(a) are mainly resulted in from the scattered acoustic pressure at n = 0. This observation is also in line with the excitation acoustic pressure components in Sec. 4.4.1.

For a real solid elastic particle, like PS beads, the frequency response is quite different from that of the cancer cell due to the large difference in their compressibity. The density, Young's modulus and Poisson's ratio of the PS beads are 1050 kg/m^3, 3.4 GPa, and 0.35[85], respectively. Here, the damping coefficient is set to be η_s = 0.001. In Fig. 4.8, the clear resonances can be determined at ka = 1.418 and 2.085 for n = 2 and n = 3, respectively. Figure 4.8(b) shows no resonance for n = 0 in the frequency range ka = [1, 2.5]. In Fig. 4.8(c), there is a resonance but the pressure amplitude is too small. Here, the large Young's modulus of the PS bead increases the resonant frequencies when compared with the resonance frequencies of the breast cancer cells in Figs. 4.7 and 4.8.

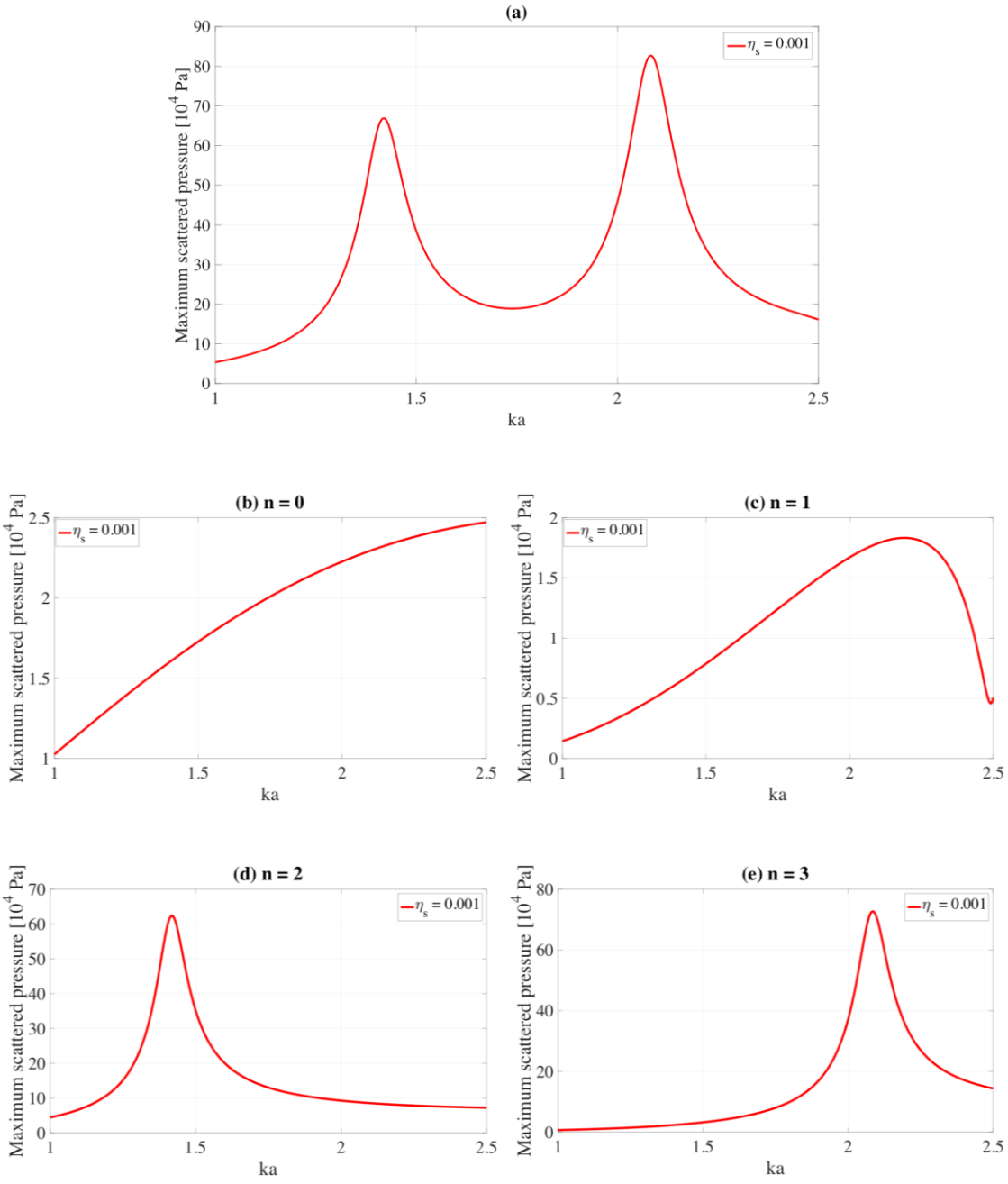

Fig. 4.8: Maximum scattered acoustic pressure for PS bead modeled as solid elastic sphere. (a) Maximum scattered pressure amplitude. (b)-(e) Amplitudes of maximum scattered acoustic pressure components for n = 0, 1, 2, and 3. The resonances are observed only for n = 2 and n = 3.

4.4.3. Model of Simple Liquid Droplet

In addition to the the solid elastic sphere model, the MCF-7 breast cancer cell can also be modeled as a simple liquid droplet with only static surface tension and a uniform fluid medium inside. This model can be used to describe the dynamic behavior of the cell more accurately than the solid elastic model. For a typical cell, its static surface tension is assumed to be 0.2 N/s[43]. The inner fluid medium density of the cell is set to be 1068 kg/m^3[74] like the density of the solid elastic model. The dynamic viscosity and sound speed of the inner fluid medium is assumed to be the same as in distilled water.

Figure 4.9 shows the maximum pressure amplitude as a function of *ka*. Unlike the results in Fig. 4.7, the dynamic response of the simple liquid droplet model has only one small resonance peak due to a large viscous damping in the inner fluid. From the acoustic pressure components in Figs. 4.9(b)-4.9(e), it is observed that there is also one resonance only for each of n = 2 and n = 3, which agrees with the resonance frequency estimation for an inviscid liquid droplet represented as[50]

$$\omega_{Tn}^2 = \frac{(n-1)n(n+1)(n+2)T_0}{\left[(n+1)\rho_i + n\rho_0\right]a^3}. \tag{4.16}$$

By using Eq. (4.16), the resonant frequencies are calculated as ka = 0.006483 (n = 2) and 0.01226 (n = 3). As shown in Fig. 4.9, the resonant frequencies estimated by using the simple liquid droplet model are 0.00601 and 0.01152 for n = 2 and n = 3, respectively. There are slight discrepancies between these two modeling data. These difference may be caused by the dynamic viscosity of the fluid medium, which is not included in the modeling procedure for Eq. (4.16).

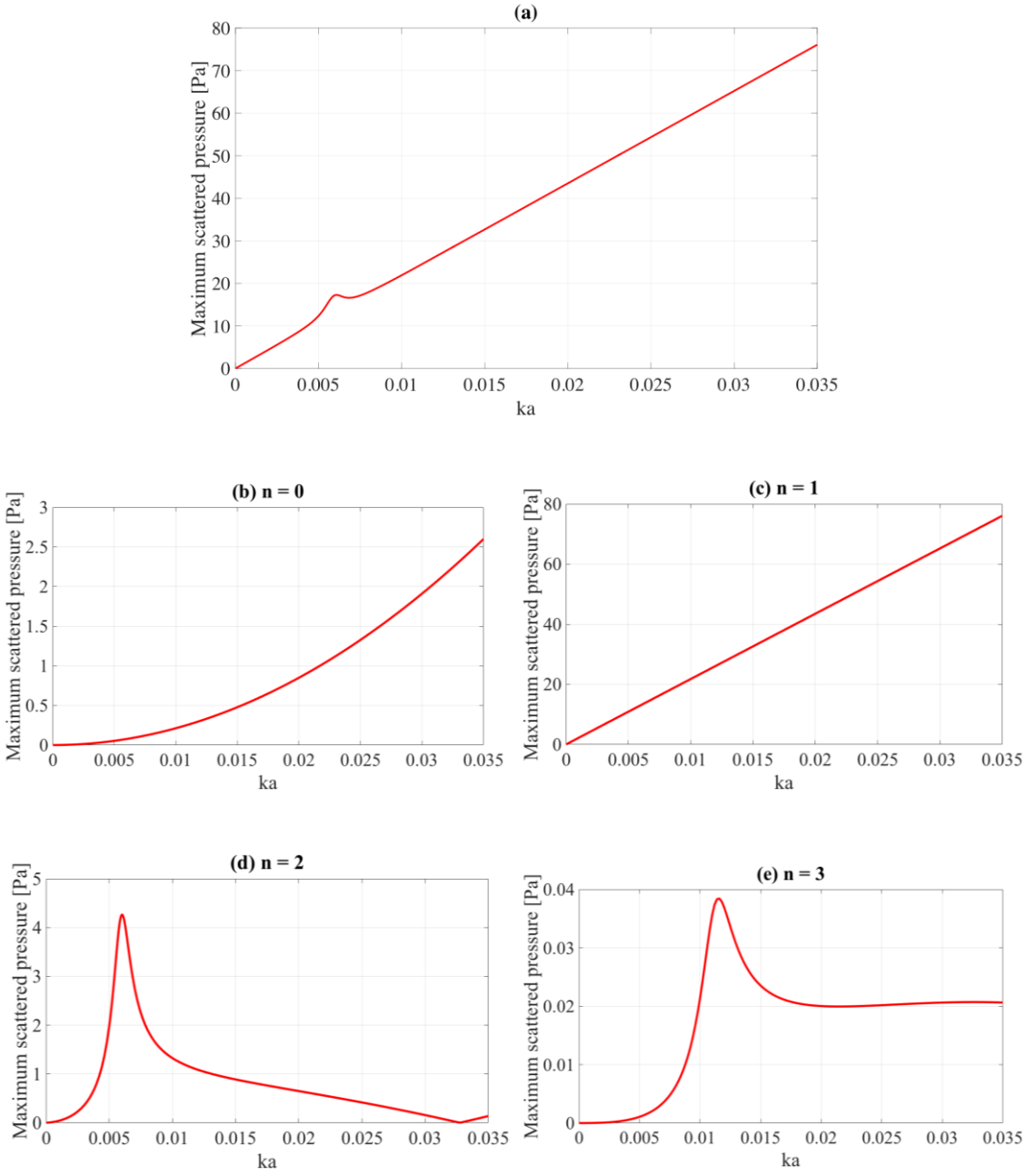

Fig. 4.9: Maximum scattered acoustic pressure of MCF-7 human breast cancer cell model as simple liquid droplet model with surface tension T_0 = 0.2 N/m. (a) Total maximum scattered acoustic pressure. (b)-(e) Amplitudes of maximum scattered acoustic pressure components for n = 0, 1, 2, and 3. Only one resonant frequency can be observed although its amplitude is significantly small when compared with the results in Fig. 4.7.

In Fig. 4.9, the maximum pressure amplitudes for $n = 2$ and $n = 3$ are much smaller than that for $n = 0$ and $n = 1$. Therefore, even there are resonances for $n > 1$, the small acoustic pressure responses make these resonances difficult to be observed in the total maximum acoustic pressure in Fig. 4.9(a). Note that the estimated resonance frequencies are in the same order of magnitude as those obtained with the solid elastic sphere model.

4.4.4. Model of Complex Membrane Enclosing Fluid Medium

For the precise analysis of the cell's dynamic behavior, it is insufficient to use the only static surface tension T_0 for the description of the cell membrane. Thus, the viscoelastic properties need to be included with six additional parameters: the dynamic surface tension, the surface compression and shear moduli, the surface compression and shear viscosity. Here, it is difficult to identify all these parameters for a cell by observing its resonant frequencies because the high order resonances are difficult to be generated and observed experimentally. Thus, although it is more sophisticated to utilize all the seven parameters to describe the cell membrane, in reality, either some parameters are estimated from literatures or are ignored if the effects of these parameters on the dynamic behavior are insignificant. In the following simulation results, the only static surface tension and surface compression and shear moduli are considered instead of all the seven parameters. Then, the surface compression and shear moduli are added to the parameters of the simple model in Section 4.4.3. In addition, it is assumed that the surface compression modulus K_A is three times higher than the surface shear modulus μ_A, $K_A = 3\mu_A$[50]: i.e., $K_A = 1.45$ N/s.

In Fig. 4.10, the frequency response shows the resonant frequency at ka = 0.006 for n = 1, which is coincident with the modeling results in Section 4.4.3 although the pressure amplitude is much larger than that in Fig. 4.9. In addition, the corresponding component number is n = 2 for the simple liquid droplet model and n = 1 for the complex fluid model, respectively. The resonant frequencies for n = 2 and 3 are ka = 0.0115 and 0.0167, respectively as shown in Figs. 4.10(d) and 4.10(e). With the addition of the surface compression and shear moduli, the resonant frequencies, at ka = 0.00601 and ka = 0.01152 for n = 2 and n = 3, of the simple fluid model are shifted to ka = 0.0115 and ka = 0.0167 for n = 2 and n = 3 for the complex fluid model. In Fig. 4.10, the pressure amplitude for n = 1 is dominant when compared with the other components for n = 0, 2 and 3.

According to Ref 50, the individual resonant frequencies corresponding to K_A and μ_A are expressed as

$$\omega_{Kn}^2 = \frac{n(n+1)K_A}{\left[(n+1)\rho_i + n\rho_0\right]a^3}. \tag{4.17a}$$

$$\omega_{\mu n}^2 = \frac{(n-1)(n+2)\mu_A}{\left[(n+1)\rho_i + n\rho_0\right]a^3}. \tag{4.17b}$$

By using the Eq. (4.17) and the modeling parameters of K_A = 1.45 N/s and μ_A = K_A/3, the resonant frequencies are calculated as ka_{Kn} = [0, 0.006491, 0.008728, 0.01044] and $ka_{\mu n}$ = [0, 0, 0.004114, 0.005503] where the values in the brackets are associated with the component number n = 0, 1, 2, and 3. From Eqs. (4.16) and (4.17), there are no resonance for n = 0. The resonance for n = 1 is resulted in mainly from K_A and the

resonances for $n > 1$, from T_0, K_A and μ_A.

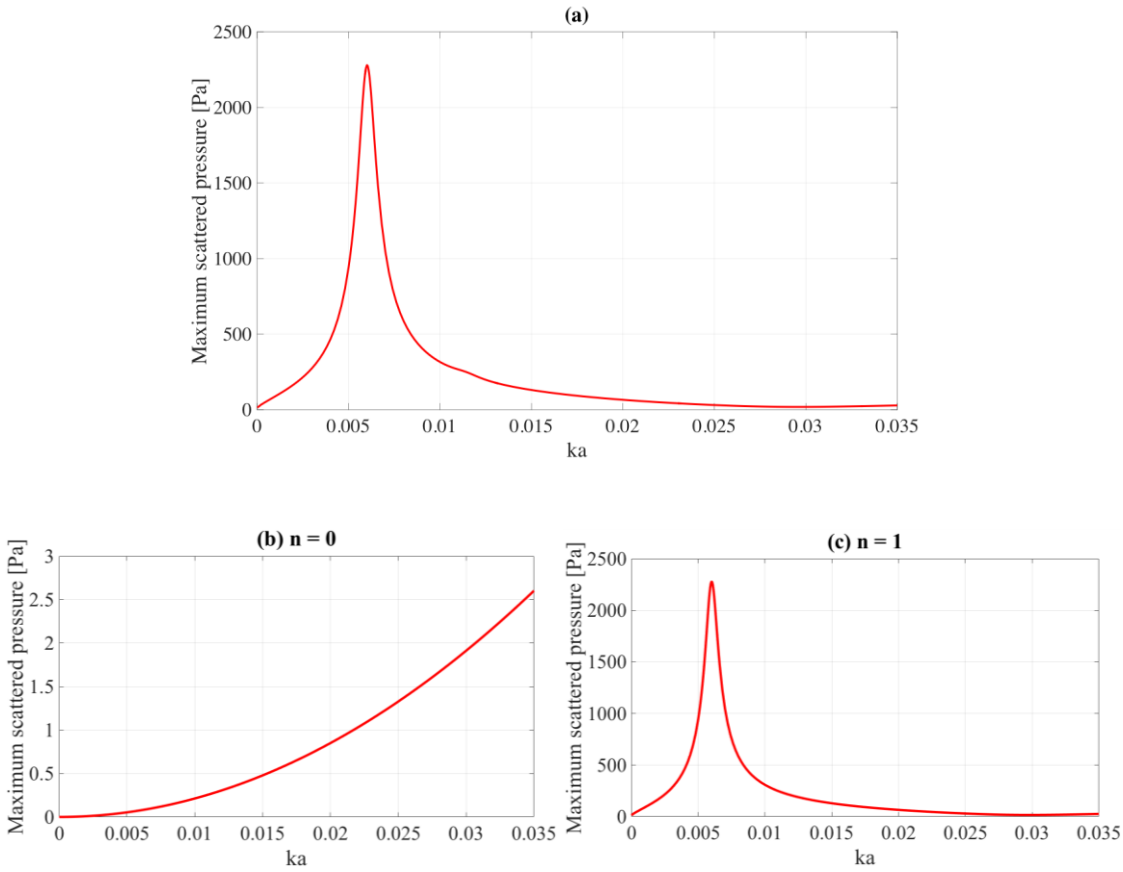

Fig. 4.10: Maximum scattered acoustic pressure amplitude of MCF-7 breast cancer cell modeled as membrane enclosing inner fluid (referred to as complex fluid model) with K_A = 1.45 N/m and T_0 = 0.2 N/m. (a) Total maximum scattered acoustic pressure. (b)-(e) Amplitudes of maximum scattered acoustic pressure components for n = 0, 1, 2, and 3.

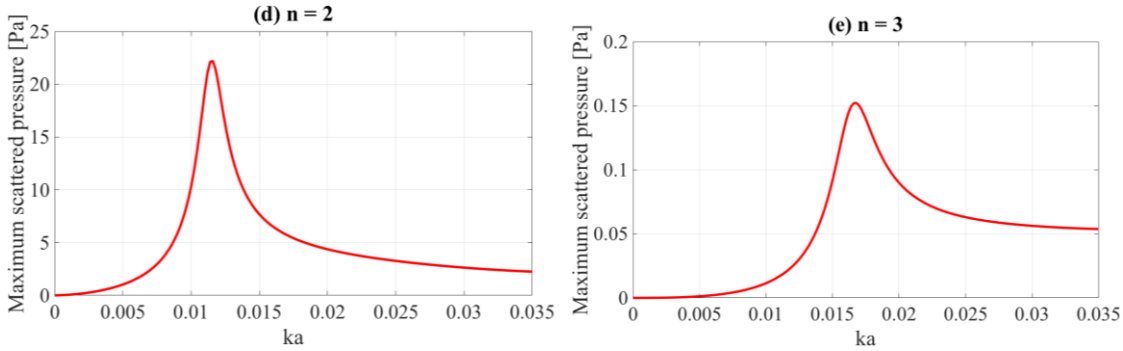

Fig. 4.10: Continued.

For n = 1, the resonant frequency ka_{Kn} = 0.006491 agrees well with the frequency identified by using the simple fluid model in Sec. 4.4.3 with the small frequency difference induced by the dynamic viscosity. For n > 1, all the parameters of T_0, K_A and μ_A work together to result in the resonant frequencies that are different from the resonance frequencies estimated by using Eqs. (4.16) and (4.17). For example, for n = 2, the resonance frequency for the complex fluid model is ka = 0.0115, while the resonant frequencies calculated from Eqs. (4.16) and (4.17) are ka_{Kn} = 0.008728, $ka_{\mu n}$ = 0.004114, ka_{Tn} = 0.006483. It is obvious that the coupling between the parameters of T_0, K_A and μ_A generates new resonance frequencies.

4.5. Conclusion

In this chapter, the dynamic behaviors of the PS bead and the breast cancer cell are analyzed by modeling them as the solid and fluid spheres. From the frequency responses of the different models to the planar, acoustic excitation, it is observed that the resonances can be identified where the scattered acoustic pressure has the peak values. It is also observed that the resonance frequencies are highly correlated with the

properties of the specific models. From the model of the membrane enclosing the inner fluid medium, it is shown that the coupling of the modeling parameters possibly generates the resonant frequencies.

5. ACOUSTIC STREAMING AROUND MICROPARTICLE*

The acoustic streaming governing equation is difficult to be solved directly and accurately. In this chapter, the Doinikov's approach[23] has been improved by decomposing the acoustic streaming into compressional and shear components depending on the inside and outside of the viscous boundary layer around a cell/microparticle of arbitrary size to accurately and computationally efficiently calculate the acoustic streaming. Then, the governing equations of the acoustic streaming are decomposed into the homogenous and particular ones for the calculation of the compressional and shear components, respectively. The decomposed governing equations are then solved separately. The total acoustic streaming is then obtained by combining both the compressional and shear components.

Since the acoustic streaming outside a cell/microparticle is of our interest, only the streaming outside the cell/microparticle is derived and calculated. In this chapter, all the variables are related to the fluid medium outside the cell/microparticle. The acoustic streaming results obtained by using the proposed algorithm around a solid elastic particle and a liquid droplet are compared with those calculated by using the Doinikov's method, and the frequency responses of their acoustic streaming are also investigated.

5.1. Calculation of Acoustic Streaming

The proposed method for the calculation of the acoustic streaming generated

* Portions of this chapter have been reprinted from with the permission of the Institute of Noise Control Engineering of the USA from Z. Liu and Y.-J. Kim, "Acoustic streaming around a spherical microparticle/cell under ultrasonic wave excitation," *Proceedings of Inter-Noise 2015*, San Francisco, California, USA, 2015.[102]

around a cell/microparticle under an ultrasonic wave excitation is outlined in Fig. 5.1. Based on the linear oscillation solution of the fluid medium around a particle[23,52,84], the acoustic streaming is solved from the second-order time-independent governing equations when the ultrasonic excitation is at a frequency of ω.

The interaction of the particle with the incident wave generates a thin viscous boundary layer $\delta_v = (2\eta/\rho_0/\omega)^{1/2}$ [23] around the particle's surface, where η is the dynamic viscosity of the fluid and ρ_0 is the fluid density. Inside this layer, the spatial change rate of velocities is significant and thus the fluid viscosity is dominant, while the fluid medium can be inviscid outside this layer. In this case, the acoustic streaming is decomposed based on the viscous boundary layer.

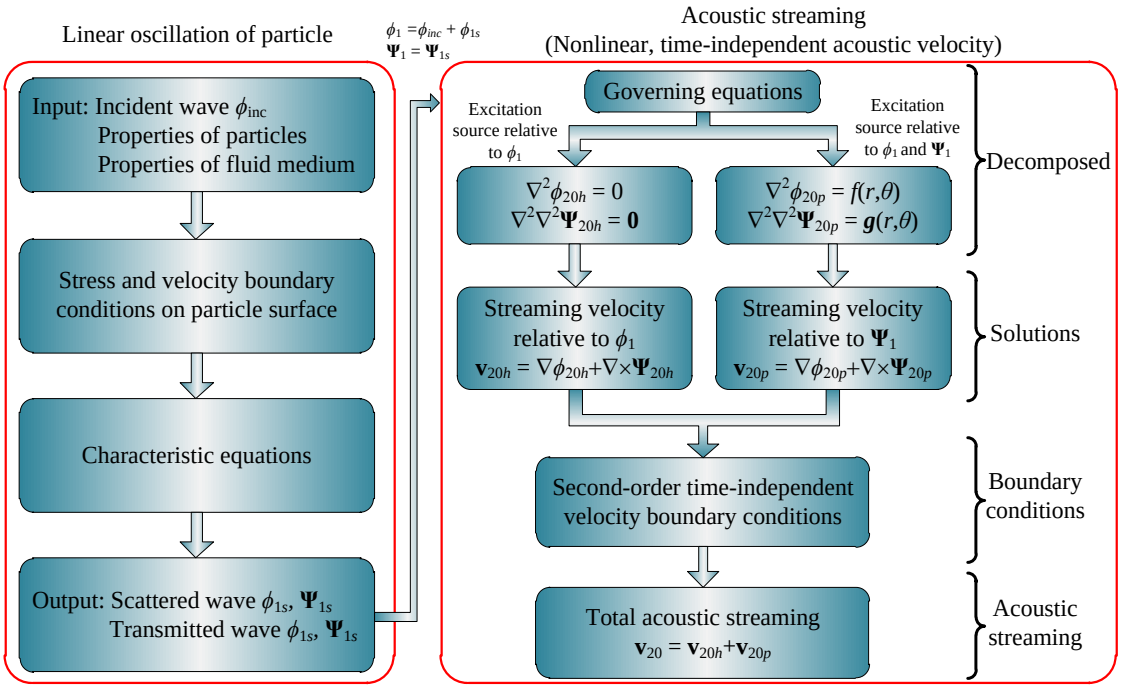

Fig. 5.1: Framework for calculation of acoustic streaming generated around cell/microparticle under ultrasonic wave excitation.[102]

5.1.1. Decomposition of Acoustic Streaming Governing Equations

The first-order acoustic particle velocity vector $\mathbf{v}_1$ can be decomposed into the first-order scalar potential ϕ_1 and vector potential $\mathbf{\Psi}_1$ as

$$\mathbf{v}_1 = \mathbf{v}_{1\phi} + \mathbf{v}_{1\psi}, \tag{5.1a}$$

$$\mathbf{v}_{1\phi} = \vec{\nabla}\phi_1, \tag{5.1b}$$

$$\mathbf{v}_{1\psi} = \vec{\nabla} \times \mathbf{\Psi}_1, \tag{5.1c}$$

where ϕ_1 includes the incident and scattered scalar potential and $\mathbf{\Psi}_1$ is purely the scattered vector potential, and the corresponding first-order velocities are $\mathbf{v}_{1\phi}$ and $\mathbf{v}_{1\psi}$, respectively. The scalar potential ϕ_1 is related to acoustic pressure (or compressional) waves, that are present inside and outside the viscous boundary layer. For a pressure wave, the fluid viscosity can be ignored in a finite domain (e.g., within a few wavelengths), and thus the corresponding velocity $\mathbf{v}_{1\phi}$ is considered as an inviscid acoustic particle velocity in the nearfield of the spherical particle surface. On the contrary, the vector potential $\mathbf{\Psi}_1$ represents a shear wave and is only significant in the vicinity of the spherical particle surface where the spatial change rate of velocities is not negligible. The shear velocity vector $\mathbf{v}_{1\psi}$ is dominant in the range of a few δ_v from the particle surface.

By substituting the decomposed, first-order acoustic particle velocity in Eq. (5.1a) into Eq. (2.11), the excitation sources of the acoustic streaming, i.e., the right-hand side (RHS) of Eq. (2.11), can also be decomposed into two components: one source is purely related to $\mathbf{v}_{1\phi}$, and the other, to $\mathbf{v}_{1\psi}$ and the product of $\mathbf{v}_{1\phi}$ and $\mathbf{v}_{1\psi}$: i.e.,

$$\vec{\nabla}\cdot\mathbf{v}_{20h}=-\frac{1}{\rho_0}\vec{\nabla}\cdot\left\langle\rho_1\mathbf{v}_{1\phi}\right\rangle, \tag{5.2a}$$

$$\nabla^2\left(\vec{\nabla}\times\mathbf{v}_{20h}\right)=\frac{\rho_0}{\eta}\vec{\nabla}\times\left\langle\mathbf{v}_{1\phi}\left(\vec{\nabla}\cdot\mathbf{v}_{1\phi}\right)+\left(\mathbf{v}_{1\phi}\cdot\vec{\nabla}\right)\mathbf{v}_{1\phi}\right\rangle, \tag{5.2b}$$

$$\vec{\nabla}\cdot\mathbf{v}_{20p}=-\frac{1}{\rho_0}\vec{\nabla}\cdot\left\langle\rho_1\mathbf{v}_{1\psi}\right\rangle, \tag{5.3a}$$

$$\begin{aligned}\nabla^2\left(\vec{\nabla}\times\mathbf{v}_{20p}\right)=\frac{\rho_0}{\eta}\vec{\nabla}\times\Big\langle&\mathbf{v}_1\left(\vec{\nabla}\cdot\mathbf{v}_{1\psi}\right)+\mathbf{v}_{1\psi}\left(\vec{\nabla}\cdot\mathbf{v}_{1\phi}\right)\\&+\left(\mathbf{v}_1\cdot\vec{\nabla}\right)\mathbf{v}_{1\psi}+\left(\mathbf{v}_{1\psi}\cdot\vec{\nabla}\right)\mathbf{v}_{1\phi}\Big\rangle\end{aligned}. \tag{5.3b}$$

In Eqs. (5.2) and (5.3), the two excitation sources decompose the acoustic streaming velocity into two components, $\mathbf{v}_{20} = \mathbf{v}_{20h} + \mathbf{v}_{20p}$ where the subscript "*h*" represents the velocity component associated with $\mathbf{v}_{1\phi}$, and the subscript "*p*" represents the components related to $\mathbf{v}_{1\psi}$ and the product of $\mathbf{v}_{1\phi}$ and $\mathbf{v}_{1\psi}$: i.e.,

$$\mathbf{v}_{20}=\mathbf{v}_{20h}+\mathbf{v}_{20p}, \tag{5.4a}$$

$$\mathbf{v}_{20h}=\vec{\nabla}\phi_{20h}+\vec{\nabla}\times\boldsymbol{\Psi}_{20h}, \tag{5.4b}$$

$$\mathbf{v}_{20p}=\vec{\nabla}\phi_{20p}+\vec{\nabla}\times\boldsymbol{\Psi}_{20p}. \tag{5.4c}$$

As shown in the following section, it is proved that the excitation source related to $\mathbf{v}_{1\phi}$ becomes zero, resulting in that $\mathbf{v}_{20h}$ and $\mathbf{v}_{20p}$ are the homogeneous and particular solutions of Eq. (2.11), respectively. Considering the effective domains of the individual excitation sources, it is concluded that $\mathbf{v}_{20h}$ exists inside and outside the viscous boundary layer while $\mathbf{v}_{20p}$ is only significant in the vicinity of the particle surface.

5.1.2. Homogeneous Acoustic Streaming Solution Vector: v_{20h}

As discussed previously, the first-order acoustic particle velocity $\mathbf{v}_{1\phi}$ associated with the scalar velocity potential is inviscid, leading to the fact that the pressure wave number k is a real number. Then, the inviscid Euler's Equation[23] and the Helmholtz Equation can be represented, respectively, as

$$\hat{\rho}_1 = i\rho_0 k^2 \hat{\phi}_1 / \omega, \tag{5.5}$$

$$\nabla^2 \hat{\phi}_1 = -k^2 \hat{\phi}_1, \tag{5.6}$$

where the hat "^" represents a complex amplitude in frequency domain.

By plugging Eqs. (5.1b), (5.5), and (5.6) into the Right-hand side (RHS) of Eq. (5.2a), the LHS is simplified as

$$\begin{aligned} -\frac{1}{\rho_0}\vec{\nabla}\cdot\left\langle \rho_1 \mathbf{v}_{1\phi} \right\rangle &= -\frac{1}{\rho_0}\left\langle \vec{\nabla}\rho_1 \cdot \mathbf{v}_{1\phi} + \rho_1 \vec{\nabla}\cdot \mathbf{v}_{1\phi} \right\rangle \\ &= -\frac{1}{2}\mathrm{Re}\left[\left(\frac{ik^2}{\omega}\vec{\nabla}\hat{\phi}_1 \right)\cdot(\vec{\nabla}\hat{\phi}_1)^* \right] - \frac{1}{2}\mathrm{Re}\left[\left(\frac{ik^2}{\omega}\hat{\phi}_1 \right)(\nabla^2\hat{\phi}_1)^* \right], \\ &= -\frac{1}{2}\mathrm{Re}\left[\frac{ik^2}{\omega}(\vec{\nabla}\hat{\phi}_1)\cdot(\vec{\nabla}\hat{\phi}_1)^* \right] + \frac{1}{2}\mathrm{Re}\left[\frac{ik^4}{\omega}(\hat{\phi}_1)(\hat{\phi}_1)^* \right] \\ &= 0 \end{aligned} \tag{5.7}$$

where the asterisk "*" represents the complex conjugate. Therefore, Eq. (5.2a) can be rewritten as

$$\vec{\nabla}\cdot\mathbf{v}_{20h} = 0. \tag{5.8}$$

Then, the velocity vector $\mathbf{v}_{20h}$ can be expressed only by the vector potential: i.e,

$$\mathbf{v}_{20h} = \vec{\nabla}\times\mathbf{\Psi}_{20h}, \tag{5.9}$$

which satisfies Eq. (5.8). That is, the homogeneous scalar potential ϕ_{20h} can be a constant: i.e.,

$$\phi_{20h} = \text{constant}\,. \tag{5.10}$$

By plugging Eqs. (5.1b), (5.5), and (5.6) into the RHS of Eq. (5.2b), the first term of the RHS is simplified as

$$\begin{aligned}\vec{\nabla}\times\left\langle \mathbf{v}_{1\phi}\left(\vec{\nabla}\cdot\mathbf{v}_{1\phi}\right)\right\rangle &= \left\langle\left(\vec{\nabla}\times\mathbf{v}_{1\phi}\right)\left(\vec{\nabla}\cdot\mathbf{v}_{1\phi}\right)+\vec{\nabla}\left(\vec{\nabla}\cdot\mathbf{v}_{1\phi}\right)\times\mathbf{v}_{1\phi}\right\rangle \\ &= \frac{1}{2}\mathrm{Re}\left[\left(\vec{\nabla}\times\hat{\mathbf{v}}_{1\phi}\right)\left(\vec{\nabla}\cdot\hat{\mathbf{v}}_{1\phi}\right)^{*}\right]+\frac{1}{2}\mathrm{Re}\left[\vec{\nabla}\left(\vec{\nabla}\cdot\hat{\mathbf{v}}_{1\phi}\right)\times\left(\hat{\mathbf{v}}_{1\phi}\right)^{*}\right] \\ &= \mathbf{0}-\frac{1}{2}\mathrm{Re}\left[k^{2}\left(\vec{\nabla}\hat{\phi}_{1}\right)\times\left(\vec{\nabla}\hat{\phi}_{1}\right)^{*}\right] \\ &= \mathbf{0}\end{aligned}. \tag{5.11}$$

For the second term of RHS in Eq. (5.2b), the vector identity of $(\mathbf{A}\cdot\nabla)\mathbf{A} = \nabla(\mathbf{A}\cdot\mathbf{A})/2 - \mathbf{A}\times(\nabla\times\mathbf{A})$ can be applied as

$$\vec{\nabla}\times\left\langle\left(\mathbf{v}_{1\phi}\cdot\vec{\nabla}\right)\mathbf{v}_{1\phi}\right\rangle = \vec{\nabla}\times\left\langle\frac{1}{2}\nabla\left(\mathbf{v}_{1\phi}\cdot\mathbf{v}_{1\phi}\right)-\mathbf{v}_{1\phi}\times\left(\vec{\nabla}\times\mathbf{v}_{1\phi}\right)\right\rangle = \mathbf{0}\,. \tag{5.12}$$

By plugging Eqs. (5.11) and (5.12) into Eq. (5.2b), Eq. (5.2b) can be rewritten as

$$\nabla^{2}\left(\vec{\nabla}\times\mathbf{v}_{20h}\right) = \mathbf{0}\,. \tag{5.13}$$

Therefore, $\mathbf{v}_{20h}$ is the homogeneous solution of Eq. (2.11). The governing equation for the homogeneous vector potential $\boldsymbol{\Psi}_{20h}$ is then derived from Eqs. (5.9) and (5.13) as

$$\nabla^{2}\nabla^{2}\boldsymbol{\Psi}_{20h} = \mathbf{0}\,, \tag{5.14}$$

which is a homogeneous Biharmonic Equation. In the axisymmetric case, the solution to Eq. (5.14) can be represented as

$$\boldsymbol{\Psi}_{20h} = \sum_{n=0}^{\infty}\left(C_{1n}z^{-(n-1)} + C_{2n}z^{-(n+1)} + C_{3n}z^{n} + C_{4n}z^{n+2}\right)P_n^1\left(\cos\theta\right), \tag{5.15}$$

where $z = r/a$, a is the radius of the particle, r and θ are the radial distance and polar angle in the spherical coordinate system, respectively, and $\frac{1}{n}(\cos\theta)$ is the associated Legendre Polynomials. (For the detailed derivation of Eq. (5.15), see Appendix E).

By applying the boundary condition of $\nabla\times\boldsymbol{\Psi}_{20h} \to 0$ as $z \to \infty$ to Eq. (5.15), the coefficients of C_{3n} and C_{4n} should be zero: i.e.,

$$C_{3n} = 0,\ C_{4n} = 0. \tag{5.16}$$

The coefficients of C_{1n} and C_{2n} will be determined from the boundary conditions on the cell/microparticle surface in the following section.

Eq. (5.15) describes the analytical acoustic streaming outside the viscous boundary layer. Since the coefficients C_{1n} and C_{2n} are constant, the outer acoustic streaming can be calculated in a relatively short computational time.

5.1.3. Particular Acoustic Streaming Solution: v_{20p}

The particular acoustic streaming solution vector $\mathbf{v}_{20p}$ consisting of the scalar potential ϕ_{20p} and vector potential $\boldsymbol{\Psi}_{20p}$ in Eq. (5.4c) can be found by solving Eqs. (5.3a) and (5.3b), respectively, using a modified Doinikov's method, although the original Doinikov's method[23] was used to solve the total solution including both the homogeneous and particular solutions. The basic idea of the Doinikov's method is to decompose the excitation source into a serial of Legendre polynomials and then solve the decomposed equations order by order using the orthogonality of these polynomials.

Note that the velocity $\mathbf{v}_{20p}$ is only significant in the vicinity of the particle surface. For the implementation of this method, at $r = a+10\delta_v$, $\mathbf{v}_{20p}$ is significantly small and can be ignored, which provides a boundary condition for ϕ_{20p} and $\mathbf{\Psi}_{20p}$. In addition, the product of $\mathbf{v}_{1\psi}$ and any other variable can be ignored at $r > a+10\delta_v$. Therefore, all the integrals in calculating the particular solution vector $\mathbf{v}_{20p}$ are accurate enough in the range of $[a \;\; a+10\delta_v]$, rather than the limit of $[a, \infty]$ that was originally proposed by Doinikov. This short integral range reduces the computational time significantly. Here, z_∞ is then defined as

$$z_\infty = 1+10\,\delta_v / a \,. \tag{5.17}$$

a) Solution Procedure for Particular, Scalar Acoustic Streaming Potential: ϕ_{20p}

By plugging Eq. (5.4c) into Eq. (5.3a), the partial differential equation for ϕ_{20p} can be expressed as

$$\nabla^2 \phi_{20\,p} = -\frac{1}{\rho_0}\vec{\nabla}\cdot\left\langle \rho_1 \mathbf{v}_{1\psi} \right\rangle . \tag{5.18}$$

By using the procedure proposed by Doinikov, the LHS of Eq. (5.18) is expressed in a series of the Legendre polynomials as[23]

$$\frac{1}{\rho_0}\vec{\nabla}\cdot\left\langle \rho_1 \mathbf{v}_{1\psi} \right\rangle = \sum_{n=0}^{\infty} \frac{2n+1}{a^2}\,\mu_n(z)\,P_n(\cos\theta), \tag{5.19a}$$

where

$$\mu_n = \frac{a^2}{2\rho_0}\int_0^{\pi} \vec{\nabla}\cdot\left\langle \rho_1 \mathbf{v}_{1\psi} \right\rangle P_n(\cos\theta)\sin\theta\, d\theta, \tag{5.19b}$$

$P_n(\cos\theta)$ is the Legendre polynomials. Here, $\mu_n(z)$ is only present in the vicinity of the particle surface, $\mu_n(z) \rightarrow 0$ at $z = z_\infty$. Based on the expansion in Eq. (5.19a), ϕ_{20p} is also expanded with the Legendre polynomials as

$$\phi_{20p} = \sum_{n=0}^{\infty} \phi_{20pn}(z) P_n(\cos\theta). \tag{5.20}$$

By substituting Eqs. (5.19) and (5.20) into Eq. (5.18) and omitting the terms of $P_n(\cos\theta)$, the equation for the expansion coefficient $\phi_{20pn}(z)$ is obtained as

$$\partial_{zz}\phi_{20pn} + \frac{2}{z}\partial_z\phi_{20pn} - \frac{n(n+1)}{z^2}\phi_{20pn} = -(2n+1)\mu_n. \tag{5.21}$$

The solution of Eq. (5.21) is then expressed as

$$\phi_{20pn} = z^{-(n+1)}\left(\int_{z_\infty}^{z} y^{n+2}\mu_n(y)dy + C_{5n}\right) - z^n\left(\int_{z_\infty}^{z} y^{-(n-1)}\mu_n(y)dy + C_{6n}\right). \tag{5.22}$$

By applying the boundary condition of $\nabla\phi_{20p} \rightarrow 0$ as $z = z_\infty$, the coefficients of C_{5n} and C_{6n} become zeros: i.e., $C_{5n} = 0$ and $C_{6n} = 0$. Then, the expansion coefficients ϕ_{20pn} is rewritten as

$$C_{5n} = 0,\ C_{6n} = 0. \tag{5.23}$$

b) Solution Procedure for Particular, Vector Acoustic Streaming Potential: Ψ_{20p}

The RHS of Eq. (5.3b) is expanded in terms of the Legendre polynomials and the associated Legendre polynomials as[23]

$$\begin{aligned}&\frac{\rho_0}{\eta}\left\langle \mathbf{v}_1\left(\vec{\nabla}\cdot\mathbf{v}_{1\psi}\right)+\mathbf{v}_{1\psi}\left(\vec{\nabla}\cdot\mathbf{v}_{1\phi}\right)+\left(\mathbf{v}_1\cdot\vec{\nabla}\right)\mathbf{v}_{1\psi}+\left(\mathbf{v}_{1\psi}\cdot\vec{\nabla}\right)\mathbf{v}_{1\phi}\right\rangle \\ &=\vec{e}_r\frac{1}{a^3}\sum_{n=0}^{\infty}(2n+1)\chi_{rn}(z)P_n(\cos\theta)-\vec{e}_\theta\frac{1}{a^3}\sum_{n=1}^{\infty}(2n+1)\chi_{\theta n}(z)P_n^1(\cos\theta)\end{aligned}, \quad (5.24a)$$

where

$$\begin{aligned}\chi_{rn}(z)=\frac{\rho_0 a^3}{2\eta}\int_0^{\pi}\vec{e}_r\cdot\Big\langle &\mathbf{v}_1\left(\vec{\nabla}\cdot\mathbf{v}_{1\psi}\right)+\mathbf{v}_{1\psi}\left(\vec{\nabla}\cdot\mathbf{v}_{1\phi}\right)\\ &+\left(\mathbf{v}_1\cdot\vec{\nabla}\right)\mathbf{v}_{1\psi}+\left(\mathbf{v}_{1\psi}\cdot\vec{\nabla}\right)\mathbf{v}_{1\phi}\Big\rangle P_n(\cos\theta)\sin\theta d\theta\end{aligned}, \quad (5.24b)$$

$$\begin{aligned}\chi_{\theta n}(z)=-\frac{\rho_0 a^3}{2\eta n(n+1)}\int_0^{\pi}\vec{e}_\theta\cdot\Big\langle &\mathbf{v}_1\left(\vec{\nabla}\cdot\mathbf{v}_{1\psi}\right)+\mathbf{v}_{1\psi}\left(\vec{\nabla}\cdot\mathbf{v}_{1\phi}\right)\\ &+\left(\mathbf{v}_1\cdot\vec{\nabla}\right)\mathbf{v}_{1\psi}+\left(\mathbf{v}_{1\psi}\cdot\vec{\nabla}\right)\mathbf{v}_{1\phi}\Big\rangle P_n^1(\cos\theta)\sin\theta d\theta\end{aligned}, \quad (5.24c)$$

The LHS of Eq. (5.24a) is a vector and thus can be decomposed into the divergence of an arbitrary scalar Q and the curl of an arbitrary vector $\mathbf{q}$ as

$$\frac{\rho_0}{\eta}\left\langle \mathbf{v}_1\left(\vec{\nabla}\cdot\mathbf{v}_{1\psi}\right)+\mathbf{v}_{1\psi}\left(\vec{\nabla}\cdot\mathbf{v}_{1\phi}\right)+\left(\mathbf{v}_1\cdot\vec{\nabla}\right)\mathbf{v}_{1\psi}+\left(\mathbf{v}_{1\psi}\cdot\vec{\nabla}\right)\mathbf{v}_{1\phi}\right\rangle=\nabla Q+\vec{\nabla}\times\mathbf{q}. \quad (5.25a)$$

where

$$Q=\frac{1}{a^2}\sum_{n=0}^{\infty}Q_n(z)P_n(\cos\theta), \quad (5.25b)$$

$$\mathbf{q}=\vec{e}_\phi\frac{1}{a^2}\sum_{n=0}^{\infty}q_n(z)P_n^1(\cos\theta). \quad (5.25c)$$

By considering Eqs. (5.24) and (5.25), the scalar Q and the vector $\mathbf{q}$ can be expressed in terms of $\chi_{rn}(z)$ and $\chi_{\theta n}(z)$ as

$$Q_n = z^{-(n+1)}\left[n\int_{z_\infty}^{z} y^{n+1}\left[\chi_{rn}(y)-(n+1)\chi_{\theta n}(y)\right]dy - C_{7n}\right], \\ +z^{n}\left[(n+1)\int_{z_\infty}^{z} y^{-n}\left[\chi_{rn}(y)+n\chi_{\theta n}(y)\right]dy - C_{8n}\right] \tag{5.26a}$$

$$q_n = -z^{-(n+1)}\left[\int_{z_\infty}^{z} y^{n+1}\left[\chi_{rn}(y)-(n+1)\chi_{\theta n}(y)\right]dy - \frac{C_{7n}}{n}\right]. \\ +z^{n}\left[\int_{z_\infty}^{z} y^{-n}\left[\chi_{rn}(y)+n\chi_{\theta n}(y)\right]dy - \frac{C_{8n}}{n+1}\right] \tag{5.26b}$$

The substitution of Eqs. (5.4c) and (5.25a) into Eq. (5.3b) gives

$$\nabla^2\nabla^2\boldsymbol{\Psi}_{20p} = \nabla^2\mathbf{q}\,, \tag{5.27a}$$

or

$$\nabla^2\boldsymbol{\Psi}_{20p} = \mathbf{q}\,. \tag{5.27b}$$

The function $\boldsymbol{\Psi}_{20p}(z)$ is then expanded in terms of the associated Legendre polynomials as

$$\boldsymbol{\Psi}_{20p} = \vec{e}_\phi \sum_{n=1}^{\infty} \psi_{20pn}(z) P_n^1(\cos\theta)\,. \tag{5.28}$$

By plugging Eq. (5.28) into Eq. (5.27b), the expansion coefficient $\psi_{20pn}(z)$ is expressed as

$$\partial_{zz}\psi_{20pn} + \frac{2}{z}\partial_z\psi_{20pn} - \frac{n(n+1)}{z^2}\psi_{20pn} = q_n(z)\,. \tag{5.29}$$

Eq. (5.29) is similar to Eq. (5.21) and its solution is then represented as

$$\psi_{20\,pn}(z) = -\frac{z^{-(n+1)}}{2(2n+3)}\left(\int_{z_\infty}^{z} y^{n+3}\left[\chi_{rn}(y)-(n+3)\chi_{\theta n}(y)\right]dy - C_{9n}\right)$$
$$+\frac{z^{-(n-1)}}{2(2n-1)}\left(\int_{z_\infty}^{z} y^{n+1}\left[\chi_{rn}(y)-(n+1)\chi_{\theta n}(y)\right]dy - \frac{C_{7n}}{n}\right)$$
$$-\frac{z^{n}}{2(2n-1)}\left(\int_{z_\infty}^{z} y^{-(n-2)}\left[\chi_{rn}(y)+(n-2)\chi_{\theta n}(y)\right]dy - C_{10n}\right) \quad . \qquad (5.30)$$
$$+\frac{z^{n+2}}{2(2n+3)}\left(\int_{z_\infty}^{z} y^{-n}\left[\chi_{rn}(y)+n\chi_{\theta n}(y)\right]dy - \frac{C_{8n}}{n+1}\right)$$

For the detailed derivation procedure for Eq. (5.30), see Appendix F. By considering the boundary condition of $\nabla\times\Psi_{20p} \to 0$ as $z = z_\infty$, the coefficients are determined as

$$C_{7n} = 0,\ C_{8n} = 0,\ C_{9n} = 0, \text{ and } C_{10n} = 0. \qquad (5.31)$$

5.1.4. Second-Order Time-Independent Boundary Conditions at Cell/Microparticle Surface

When the particle surface is oscillating in response to the incident wave, the fluid velocity at the oscillating surface can be expressed as[28]

$$\mathbf{v}\big|_{r=r(t)} = \mathbf{v}\big|_{r=a} + \mathbf{u}\cdot\left(\vec{\nabla}\mathbf{v}\right)\Big|_{r=a}, \qquad (5.32)$$

where **u** is the displacement of the particle surface. By using the perturbation method, the second-order time independent microparticle surface velocity at $r = r(t)$ is obtained as

$$\mathbf{v}_{20}\big|_{r=r(t)} = \mathbf{v}_{20}\big|_{r=a} + \left\langle\left[\mathbf{u}_1\cdot\left(\vec{\nabla}\mathbf{v}_1\right)\right]_{r=a}\right\rangle, \qquad (5.33a)$$

or

$$\mathbf{v}_{20}\big|_{r=a} = \mathbf{v}_{20}\big|_{r=r(t)} - \left\langle \left[\mathbf{u}_1 \cdot \left(\vec{\nabla} \mathbf{v}_1 \right) \right]_{r=a} \right\rangle, \tag{5.33b}$$

where

$$\begin{aligned} \left\langle \left[\mathbf{u}_1 \cdot \left(\vec{\nabla} \mathbf{v}_1 \right) \right]_{r=a} \right\rangle = \vec{e}_r \left\langle \left(u_r \frac{\partial v_{1r}}{\partial r} + \frac{u_\theta}{r} \frac{\partial v_{1r}}{\partial \theta} - \frac{u_\theta v_{1\theta}}{r} \right)_{r=a} \right\rangle \\ + \vec{e}_\theta \left\langle \left(u_r \frac{\partial v_{1\theta}}{\partial r} + \frac{u_\theta}{r} \frac{\partial v_{1\theta}}{\partial \theta} + \frac{u_\theta v_{1r}}{r} \right)_{r=a} \right\rangle \end{aligned}. \tag{5.33c}$$

The LHS of Eq. (5.33c) is expanded in terms of the Legendre polynomials and the associated Legendre polynomials as

$$\left\langle \left[\mathbf{u}_1 \cdot \left(\vec{\nabla} \mathbf{v}_1 \right) \right]_{r=a} \right\rangle = \vec{e}_r \frac{1}{a} \sum_{n=0}^{\infty} (2n+1) \alpha_n P_n (\cos\theta) - \vec{e}_\theta \frac{1}{a} \sum_{n=1}^{\infty} (2n+1) \beta_n P_n^1 (\cos\theta), \tag{5.34a}$$

where

$$\alpha_n = \frac{a}{2} \int_0^\pi \left\langle \left(u_r \frac{\partial v_{1r}}{\partial r} + \frac{u_\theta}{r} \frac{\partial v_{1r}}{\partial \theta} - \frac{u_\theta v_{1\theta}}{r} \right)_{r=a} \right\rangle P_n (\cos\theta) \sin\theta d\theta, \tag{5.34b}$$

$$\beta_n = \frac{a}{2n(n+1)} \int_0^\pi - \left\langle \left(u_r \frac{\partial v_{1\theta}}{\partial r} + \frac{u_\theta}{r} \frac{\partial v_{1\theta}}{\partial \theta} + \frac{u_\theta v_{1r}}{r} \right)_{r=a} \right\rangle P_n^1 (\cos\theta) \sin\theta d\theta. \tag{5.34c}$$

At the oscillating cell/microparticle surface $r = r(t)$, the acoustic streaming velocity is assumed to be zero, that is $\mathbf{v}_{20}|_{r=r(t)} = \mathbf{0}$. In addition, the acoustic streaming velocity at $r = a$ can be expressed in terms of the scalar potential ϕ_{20p} and the vector potential $\mathbf{\Psi}_{20h} + \mathbf{\Psi}_{20p}$. Therefore, considering Eq. (5.33b), a new equation is obtained as

$$\left(\nabla \phi_{20p} \right)_{r=a} + \left[\vec{\nabla} \times \left(\mathbf{\Psi}_{20h} + \mathbf{\Psi}_{20p} \right) \right]_{r=a} = - \left\langle \mathbf{u} \left(\vec{\nabla} \mathbf{v}_1 \right) \Big|_{r=a} \right\rangle. \tag{5.35}$$

The substitution of Eq. (5.34) into Eq. (5.35) results in

$$\partial_r \phi_{20pn}\Big|_{r=a} - \frac{n(n+1)}{a}\psi_{20pn}\Big|_{r=a} - \frac{n(n+1)}{a}\left(C_{1n}+C_{2n}\right) = -\frac{2n+1}{a}\alpha_n , \qquad (5.36a)$$

$$\begin{aligned} &\frac{1}{a}\phi_{20pn}\Big|_{r=a} - \partial_r \psi_{20pn}\Big|_{r=a} - \frac{1}{a}\psi_{20pn}\Big|_{r=a} \\ &-\frac{1}{a}\left[-(n-1)C_{1n} - (n+1)C_{2n}\right] - \frac{1}{a}\left(C_{1n}+C_{2n}\right) = \frac{2n+1}{a}\beta_n \end{aligned} , \qquad (5.36b)$$

where the expressions and derivative of ϕ_{20p}, $\mathbf{\Psi}_{20h}$, and $\mathbf{\Psi}_{20p}$ can be obtained in Eqs. (5.15)-(5.16), (5.20), (5.23), (5.28), (5.30), and (5.31). By solving Eq. (5.36), the coefficients C_{1n} and C_{2n} are determined as

$$\begin{aligned} C_{1n} = &\frac{n}{2}\left[\frac{2n+1}{n(n+1)}\alpha_n + \frac{a}{n(n+1)}\partial_r \phi_{20pn}\Big|_{r=a} - \psi_{20pn}\Big|_{r=a}\right] \\ &-\frac{1}{2}\left[(2n+1)\beta_n - \phi_{20pn}\Big|_{r=a} + a\partial_r \psi_{20pn}\Big|_{r=a} + \psi_{20pn}\Big|_{r=a}\right] \end{aligned} , \qquad (5.37a)$$

$$\begin{aligned} C_{2n} = &-\frac{n-2}{2}\left[\frac{2n+1}{n(n+1)}\alpha_n + \frac{a}{n(n+1)}\partial_r \phi_{20pn}\Big|_{r=a} - \psi_{20pn}\Big|_{r=a}\right] \\ &+\frac{1}{2}\left[(2n+1)\beta_n - \phi_{20pn}\Big|_{r=a} + a\partial_r \psi_{20pn}\Big|_{r=a} + \psi_{20pn}\Big|_{r=a}\right] \end{aligned} . \qquad (5.37b)$$

5.2. Simulation Results and Discussion

The proposed method can be used to calculate the acoustic streaming in the outer boundary layer analytically while the streaming in the inner boundary layer can be obtained by solving the integrals for the short integral range. For the simulated acoustic streaming results, two kinds of spherical particles are used in this chapter. One is a polystyrene (PS) bead and the other is a liquid droplet, and the radii of both the particles are a = 10 μm. For the PS bead, its Young's modulus and Poisson's ratio are set to E = 3.4 GPa and ν = 0.35, respectively.[85] For the liquid droplet, its density and surface

tension are ρ_0 = 1100 kg/m^3 and T_0 = 0.2 N/m, respectively.[43, 50]

The acoustic streaming around the PS bead for an incident plane wave of ka = 0.01 is calculated and then the computational times of both the proposed method and the Doinikov's method are compared. Since the proposed method is advantageous to the calculation of the acoustic streaming around particles of non-compact size (i.e., $ka \geq 1$), the acoustic streaming for the PS bead and the liquid droplet are then compared for their computational accuracies under the excitation condition of ka = 1.

5.2.1. Acoustic Streaming Around Compact Polystyrene Bead of ka = 0.01

Figure 5.2 shows the acoustic streaming in the vicinity on the surface of the PS bead in water when a plane standing ultrasonic wave with amplitude of 10^5 Pa at the excitation frequency of ka = 0.01 is incident to the PS bead in the vertical direction (i.e., θ = 90°). In Fig. 5.2, the four vortexes are observed and are symmetric with respect to the axes of x = 0 and y = 0. The maximum steaming velocity occurs at the surface of the PS bead, which is due to the large spatial gradient of the shear fluid medium velocity. The velocity nodal line is formed approximately at $r = a + \delta_v$ and the velocity directions are opposite at both the sides of the nodal line. In the far field away from the surface, the velocity is decreased significantly.

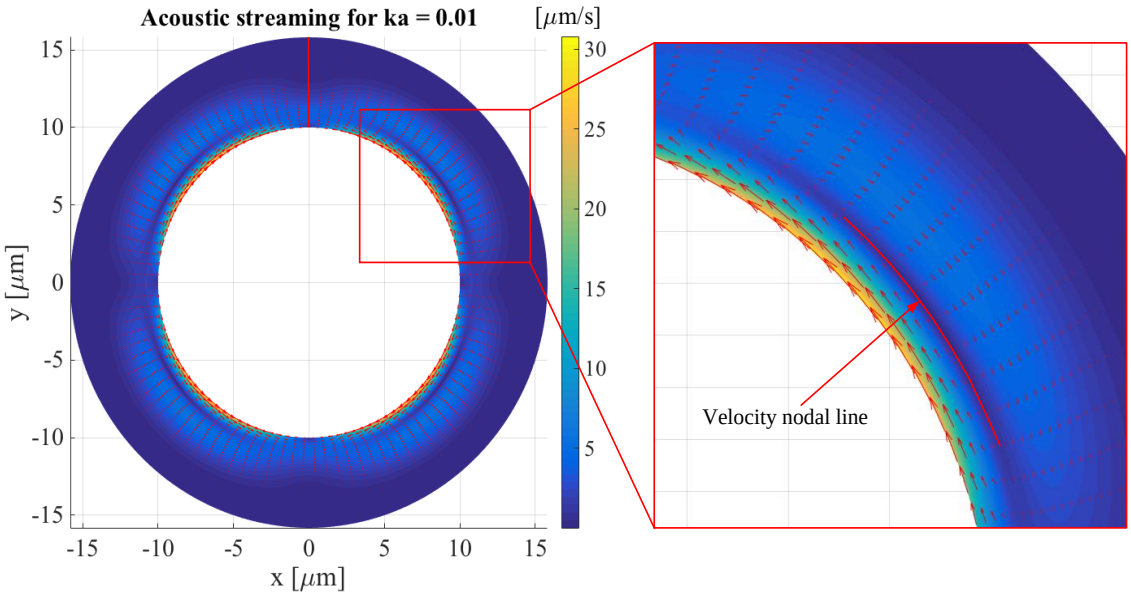

Fig. 5.2: Acoustic streaming around PS bead in water under ultrasonic standing plane wave excitation at frequency of ka = 0.01 in incident angle of 90°. The acoustic streaming is symmetric with respect to x = 0 and y = 0 and one vortex is shown in the right figure.[102]

Under the same condition of ka = 0.01, the computational times of both the Doinikov's method and the proposed method are compared in Table 1. These two methods were implemented in MathWork® Matlab 2014b for Mac. The computation was performed in an Apple® iMac Late 2013 equipped with 32 GB RAM (1600MHz) and one Intel Core i7 processor with the clock frequency of 3.5 GHz. The last column in Table 1 shows the spatially-averaged percentage difference between the streaming velocity distributions calculated by using the two methods for the range of [a, 4a]. Here, the percentage difference is defined as

$$E_r = \frac{\sqrt{\left(v_{20x} - v_{20x\_ref}\right)^2 + \left(v_{20y} - v_{20y\_ref}\right)^2}}{\mathrm{Max}\left(\sqrt{\left(v_{20x\_ref}\right)^2 + \left(v_{20x\_ref}\right)^2}\right)}, \tag{5.38}$$

where the acoustic streaming velocity calculated using the proposed method is used as a reference.

Table 5.1: Comparison of computational time for PS bead for $ka = 0.01$[102]

Doinikov's method		Proposed method		Spatially-Averaged Percentage Difference of Acoustic Streaming
Integral range	Computational time [s]	Integral range	Computational time [s]	
[a 100a]	94.9	[a a+10δ_v]	3.93	2.95 %
[a 150a]	102.5			2.94 %
[a 200a]	114.6			2.94 %
[a 250a]	127.8			2.94 %
[a 300a]	144.8			2.94 %
[a 350a]	174.9			2.94 %

As shown in Table 1, the Doinikov's method results in smaller difference when the integral range is larger than 150a although its computational time is getting much longer. Obviously, the proposed method can produce the more accurate results in much shorter computational time than the Doinikov's method. Even for the integral range of [a 100a], the computational time of the Doinikov's method is approximately 24.2 times longer than the proposed method. Therefore, the proposed method can be used to reduce the computational time significantly. However, the results in Table 1 are based on the spatially-averaged computation and do not give detailed information about the streaming velocity components at specific locations. Along the direction of $x = 0$ and $y > a$ (i.e., the direction along the red line in Fig. 5.2), the streaming velocities for different integral

ranges using Doinikov's method and the proposed methods are compared. Here, the streaming velocity in the θ-direction is supposed to be zero due to the symmetry of the streaming and thus only the streaming velocity in the r-direction v_{20r} is considered. In contrast to the results in Table 1, Fig. 5.3 shows that v_{20r} converges to a constant value until the integral range goes from a to $350a$ for the method of Doinikov, and this converged result using Doinikov's method is exactly in line with the one using the proposed method, validating the proposed method. For a converged result, the computational time for Doinikov's method is approximately 44.5 times longer than the proposed method. Besides, it is of interest to observe that the streaming velocity decreases significantly for $r > 1.5a$.

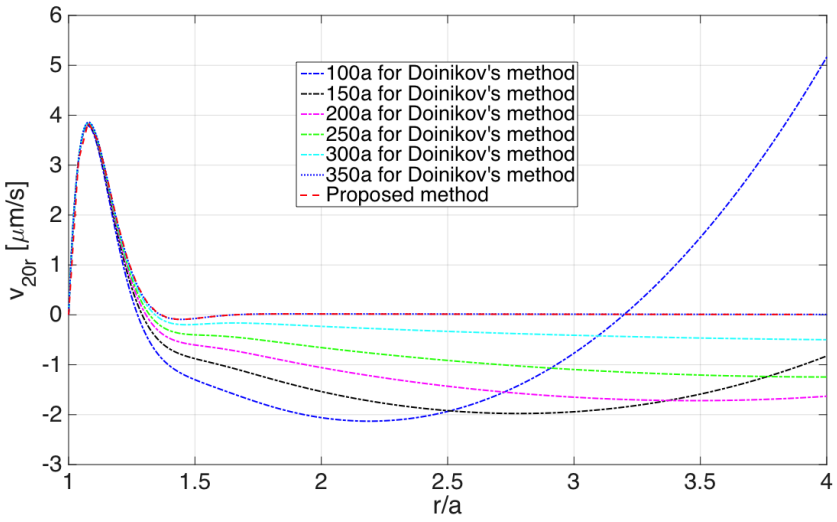

Fig. 5.3: Comparison of acoustic streaming velocity in r-direction along red line in Fig. 5.2 for different integral range using Doinikov's method and proposed method, respectively. Here, the simulation setup is the same as that in Fig. 5.2, and the acoustic streaming is shown for range of [a, $4a$].

5.2.2. Acoustic Streaming Around Polystyrene Bead of ka = 1

For an incident wave of $ka \geq 1$, the viscous boundary layer thickness δ_v is relatively thin compared with microparticle radius a. In this simulation, the incident wavenumber is set to $ka = 1$. Then, the viscous boundary layer is $\delta_v = 0.12$ μm for a particle of 10 μm in radius. In this extremely thin layer, it is difficult to clearly observe the inner streaming either in a simulation or in an experiment. Thus, the outer streaming is only of interest. In this paper, the outer streaming for $r > a + 4\delta_v$ is presented. Figure 5.4(a) shows the outer acoustic streaming generated around the spherical PS bead under an ultrasonic plane wave excitation of $ka = 1$. In Fig. 5.4(a), twelve vortexes are observed and these vortexes are symmetric with respect to the axes of $x = 0$ and $y = 0$. For the outer streaming, the maximum speed occurs in the vicinity of the top and bottom surface of the particle, different from the case of $ka = 0.001$ in Fig. 2. Figure 5.4(b) shows the percentage difference between the acoustic streaming results obtained by using the Doinikov's method and the proposed method (see Eq. (5.38)). In Fig. 5.4(b), the maximum percentage difference is approximately 5.5%. In particular, the difference is increased along the red line shown in Fig. 5.4(b). Along this red line, the total streaming velocities ($\mathbf{v}_{20} = \mathbf{v}_{20h} + \mathbf{v}_{20p}$) in the r-direction are compared in Fig. 5.4(c). Here, the streaming velocity in the viscous boundary layer is also included. For $r < 1.5a$, the total acoustic streaming velocity is much higher than that in the rest region. The velocities calculated by using both the methods are also close to each other in this region. As the r-direction distance increases, the difference between the two methods increases slightly. For the PS bead, these results agree well with each other, indicating that the

proposed method is valid.

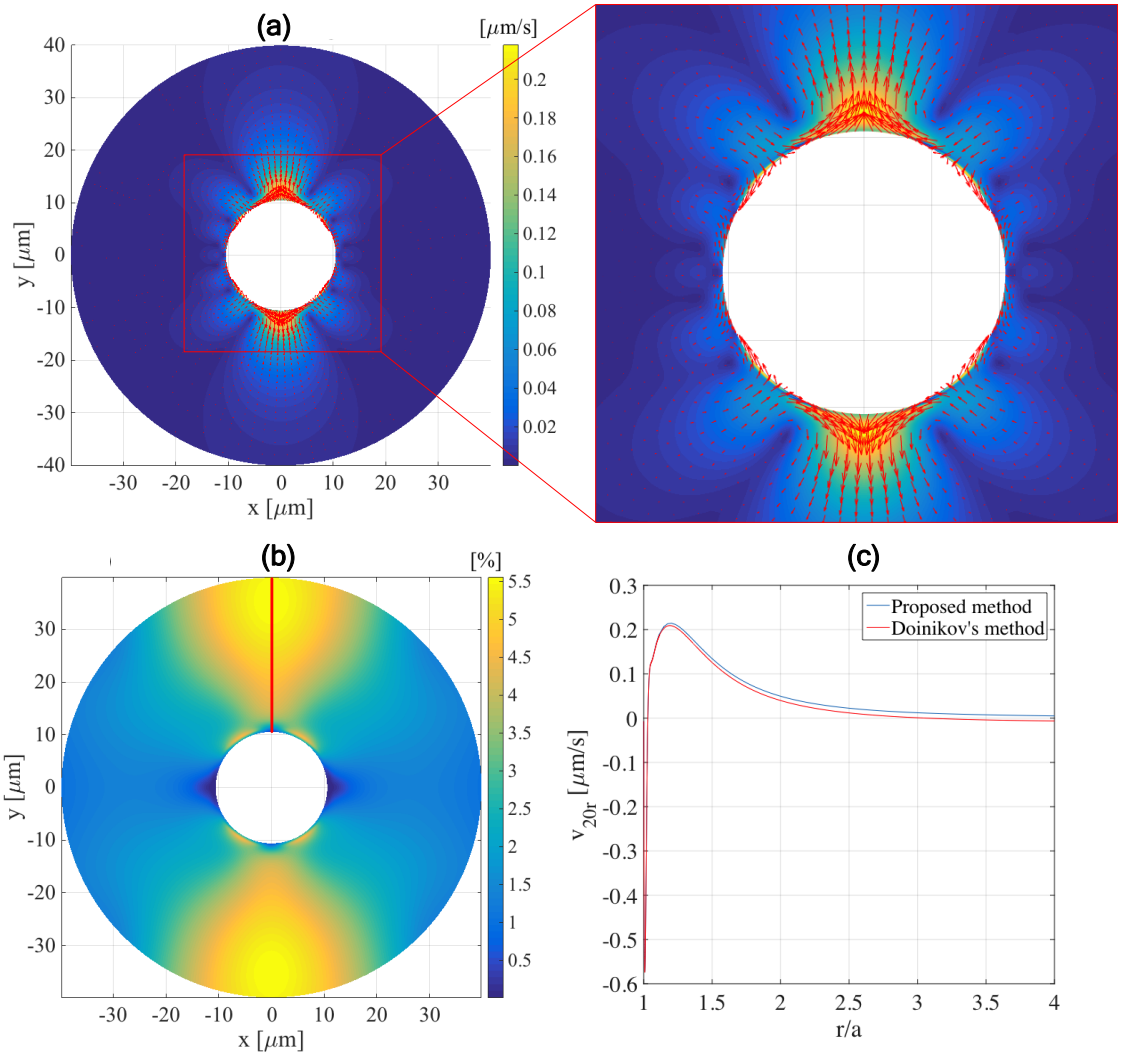

Fig. 5.4: Outer acoustic streaming around PS bead in water under ultrasonic plane wave excitation at frequency of ka = 1 in incident angle of 90°. (a) Acoustic streaming calculated by using proposed method for range of [a+4δ_v, 4a]. (b) Percentage difference of streaming velocities (referenced with the streaming velocity distribution calculated by using proposed method). (c) Streaming velocities in r-direction along red line in Fig. 5.4(b).[102]

5.2.3. Acoustic Streaming Around Liquid Droplet of ka = 1

By using the same incident wave of ka = 1, the acoustic streaming around the liquid droplet is studied. In Fig. 5.5(a), it seems that there are four vortexes but they are not observed clearly, in contrary to the case of the PS bead in Fig. 5.4(a). It is interesting that the streaming velocity of the liquid droplet is much lower than that of the PS bead: i.e., in Figs. 5.4(a) and 5.5(a), the maximum acoustic streaming speeds of the PS bead and the liquid droplet are 0.22 μm/s and 0.019 μm/s, respectively. Figure 5.5(b) shows the percentage difference of the streaming velocity distributions calculated by using both the two methods. In contrast to the results for the PS bead in Fig. 5.4(b), there is the large percentage difference in the calculated streaming velocities with the maximum difference of 120% at $r = 4a$, along the red line in Fig. 5.5(b), as shown in Fig. 5.5(c). In the vicinity of the droplet surface at $r < 1.1a$, the two acoustic steaming results are in line with each other, providing the validation of the proposed method. For $r > 1.1a$, the solution of the Doinikov's method starts to diverge, while the acoustic streaming velocity of the proposed method converges to zero.

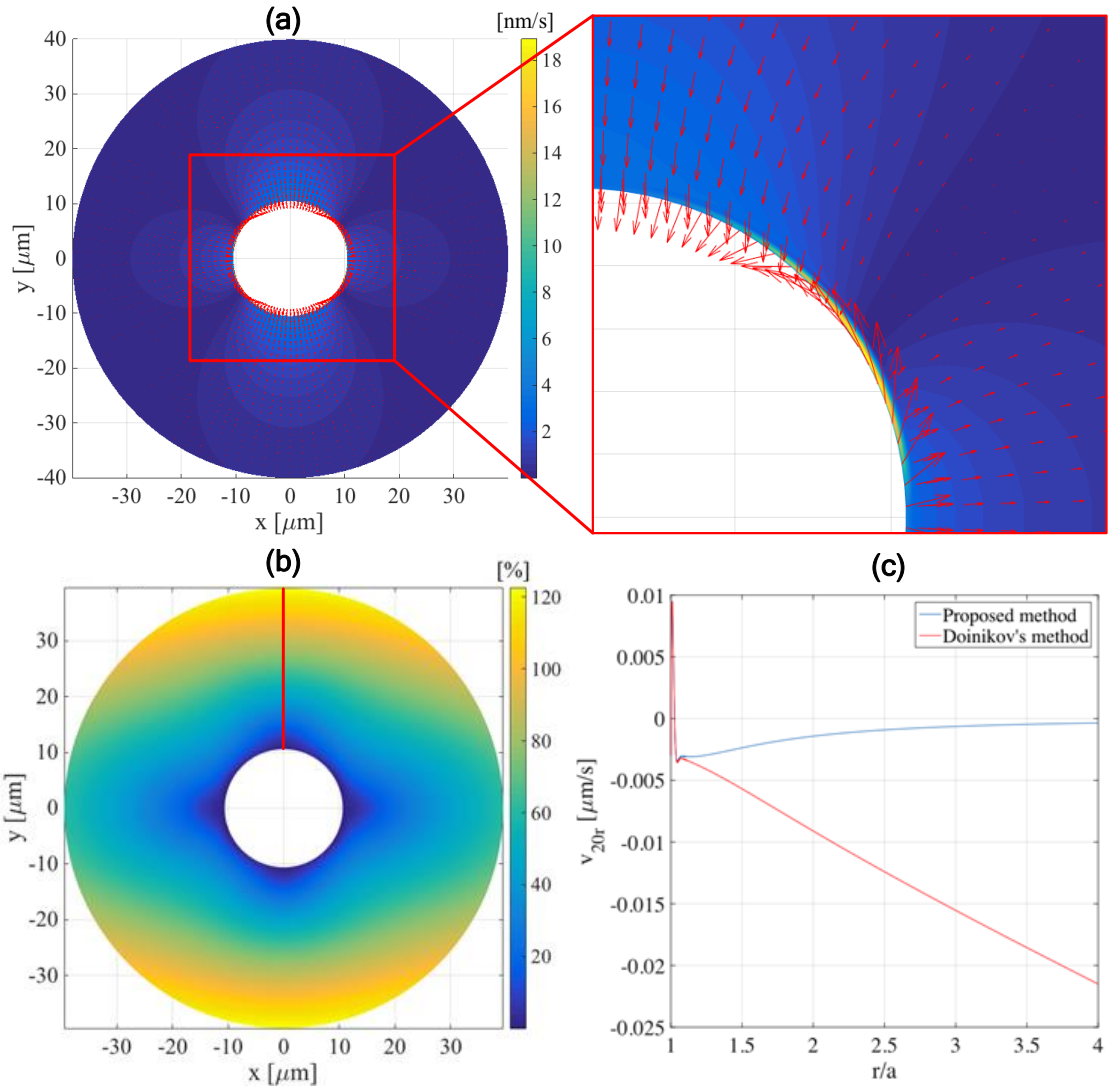

Fig. 5.5: Acoustic streaming around liquid droplet in water under ultrasonic plane wave excitation at frequency of ka = 1 in incident angle of 90°. (a) Acoustic streaming calculated by using proposed method for range of [a+4δ_v, 4a]. (b) Percentage difference of acoustic streaming velocities (referenced with the streaming velocity distribution calculated by using proposed method). (c) Streaming velocities in r-direction along red line in Fig. 5.5(b).[102]

5.3. Acoustic Streaming as Function of Excitation Frequency

The acoustic streaming induced by PS beads and cells is studied under the

propagating wave of amplitude 10^5 Pa. The parameters of the PS bead and cell are the same as those in Sec. 4.4.2 and 4.4.4. The maximum streaming velocity is investigated as a function of the excitation frequency.

Figure 5.6 shows the maximum streaming velocity for a PS bead, and the identified resonant frequencies are ka = 1.417 and 2.079 where peak streaming velocity magnitudes are observed, agreeing with the values 1.418 and 2.085 in Sec. 4.4.2. For those excitation frequency ranges, the magnitude order of the viscous boundary layer thickness is 0.1 μm, where the maximum streaming velocity occurs. This thickness is very small compared with the particle radius a = 10 μm, and thus here only the streaming for the range of [a+4δ_v, 4a] is shown for a clear view of the streaming in Fig. 5.6(b)-(g). It is observed that at the ka = 1.417 and 2.079, the maximum velocities for the range of [a+4δ_v, 4a] are 209.9 μm/s and 142.0 μm/s, respectively. Here, away from the resonant frequency ka = 1.418, two frequencies 1.34 (5.5%) and 1.51 (6.5%) are investigated in Fig. 5.6(b)-(d), and the maximum streaming velocities are 81.0 μm/s and 42.9 μm/s, respectively. As for the resonant frequency ka = 2.079, two frequencies ka = 1.99 (4.3% off) and 2.16 (3.9% off) are calculated with the maximum streaming velocities 53.8 μm/s and 39.5 μm/s shown in Fig. 5.6(e)-(g). Besides, the streaming patterns at the resonant frequencies are also different from that at non-resonant frequencies.

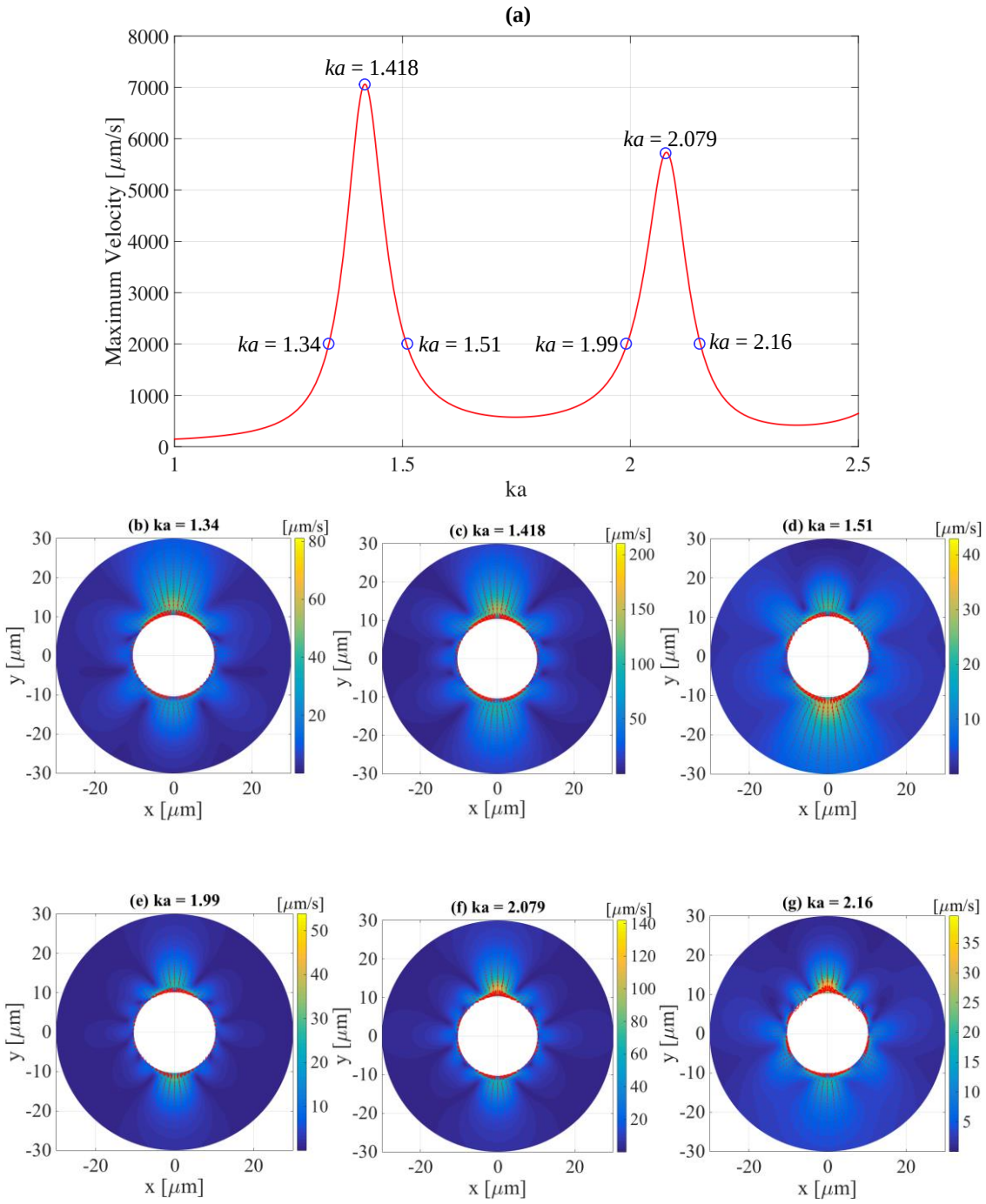

Fig. 5.6: Streaming velocity as function of *ka* for PS bead. The damping coefficient is set to be 0.001. (a) Maximum acoustic streaming velocity as function of *ka*. (b)-(g) Streaming velocity distribution for range of [a+4δ_v, 4a] around resonant frequencies.

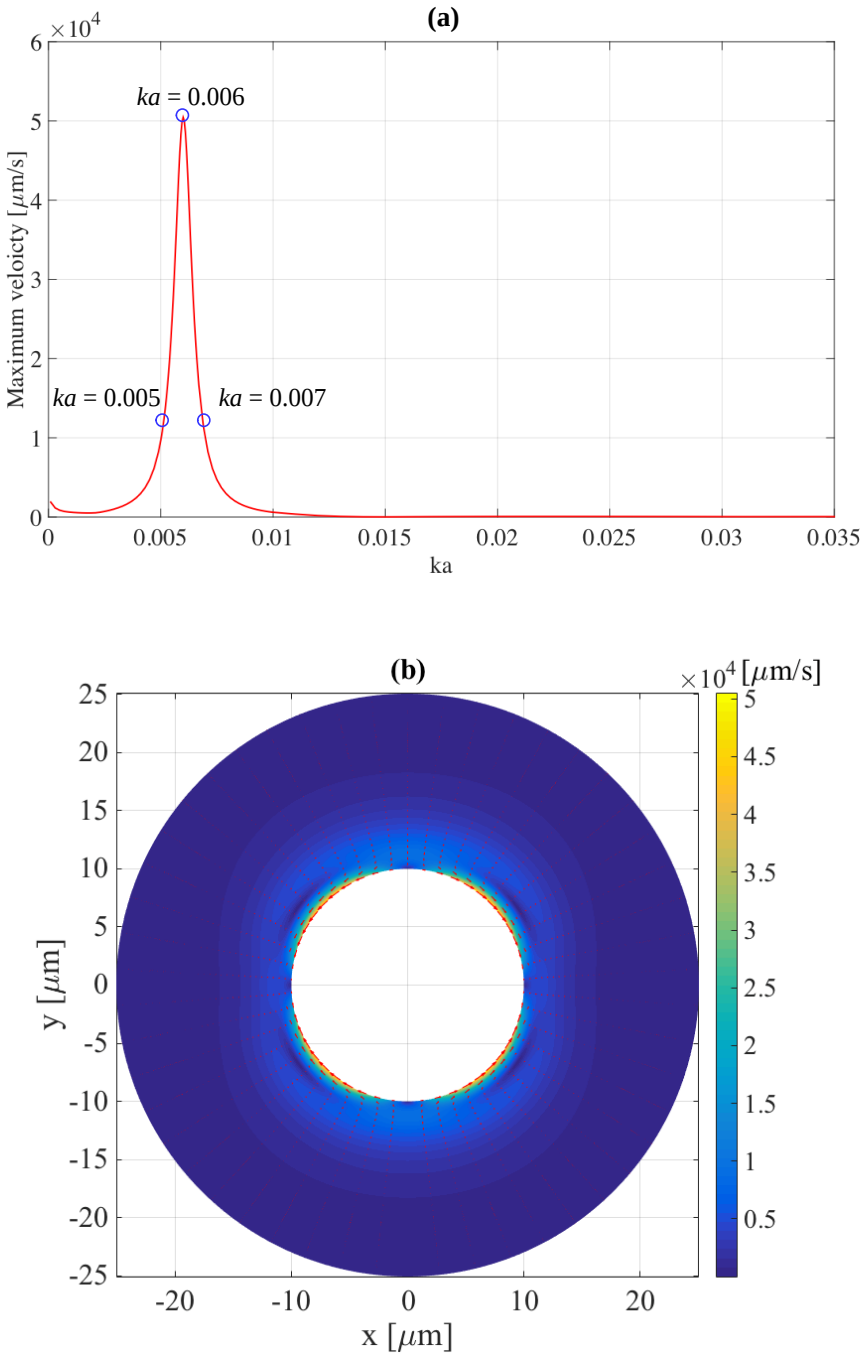

Fig. 5.7: Streaming velocity for cell model with K_A = 1.45 N/m and T_0 = 0.2 N/m. (a) Maximum streaming velocity as function of *ka*. (b) Acoustic streaming velocity distribution for *ka* = 0.006 for range of [*a*, 2*a*].

In Sec. 4.4.4, the complex fluid model is used to describe a cell and the excitation range is $0 < ka < 0.035$. In this range, the viscous boundary layer thickness is in the magnitude order of 1.5 μm, comparable with the particle radius. Therefore, in the thickness range of [a 2a], the streaming velocity can be observed clearly and shown in Fig. 5.7.

In Fig. 5.7(a), the resonant frequency $ka = 0.006$ is observed, the same as the values identified using the scattered pressure. Besides, it is found that the streaming patterns for the frequency close to $ka = 0.006$ are almost the same except different amplitudes. For example, the maximum streaming velocities for $ka = 0.005$, 0.006 and 0.007 are 9659.3 μm/s, 50431.5 μm and 9668.9 μm/s, respectively. And thus, the velocity magnitude can be an indicator of the resonant response of a cell.

5.4. Simulation of Streaming Particle Around Cell in Propagating Wave

In the simulation, small particles, named as streaming particles, are scattered around a cell in a propagating wave. The cell's parameters are the same as those in Sec. 5.3. The excitation frequency is selected as the resonant frequency of this cell $ka = 0.006$. The pressure amplitude of the wave is set to be 10^4 Pa. The radius of the streaming particles is 1 μm. Since the excitation is axisymmetric, only the right half of the results are shown in Fig. 5.8.

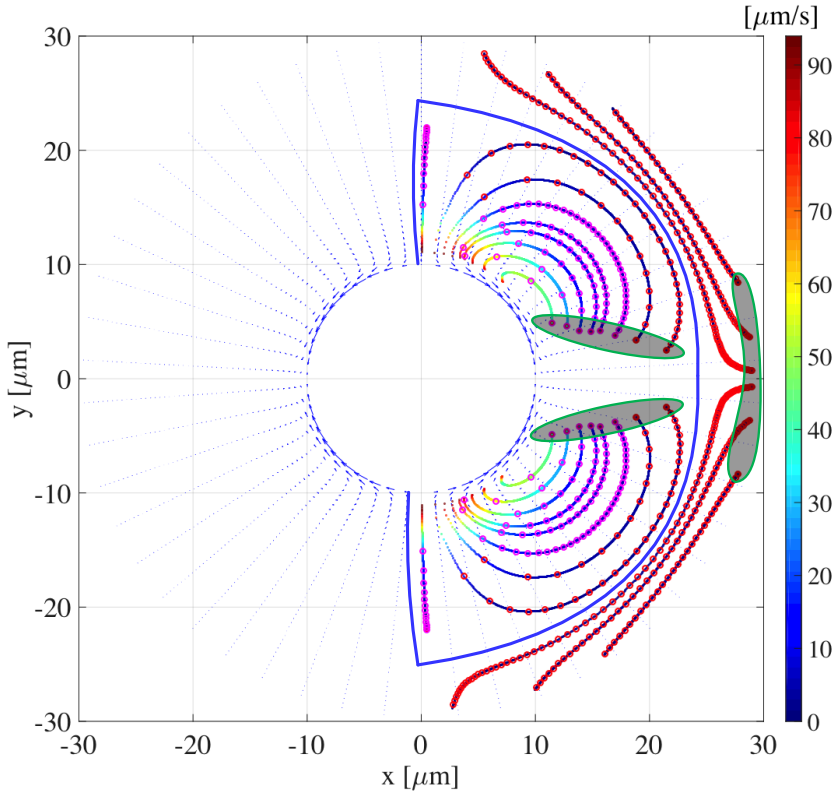

Fig. 5.8: Simulated trajectories of streaming particles around a cell in propagating wave. The radii of cell and streaming particles are 10 μm and 1 μm, respectively. The excitation frequency is ka = 0.006 and its pressure amplitude is 10^4 Pa. The time intervals for red and pink circles are 0.5 s and 0.1 s, respectively. Those points in blue areas represent initial positions.

In theory, if a streaming particle is very close to cell surface, it may be captured due to the drag force between the streaming particle and cell. Here, the same criterion is used. Figure 5.8 shows that once the streaming particle goes into a certain area around the cell, it will be captured due to the combination of the acoustophoretic force and acoustic streaming. The areas in the blue cures represent these capturing areas, and the boundary of those areas is about from the cell surface to twice cell radius. Outside those

capturing areas, the streaming particles move away from the cell at a very slow speed. If the particles are not trapped at the cell surface, they may be circulating along the acoustic streaming lines.

In this thesis, the research on the cell/microparticle is focused on a single cell/microparticle in free fields and the simulation is based on the assumption that the streaming particles does not affect the acoustic fields generated by the big cell/microparticle. In the acoustic fields, the inner layer thickness of the acoustic streaming is about acoustic boundary layer thickness $\delta = (2\eta/\rho_0/\omega)^{1/2}$. To observe the motion of the streaming particles clearly, the radii of those streaming particles are supposed to be comparable to or smaller than the inner layer thickness of the acoustic streaming. Based on the calculation, the affecting area of a cell/microparticle is usually in the range of [0 a] from the cell/microparticle's surface. If the streaming particle is significantly small compared with the big cell/microparticle, its affecting area is also very small compared with that of the big cell/microparticle and thus the effects of the small streaming particle can be ignored. For two big cells/microparticles with the same radius, the distance between them is at least five times their radius. By using a safety factor of two, the recommended distance would be ten times the radius.

5.5. Experiment on Streaming Particle Around Cancer Cell MCF-7

The experiment setup is shown in Fig. 5.9. The function generator (Agilent 33220A) provides the sinusoidal excitation to the power amplifier (ENI 2100L, 100 W). Then, the water in the cell dish (60 mm in diameter) is excited by the PZT transducer attached to the bottom of the cell dish. In the cell dish, the cancer cells MCF-7 and the

streaming poly(lactic-co-glycolic acid) (PLGA) particles are mixed. Here, the averaged radii of the PLGA particles are about 0.25 mm while the radii of MCF-7 are approximately 10 μm. Based on the simulation in Figs. 5.7 and 5.8, in the cell dish with ultrasonic excitation, the circulation of the PLGA particles around MCF-7 is supposed to be observed.

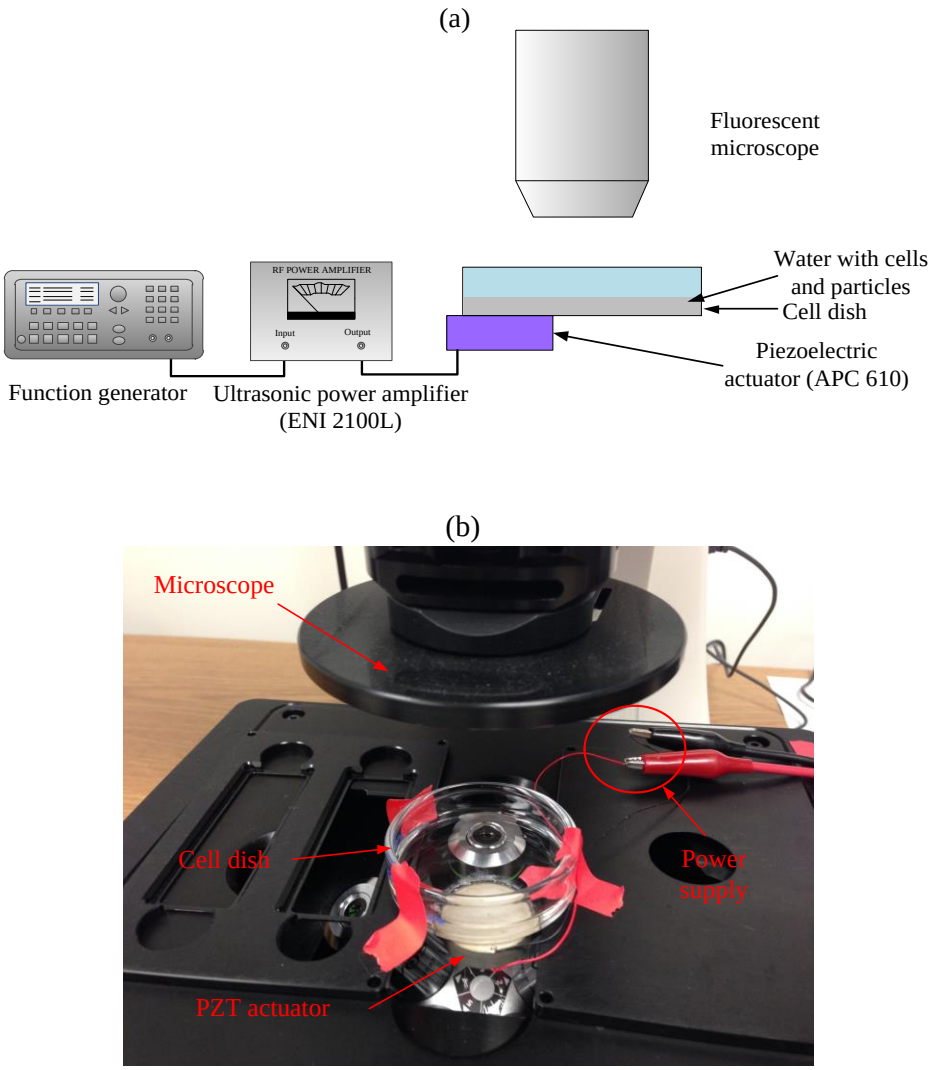

Fig. 5.9: Experimental setup of small particles around big cell/microparticle. (a) Schematic of experimental setup. (b) Photo of experimental setup.

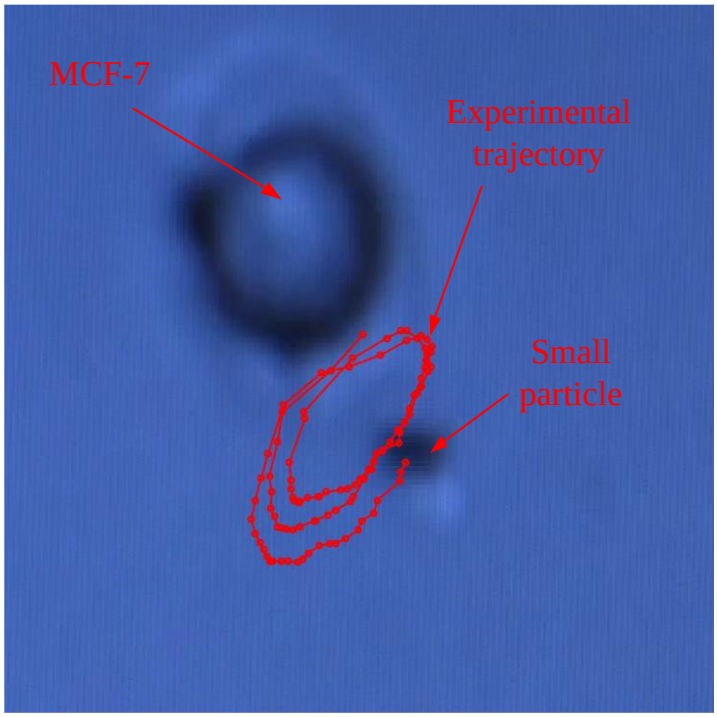

Fig. 5.10: Experimental trajectories of small particle around cancer cell.

In the experiment, the excitation frequency of the function generator is adjusted and the output voltage is kept on 150 mV. At the frequency of 85 kHz, the circulation of the PLGA particle around MCF-7 is observed. The inner layer thickness is about 1.9 μm that is much larger than the PLGA particles' radii. In Fig. 5.10, the experimental trajectory of the PLGA particle is extracted from the video clip. This trajectory shows a few circles of the PLGA particle, which agrees with what is expected. Furthermore, in Fig. 5.11, the images of the PLGA particle around MCF-7 are shown. Here, the time interval for those images is 0.5 s. In the simulation, the acoustic streaming velocity is observed to approach the maximum near the cell surface. Therefore, it is expected that the streaming particles may have the largest speed near the cell surface. In Fig. 5.11, it is obvious that the displacement of the PLGA particle is largest from t = 1.5 s to t = 3.0 s.

In those times, the PLGA approaches to the cell surface the most. Based on those experiment and simulation, the theory of the acoustic streaming around microparticles may be validated.

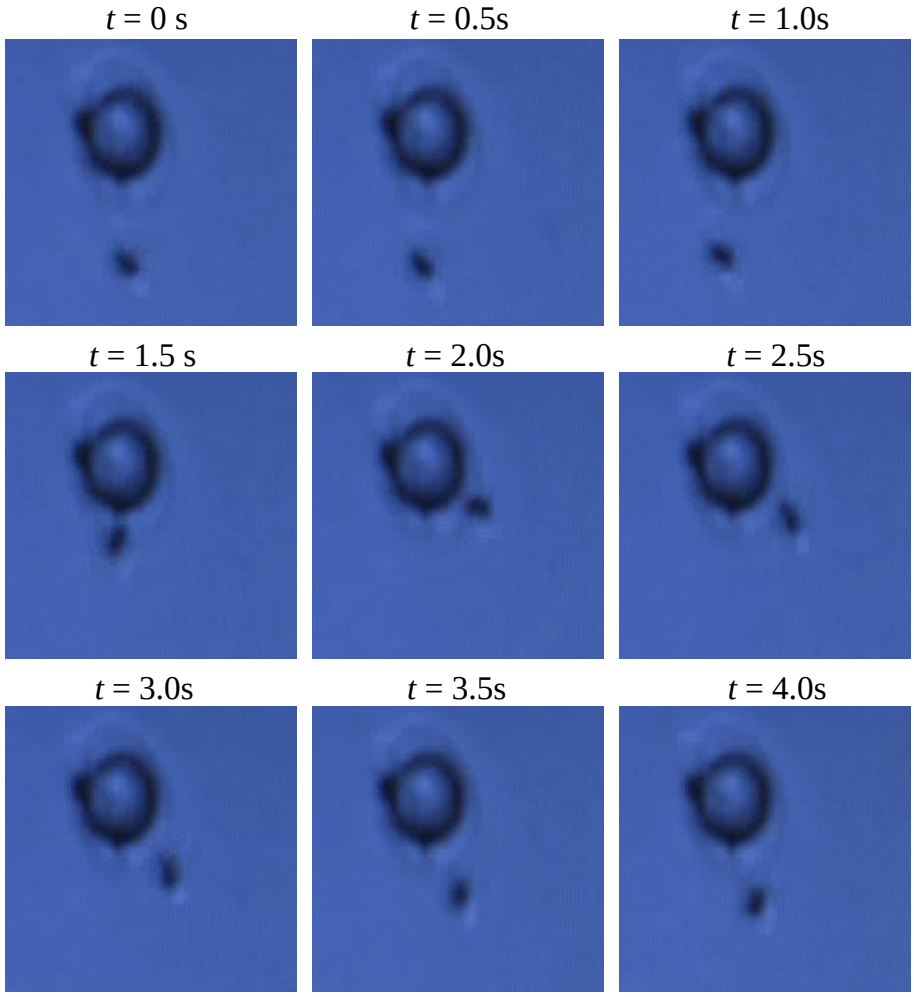

Fig. 5.11: Motion of streaming particle around MCF-7.

5.6. Estimation of Cell/Microparticle's Property

For a cancer cell line, its important parameters are the surface tension T_0, surface compression modulus K_A and shear modulus μ_A. As discussed in Sect. 4.4.4, $\mu_A = K_A/3$.

Therefore, T_0 and K_A are essential. By assuming either of them is zero, the other is estimated. For the cancer cell with radius a = 10 μm, its scaled resonant frequency is ka = 0.0036.

Here, with T_0 = 0 N/m, it is estimated that K_A = 0.546 N/m. In the same way, with K_A = 0 N/m, T_0 is estimated at 0.092 N/m. Since the relative data of MCF-7 is not found, those of RBC are compared. The surface tension of RBC is about 0.0255 N/m[43] and its surface compression modulus is calculated as 0.865 N/m.[98] Therefore, the magnitude of estimated values are in a reasonable magnitude order. Further, the maximum streaming velocity is plotted as a function of T_0 and K_A. Here, the incident wave is propagating with amplitude of 10^5 Pa. Fig. 5.12(a) shows that it is difficult to identify the peak velocity. At ka = 0.036, there is slight increase but not obvious. On the contrary, an sharp velocity peak is observed I Fig. 5.12(b). Moreover, both T_0 and K_A are put into the system together and it is found that the maximum streaming velocity plot in Fig. 5.12(c) is the same as Fig. 5.12(b). This phenomenon agrees with what is observed in Sect. 4.4. Therefore, it may be thought that the resonance of MCF-7 observed in the experiment may come from the parameter K_A.

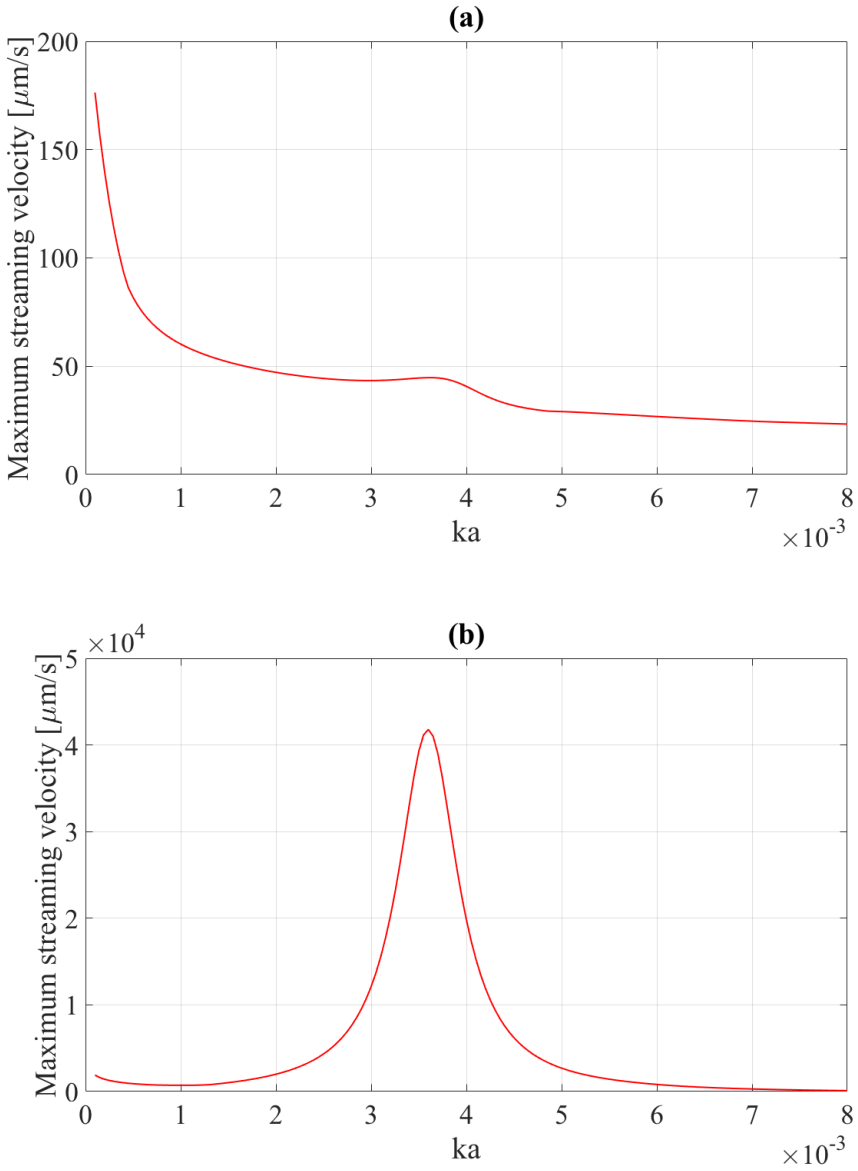

Fig. 5.12: Maximum streaming velocity for different T_0 and K_A of MCF-7. (a) maximum streaming velocity for T_0 = 0.092 N/m and K_A = 0 N/m. (b) maximum streaming velocity for T_0 = 0 N/m and K_A = 0.546 N/m. (c) maximum streaming velocity for T_0 = 0.092 N/m and K_A = 0.546 N/m.

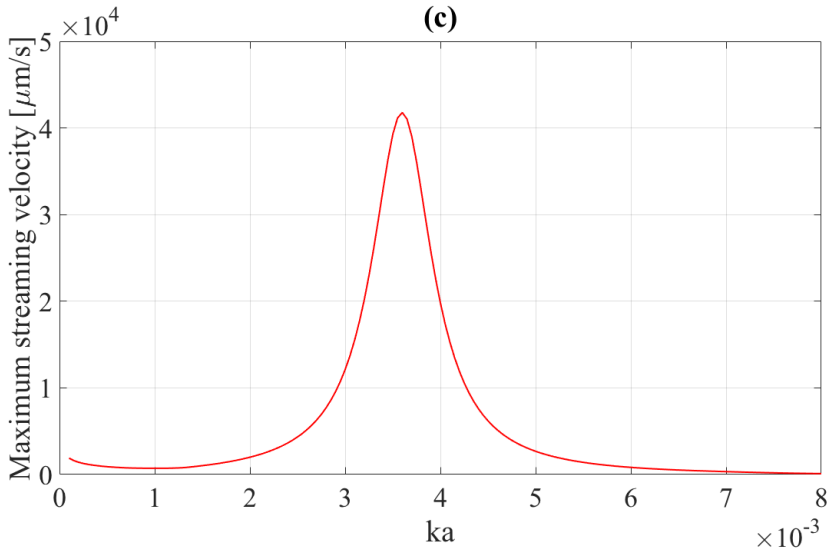

Fig. 5.12: Continued.

For a solid elastic particle, the important parameters are the Poisson's ratio and Young's modulus. The Poisson's ratio of PLGA material is 0.36[99,100], which is usually constant. However, its Young's modulus is reported in a large range of [0.6 4.4] GPa.[99,100] In this section, the Young's modulus's of PLGA is measured by observing the streaming motion in an ultrasonic excitation. In the experiment, the radius of the large PLGA particle is measured to be 42.4 μm and the resonant frequency corresponding to the stream motion is recorded to be 7.393 MHz. Therefore, the scaled resonant frequency is ka = 1.33. Based on the developed algorithm, the PLGA's Young's modulus is adjusted to have a peak velocity at ka = 1.33 and thus the Young's modulus is estimated to be 3.23 GPa, which falls in the report range of [0.6 4.4] GPa. In Fig. 5.13, the streaming velocity approach the maximum at ka = 1.33. Here, please note the structural damping is set to be 0.001.

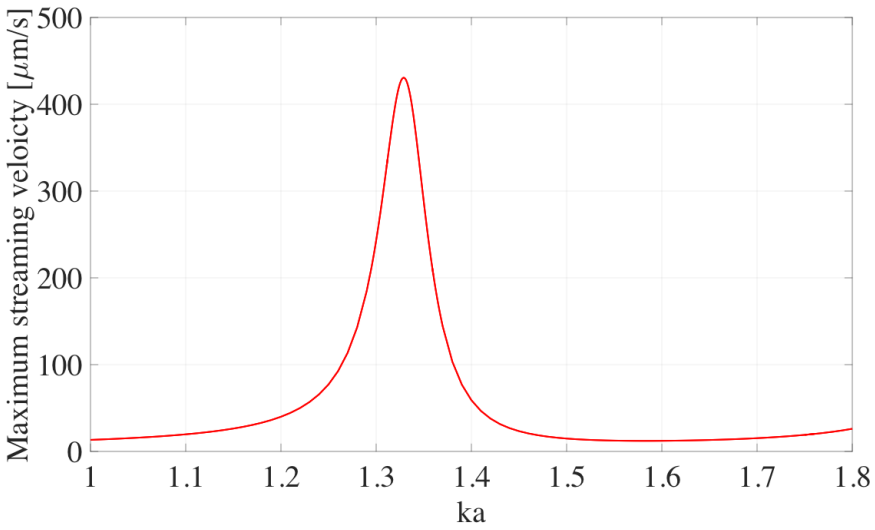

Fig. 5.13: Maximum streaming velocity for PLGA particle. The particle radius is 42.4 μm and the frequency at the peak velocity is ka = 1.33. The Young's modulus and Poisson's ratio are 3.23 GPa and 0.36, respectively.

5.7. Conclusion

In this chapter, the novel algorithm is proposed to compute the acoustic streaming around a cell/microparticle. By decomposing the acoustic streaming into the compressional and shear streaming components, the governing equations for each streaming component are solved independently. Then, the total acoustic streaming is obtained by combining the two resulting streaming components.

From the comparison of the computational times of both the Doinikov's method and the proposed method, it is shown that the computational time of the proposed method is approximately 1/44.5 of that of the Doinikov's method for the same acoustic streaming results. In addition, under the incident wave excitation of ka = 1, the acoustic streaming results, around the PS beads, obtained by using the Doinikov's method and the

proposed method are almost identical with the spatially-averaged maximum difference of 5.5%, indicating that the proposed method is valid. For the liquid droplet under the ultrasonic excitation of $ka = 1$, the acoustic streaming calculated by using the Doinikov's method is divergent at the farfield of the liquid droplet, while the proposed method results in the convergent streaming velocity. Therefore, it can be concluded that the proposed method can provide accurate acoustic streaming results in a relatively short computational time.

The response of the acoustic streaming to the excitation frequency shows the resonant frequencies agree with those identified by analyzing the scattered pressure in Chap. 4. At the resonant and non-resonant frequencies, the streaming velocities and patterns are distinguished and thus both can be used for the identification of cell/microparticle's properties.

In the experiment, the circulation of PLGA particles around cancer cells MCF-7 is observed, and the velocity of PLGA particles are much larger near the cell surface than those away from the cell surface. Those phenomena agree with the simulation and validate the theory of the acoustic streaming around cells/microparticles. Based on the developed algorithm, the parameters of cells/microparticles are estimated and compared with the reported results.

6. IDENTIFICATION OF CELL'S DENSITY AND COMPRESSIBILITY

Here, it is proposed that the density and compressibility of cells/microparticles are identified by using the acoustophoretic model presented in the previous chapter. The proposed property identification procedure consists of the following two steps. Firstly, the calibration of the excitation pressure inside the microchannel is conducted by analysing the trajectories of PS beads with known density and compressibility, and then the density and compressibility of cells are predicted by optimally fitting the experimental trajectories of the cells to the predicted ones.

The traditional models for predicting the acoustophoretic motion of cells/microparticles can be used to mainly analyze the particle's movement in the horizontal plane. Thus, using these models, it is difficult to identify the density and compressibility of the cells/microparticles simultaneously since the density is strongly correlated with the vertical motion. Based on the acoustophoretic model in Chap. 3, the particle's movement in both the horizontal and vertical directions can be predicted. Thus, the proposed procedure enables to identify the compressibility as well as the density. Depending on the vertical locations of the cells/microparticles, the viscous drag forces in the horizontal directions are affected by microchannel walls, which is referred to as the "wall effects" and has rarely been investigated before. In the proposed procedure, the wall effects are considered so that the mechanical properties can be identified accurately.

6.1. Theory and Method

The proposed procedure for identifying cell's density and compressibility is overviewed in Fig. 6.1. The recorded images of the motion of the cells and PS beads are processed by using an in-house image processing program to extract the trajectories of the PS beads and cells. Then, these trajectories are fitted into the trajectories predicted by using the acoustophoretic model developed in Chap. 3 for the calibration of the acoustic pressure excitation levels and the identification of the cell's density and compressibility. Each step in Fig. 6.1 will be discussed in detail in the following sections.

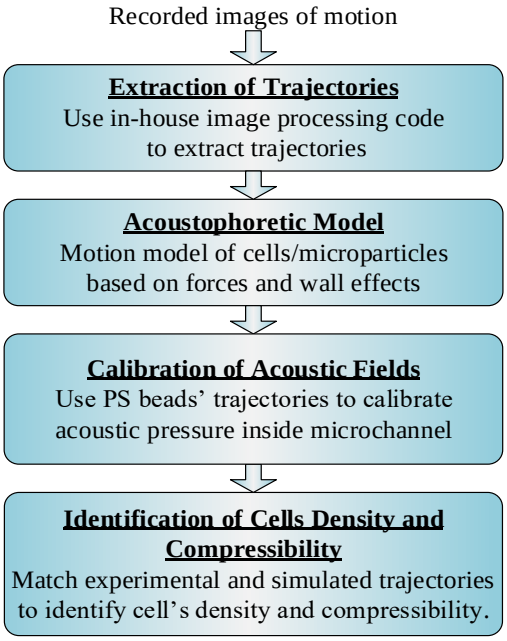

Fig. 6.1: Procedure for identifying cell's density and compressibility by using acoustophoretic model.

6.1.1. Extraction of Trajectories

The motions of the PS beads or cells are recorded as a serial of images using a microscope equipped with a video camera. Since the shapes of the PS beads are almost perfectly spherical, their recorded images can be processed easily, which allows the automatic extraction of the PS beads' trajectories. On the contrary, the shapes of cells are not perfectly spherical and the cells may not be focused well by the microscope, causing thus their recorded images blurry. In order to accurately extract the trajectories of the cells, a manual imaging processing program is also developed. In Fig. 6.2, the images of the PS beads and MCF-7 (breast cancer cell line) are shown. The images of the PS beads are always clear, e.g., at the record starting and middle times of $t = 0$ and $t = 2.6$ s as in Fig. 6.2, while the images of MCF-7 are unclear and their foci change with respect to the time since the cells are moving down due to their heavy density. Therefore, the automatic and manual extraction programs are developed to process the recorded image data of the PS beads and cells, respectively.

The trajectory errors caused by the cells' blurry images result occasionally in the inaccurate identification of the cells' density and compressibility. In reality, the quality of the extracted trajectories is dependent on the operation of the experiments.

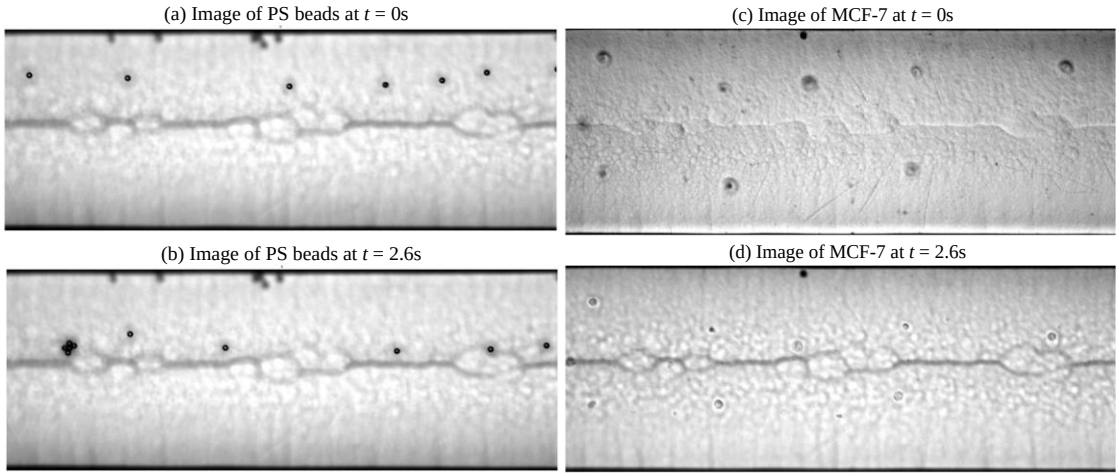

Fig. 6.2: Images of PS beads and MCF-7 (breast cancer cell line). (a) Image of PS beads at t = 0 s. (b) Image of PS beads at t = 2.6 s. (c) Image of MCF-7 at t = 0 s. (d) Image of MCF-7 at t = 2.6 s. The images of the PS beads are much better focused than those of MCF-7.

6.1.2. Viscous Drag Force Affected by Walls

In a static fluid medium, a moving particle generates a disturbance to the fluid. If the fluid domain is infinite, this disturbance decays out negligibly far away from the particle. However, if the fluid domain is finite, the disturbance is reflected by the boundaries of the finite fluid domain, then affecting the motion of the particle, referred to be as the "wall effects"[86] as illustrated in Fig. 6.3. In addition, the disturbance between two adjacent particles is significant if they are too close to each other, which is not considered in this chapter for the simplicity. Thus, the only particles isolated from other particles with a minimum dance of 10a are considered here where a is the radius of the particles. The minimum distance is determined by the theoretical calculation of the mutual disturbance between two particles moving in the same direction.

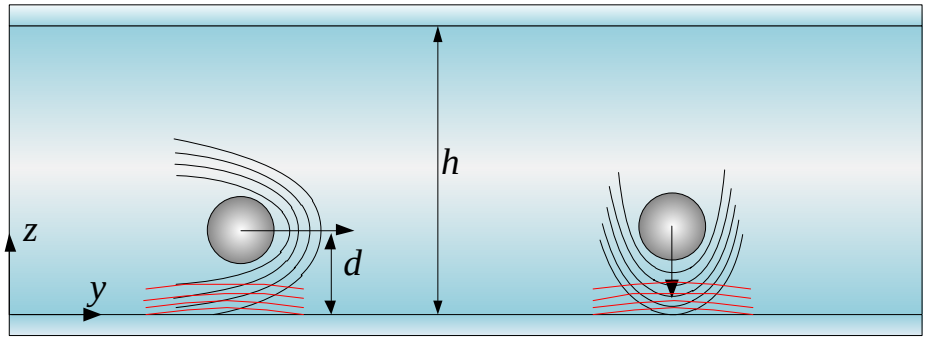

Fig. 6.3: Schematic of wall effects on motion of particle between two infinite parallel plates. When a particle is moving close to one plate, the disturbance to the motion of the particle is induced by the plate, which slows down the velocities of the particle in the *y*- and *z*-directions. Here, the black curves represent the disturbance induced by the moving particle and the red curves represent reflected disturbance by the wall.

The drag coefficients of a particle moving between two infinite parallel plates have been studied extensively for a long time. Figure 6.3 illustrates the disturbances when a particle is moving in the *y*- and *z*-directions. Here, C_y and C_z are used to represent the viscous drag coefficients for the particle moving in the *y*- and *z*-directions, respectively. According to Ref 87 and 88, the drag coefficients C_y and C_z are the functions of the particle radius a, the distance between the two plates h, and the particle's location d with respect to the plates as

$$C_y = f_{cy}(a,d,h), \tag{6.1a}$$

$$C_z = f_{cz}(a,d,h). \tag{6.1b}$$

Figure 6.4 shows the drag coefficients when the particle radius is a = 5.5 μm and the channel depth is h = 56 μm. Since the two plates are symmetric with respect to their center line, it is reasonable to display the viscous drag coefficients only for the half

channel. For the infinite fluid domain, the drag coefficients C_y and C_z are supposed to be 1. Due to the wall effects, the viscous drag coefficients C_y and C_z become much larger than 1. For example, at $d = h/2 = 28$ μm (i.e., $d/a = 5.1$), the viscous drag coefficients C_y and C_z are 1.233 and 1.286, respectively. The drag coefficients are exponentially decreasing as the distance increases. When the ratio of the particle location d to the radius a is large than 3, the drag coefficients do not vary much, and then the drag coefficients increase significantly as the particle location d decreases.

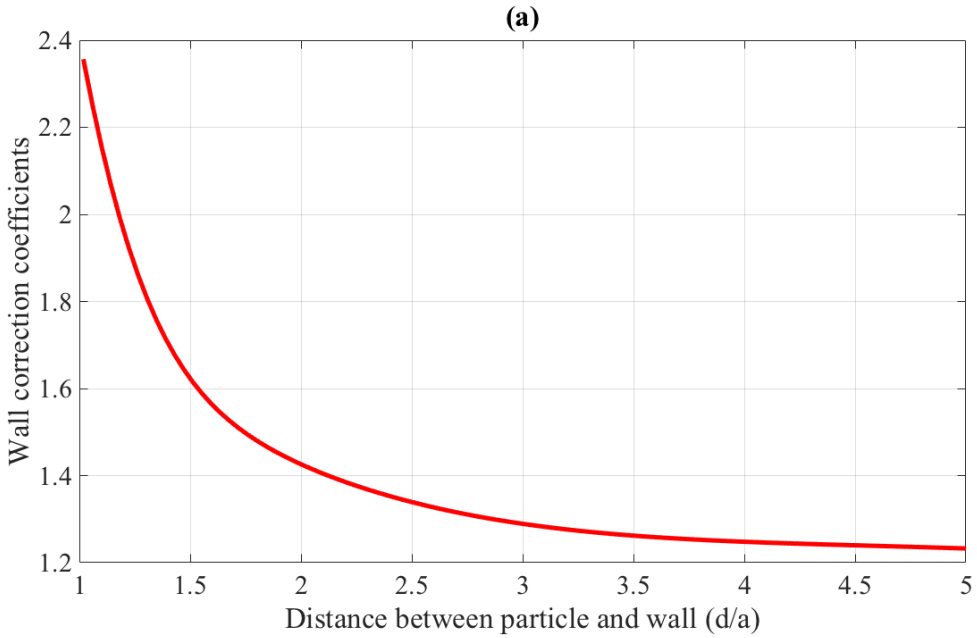

Fig. 6.4: Viscous drag force coefficients C_y and C_z as function of particle location d between two parallel plates. (a) Viscous drag force coefficients C_y. (b) Viscous drag force coefficients C_z. The distance between the two parallel plates is $h = 56$ μm and the particle radius is $a = 5.5$ μm.

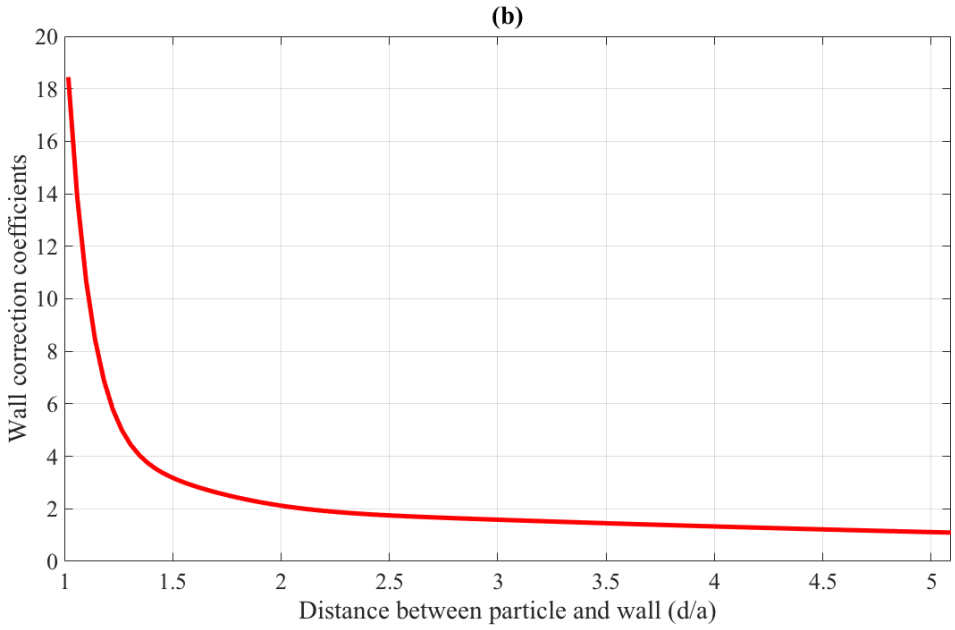

Fig. 6.4: Continued.

The microchannel used in the following experiments has the width of w = 375 μm and the depth of h = 56 μm. For a cell with the typical radius of 10 μm, the channel width is much larger than the cell radius. Therefore, the effects of the sidewall on the cell's motion can be ignored if the distance between the cell/microparticle and the sidewall is about ten times of its radius where the viscous drag force coefficients approaches to zero in theory[86]. As for the interaction between any two adjacent particles, if the distance between these particles is ten times larger than their radius[86], both the particles can be considered to move independently.

Here, it is assumed that the drag coefficients C_y and C_z are independent if a particle moves in both the y- and z-directions simultaneously[87]. Therefore, the viscous drag force equation in Eq. (3.13) is modified as

$$\mathbf{F}_v = -\mathbf{C} \cdot 6\pi\eta a\left(\mathbf{v}_p - \mathbf{v}_m\right) = -\hat{e}_y 6C_y \pi\eta a\left(v_{py} - v_{my}\right) - \hat{e}_z 6C_z \pi\eta a\left(v_{pz} - v_{mz}\right), \quad (6.2)$$

where $\mathbf{C} = [C_y\ C_z]^T$. For two infinite parallel plates, the viscous drag coefficients are dependent on the location of the particle and the location is the function of the particle's initial z-location z_0 and density ρ_p. That is, if z_0 and ρ_p are known, the particle's dropping velocity and viscous drag coefficients can be calculated, which is used to develop the property identification procedure based on the developed acoustophoretic model.

6.1.3. Forces Applied on Cell/Microparticle

As shown in Fig. 6.5, in a microchannel with an acoustic excitation, the motion of cells/microparticles is induced by four forces: acoustophoretic force, viscous drag force, gravity force, and buoyant force. If the cells are close to the wall, the wall effects on the viscous drag force need to be considered as discussed in the previous section. For the simulated trajectories, all the four forces as well as the wall effects are considered along with the density and compressibility of the cells/PS beads and the fluid medium. In addition, the acoustic streaming in the rectangular cross-section is included. Then, the cell's density and compressibility are identified by matching the experimental and simulated trajectories.

In the experiment, the trajectories of the PS beads and cells are recorded by using a vertical microscope: i.e., the particle's motion only in the horizontal plane (e.g., *xy*-plane) is recorded. At first glance, this horizontal motion seems not to be related to the motion in the *z*-direction. However, when a cell is dropping to the channel bottom due to its heavy density, the viscous drag force coefficients C_y and C_z vary depending on the

distance between the cell and the channel bottom. Then, the particle velocities in the *xy*-plane are affected by its *z*-location. Therefore, the trajectories recorded by the vertical microscope also include the information of the particle in the *z*-direction.

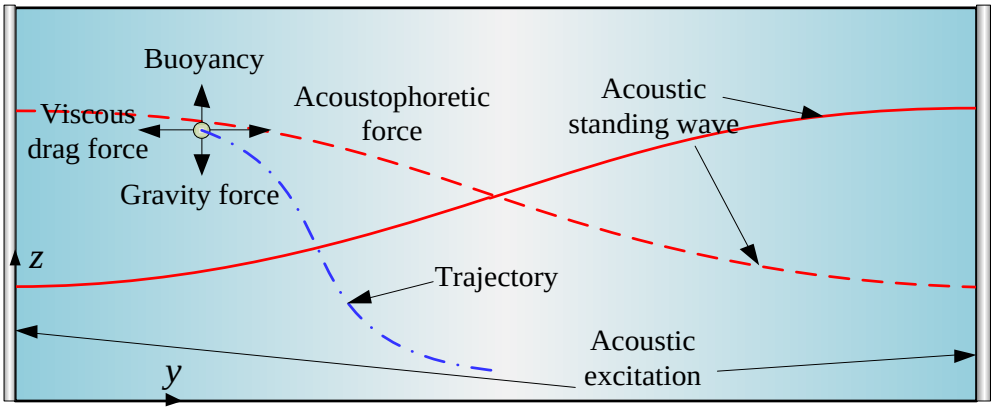

Fig. 6.5: Forces applied on cell/microparticle and its trajectory in rectangular cross-section of microfluidic channel. The red solid and dashed lines represent the acoustic pressure of the resonant standing wave. The four forces are applied on the cell/microparticle: i.e., acoustophoretic force, viscous drag force, gravity force, and buoyant force. The blue dashed line represents typical trajectory of the cell/microparticle.

For the calculation of the acoustophoretic force, the wavelength and the location of the acoustic pressure nodal line are required. Here, the wavelength is calculated from the given excitation frequency and the wave speed. In theory, at the first resonance of the microchannel, the acoustic pressure nodal line is in the microchannel center. However, due to the complex vibration of the device structure, the location of the pressure nodal line may not be in line with the theoretical prediction. Thus, it is determined from the experimental data as presented below.

The acoustophoretic force in Eq. (1.3), the viscous drag force in Eq. (6.2) (including both the acoustic streaming and the wall effects), and the buoyant and gravitational forces are used to calculate the cell/microparticle's motion from the Newton's Equation of Motion by using Eqs. (3.14) and (3.15). Then, the experimental trajectories are compared with the simulated trajectories with the cost function of

$$E_r = \sum_{n=1}^{N} \frac{\left(y_e^n - y_s^n \right)^2}{N}, \tag{6.3}$$

where y_e^n and y_s^n are the y-coordinates of the experimental and simulated trajectories, respectively, and N is the number of data points of the experimental trajectories. Here, the unknown parameters are the excitation pressure amplitude P_a, and the cell/particle's initial z-location z_0, density ρ_p, and compressibility β_p. For the identification of the excitation pressure in the microchannel using the PS beads, ρ_p and β_p are input to Eq. (6.3) and P_a is then obtained. For the identification of the cells's density and compressibility, ρ_p and β_p are calculated based on the calibrated pressure. In theory, the variables ρ_p, β_p and z_0 of cells can be optimally identified simultaneously. However, the optimized results, in particular, z_0 are sensitive to the quality of the extracted trajectories of the cells. Therefore, if the variable z_0 can be determined before the optimization, the identified ρ_p and β_p of the cells are less sensitive to large trajectory extraction errors.

6.1.4. Experiment Procedure

In addition to the excitation in the y-direction, an excitation in the z-direction is applied for the levitation of the cells/microparticles. If the z-levitation excitation is at the first resonance in the z-direction, the pressure nodal line is formed at $z = h/2$ and

cells/microparticles can be levitated approximately at $z_0 = h/2$.

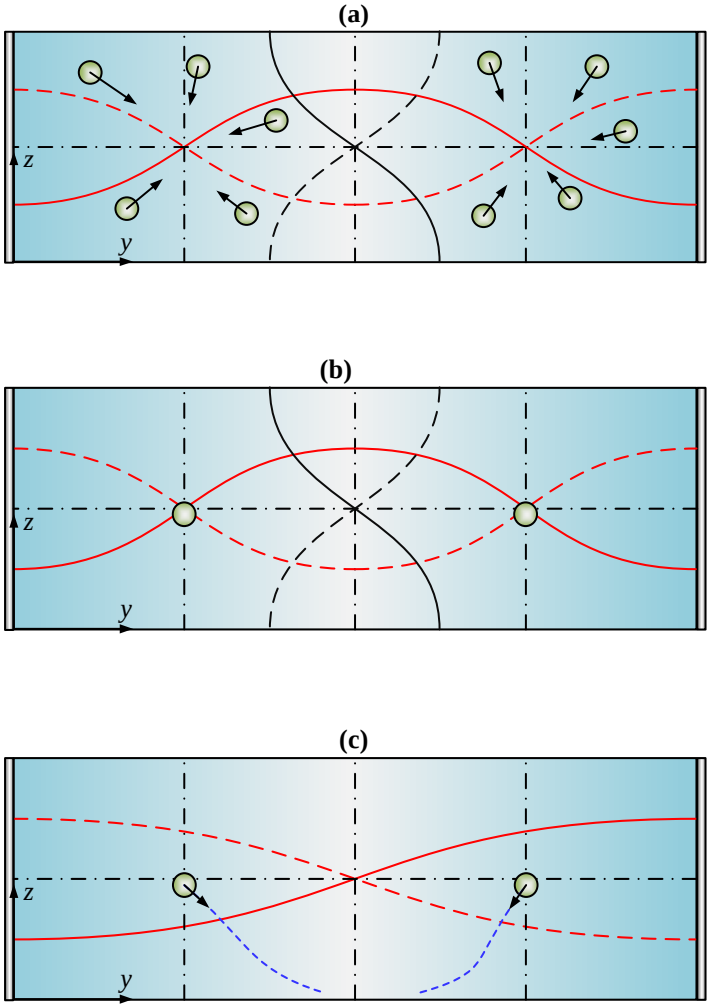

Fig. 6.6: Schematic of experimental procedure in cross-section of microchannel. (a) The cells/particles are distributed randomly at the beginning when the *z*-levitation and second *y*-direction resonant excitation are turned on. (b) The cells/particles are aggregated at the intersection of the pressure nodal lines. (c) The cells/particles move to the pressure nodal line in the middle of the channel while dropping when the only first *y*-direction resonant excitation is turned on.

The experiment procedure is illustrated in Fig. 6.6. In the cross-section of the

microchannel, by simultaneously turning the *z*-levitation excitation and the second *y*-direction resonant excitation on, the cell/particles move to the intersection of both the pressure nodal lines. When the particles flow into the excitation areas, they are aggregated and the initial *z*-locations of those particles are slightly lower than *h*/2 due to the balance of gravitational, buoyant, and acoustophoretic forces. Once the particles aggregated, the *z*-levitation and second *y*-direction resonant excitation is switched to the first *y*-direction resonant excitation. Then, the aggregated particles move from the second resonance pressure nodes to the first resonance pressure nodes while they are dropping down due to their heavy density.

In theory, the experimental procedure presented in Fig. 6.6 ensures that the initial *z*-location z_0 of the cells and PS beads are close to the channel center in the *z*-direction. In the experiment, it may not be the case and the optimization using the constant z_0 generates the property values with large variations, which will be discussed later in detail.

6.2. Experimental Results and Discussion

In the experiment, the fluid medium is water and its density and compressibility are known as 1000 kg/m^3 and 4.55×10^{-10} Pa^{-1}, respectively. The size of the cells can be measured from the recorded images and thus the other key parameters are the excitation pressure and the density and compressibility of the cells. From Eq. (1.3), the cell's compressibility and the excitation pressure cannot be identified at the same time because both parameters are coupled. Therefore, the acoustic pressure inside the microchannel must be calibrated in the first place.

6.2.1. Trajectories of PS Beads and Cells

From the recorded images of the cells and PS beads, their trajectories are extracted for further analyses. Figure 6.7 shows the trajectories of the PS beads and the head and neck cancer cells (686LN) under the same excitation condition. All the trajectories start from the *y*-locations close to the second resonance pressure nodal lines as shown in Figs. 6.7(a) and 6.7(b).

In the *x*-direction, the cells or PS beads are distributed randomly since the acoustophoretic force in this direction is weak. The radius, density and compressibility of the PS beads are 5.5 μm (measured), 1050 kg/m^3 (provided by the manufacturer), and 2.16×10^{-10} Pa^{-1}[39,74] (found from the references), respectively. Generally, the density of 686LN is similar to that of MCF-7, that is, 1068 kg/m^3[74] and its compressibility is approximately 4.22×10^{-10}[74]. The cells usually have much larger compressibility than the PS beads[74]. Under the same condition, the acoustophoretic forces applied on the PS beads are much larger than those on cells. This is why the PS beads move faster than cells in Fig. 6.7. In Figs. 6.7(a) and (b), some cells/microparticles move faster than the others. This is because the excitation pressure distribution is not uniform along the *x*-direction in addition to the variation in the initial *z* locations. Therefore, at the location of a large excitation pressure amplitude, the cells/microparticles move fast to approach to the pressure nodal line. Again, as discussed in Sec. 6.1.1, the smooth trajectories of both the PS beads and cells can be obtained by using the automatic and manual trajectory extraction programs as shown in Fig. 6.7.

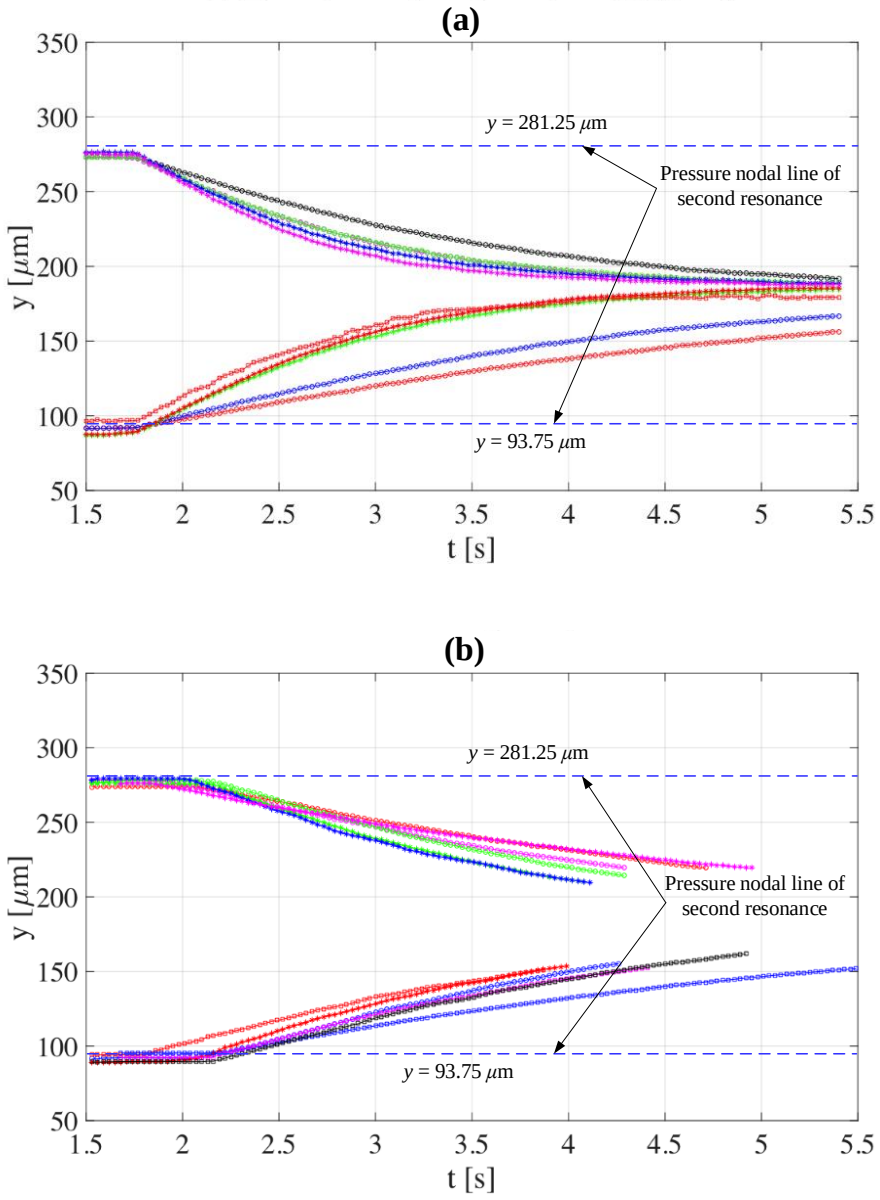

Fig. 6.7: Experimental trajectories of cells and PS beads. (a) Experimental trajectories of PS beads. (b) Experimental trajectories of 686LN. Due to the low compressibility of the PS beads, they move faster than the cells under the same excitation condition.

6.2.2. Calibration of Acoustic Excitation Pressure

The PS bead radius of 5.5 μm is much smaller than the channel depth of 56 μm, and thus the viscous drag coefficients do not change much if the PS beads are in the

range of 28±15 μm in the *z*-direction. For the calibration, the useful trajectory segment of PS beads is usually in the range of 230 - 270 μm or 100 - 150 μm in the *y*-direction (see Fig. 6.7). It takes about 1 - 3 s for PS beads to travel through this range and their corresponding dropping displacements in the *z*-direction are just 2-5 μm. Therefore, the drag coefficients can be assumed as a constant and the values for the initial *z*-location z_0 = 26 μm for all beads are used for the calibration of the excitation pressure level.

It is expected that the pressure nodal line is in line with the center of the microchannel. Then, all the PS beads should finally move to the center of the microchannel. However, it is observed that the final *y*-locations of all the beads are off from the microchannel center. Thus, the final *y*-locations of the PS beads after a sufficiently long time are considered as the pressure nodal lines. The offset values of the pressure nodal line from the channel center are shown in Fig. 6.8(a).

By fitting the experimental trajectories of the PS beads into the predicted trajectories, the excitation acoustic pressure amplitudes are calculated as a function of the *x*-location. The excitation pressure amplitudes are not symmetric with respect to the channel center as shown in Fig. 6.8(b) and (c). The acoustic pressure amplitude inside the microchannel varies along the *x*-direction and the pressure levels in the upper half channel are slightly different from those in the lower half channel. This asymmetry may come from the asymmetric structural excitation of the PZT actuator, the silicon chip, and the glass cover.

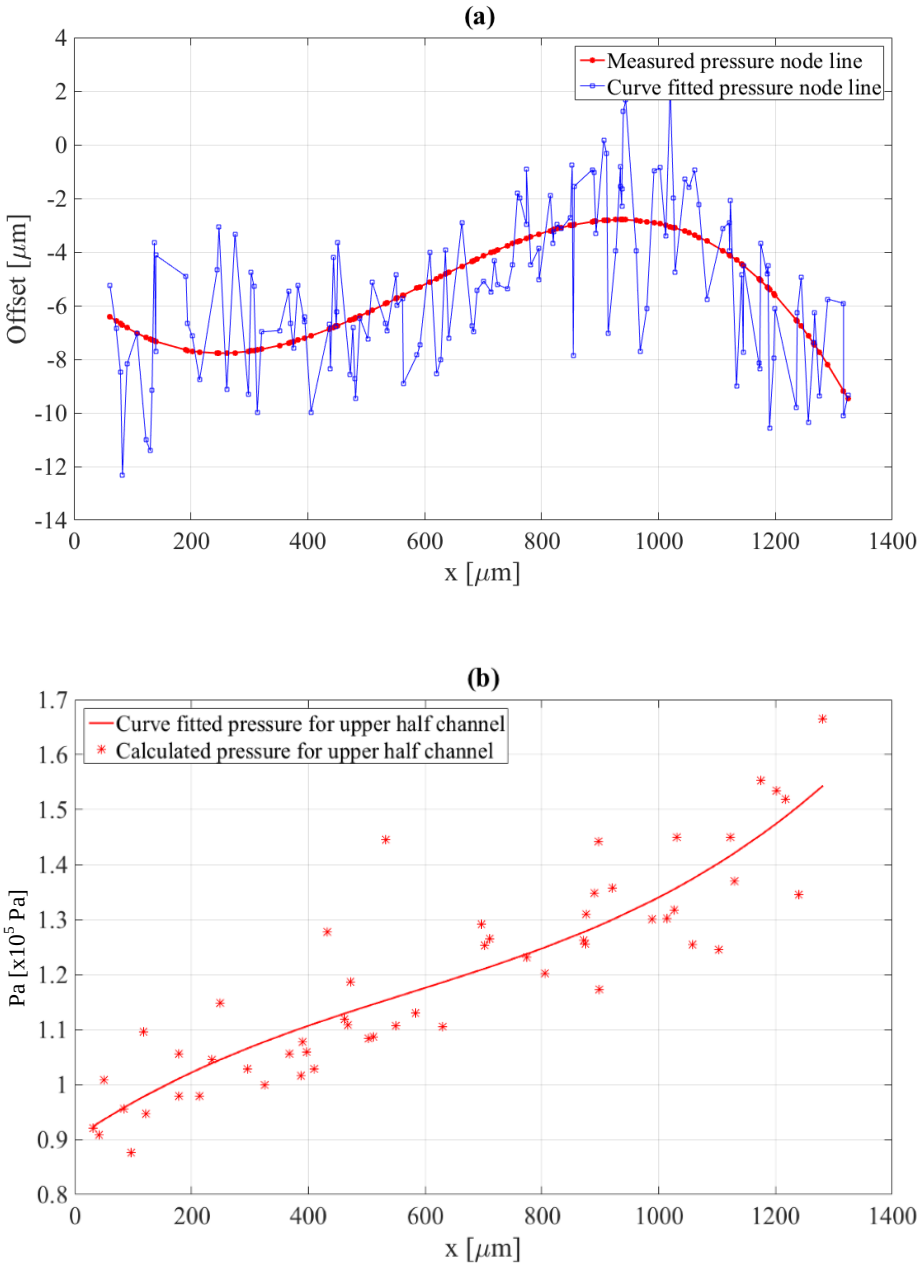

Fig. 6.8: Calibration of excitation acoustic pressure amplitude inside microchannel. (a) Offset of pressure node location with respect to channel center. (b) Calibrated excitation pressure amplitude for upper half of microchannel. (c) Calibrated excitation pressure amplitude for lower half of microchannel.

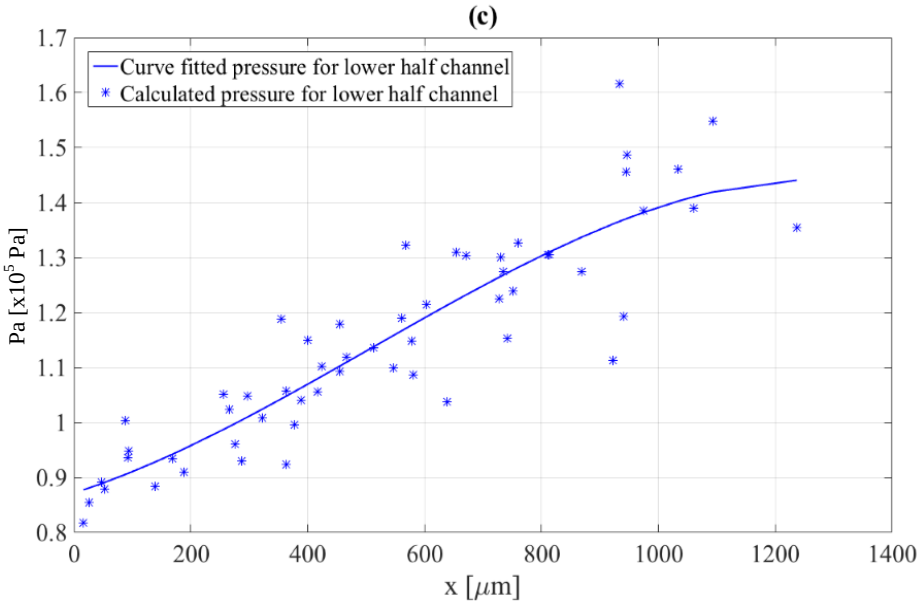

Fig. 6.8: Continued.

6.2.3. Identified Density and Compressibility of Cells

In the experiment, four cell lines are used for their biomechanical property identification: 37B, M4e, Tu686, and 686LN. All of them are head and neck cancer cell lines. Here, 37B and M4e have higher metastatic potential than Tu686 and 686LN[98]. After analyzing the cell size, it is found that the typical radii of these cells are in the range of [8, 12] μm. For the identification of the density and compressibility of the cells, the drag coefficient variation as the function of the z-location needs to be considered because the density of the cells is strongly correlated with the dropping velocity of the cells.

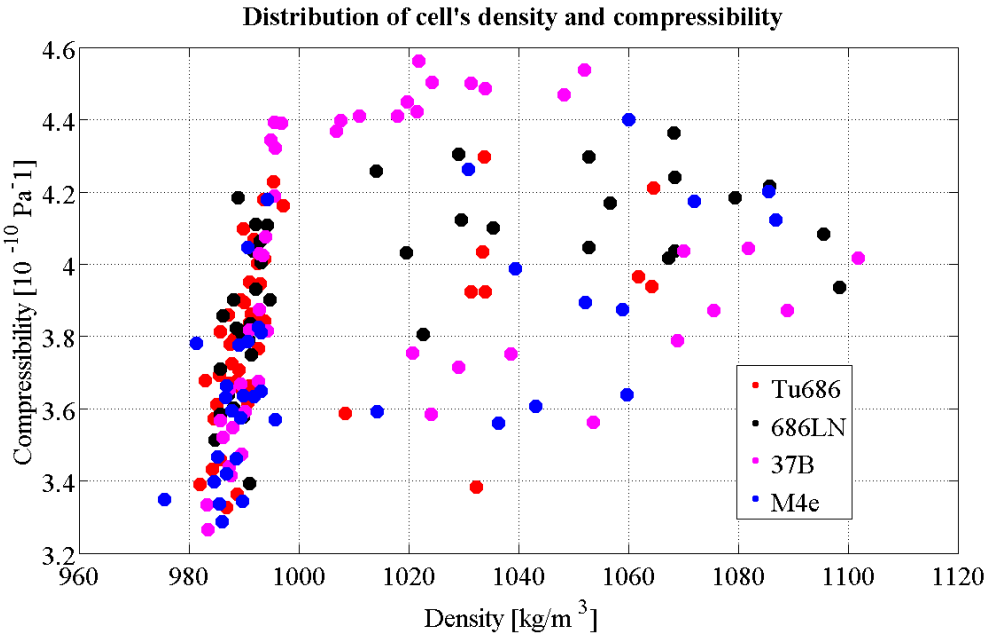

Fig. 6.9: Distribution of cell's density and compressibility for constant z_0 = 26 μm. The colors represent different cancer cell lines.

First, the initial height z_0 is set to be 26 μm and the unknown parameters are the density ρ_p and compressibility β_p of the cells. Note that the excitation acosutic pressure is already determined from the experiments with the PS beads. The identified biomechanical properties are shown in Fig. 6.9. It can be observed that the density of most cells are below 1000 kg/m^3, which is not consistent with the density reported in the literature[74]. In order to address this discrepancy, the initial location z_0 is varied from 26 μm. As described before, due to the complex structural vibration of the microfluidic device at the excitation frequency, the nodal line for the z-direction levitation may not be formed exactly in the middle.

Then, the initial height z_0 is set as an unknown variable and z_0 is determined by using the same optimization process as ρ_p and β_p. However, the three optimization

variables make the identification procedure sensitive to any experimental noise. Therefore, it is required to use long and smooth trajectories for the optimization process. If the trajectories are short or the cells do not drop down with an enough displacement, the optimization results have large statistical variations. Figure 6.10 shows the results obtained with the initial height z_0 set as the optimization variable. The density and compressibility of the cancer cells are scattered in a large range. The corresponding statistical results are shown in Table 6.1. The identified density and compressibility of Tu686 and 686LN agree with what are reported in the literature, and the corresponding standard deviations (STD) are reasonably acceptable.

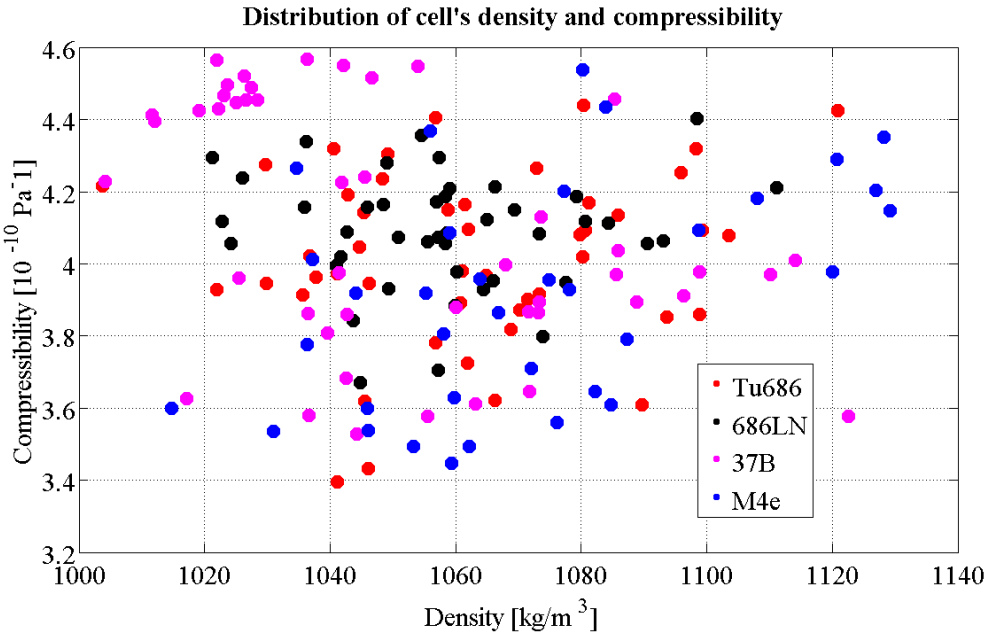

Fig. 6.10: Density and compressibility distribution of four cancer cells with initial height z_0 set as optimization variable. The colors represent the four different cancer cell lines.

Table 6.1: Statistical results of identified density and compressibility data

	Density [kg/m^3]		Compressibility [$\times 10^{-10}$ Pa^{-1}]	
	Mean	Standard deviation	Mean	Standard deviation
Tu686	1062.6	24.4	4.0185	0.2434
686LN	1058.4	20.1	4.0896	0.1616
37B	1051.3	29.9	4.0998	0.3386
M4e	1071.8	29.5	3.9124	0.3073

Table 6.2: Statistical results of grouped 37B experimental data

Data Set	Number of data points	Density [kg/m^3]		Compressibility [$\times 10^{-10}$ Pa^{-1}]	
		Mean	STD	Mean	STD
1-7	18	1032.1	17.7	4.4688	0.0772
8-23	28	1063.7	29.8	3.8626	0.1952

Regarding the results of 37B, it is observed that the first 7 experimental data sets are quite different from the rest data sets and the trajectories of these two groups are significantly different from each other. Table 2 shows the statistical results for these two groups of the experiment data. While the averaged densities of 37B in these two groups are reasonably closed to each other (i.e., 1032.1 kg/m^3 and 1063.7 kg/m^3), the averaged compressibilities are significantly different (i.e., 4.4688×10^{-10} Pa^{-1} and 3.8626×10^{-10} Pa^{-1}). This large compressibility difference of 0.6062×10^{-10} Pa^{-1} is not acceptable. This large difference may be caused by two possible reasons. The first one is that this cancer cell actually have a wide variation in its properties and the other one is that the excitation levels may be shifted significantly from the calibrated ones.

As for M4e, its compressibility is expected to be larger than Tu686 and 686LN since it has a lower metastatic potential than Tu686 and 686LN. However, the statistical

results identified with the optimization variable z_0 are not in line with this hypothesis.

The average and STD of the identified density and compressibility in Tables 6.1 and 6.2 are plotted in Fig. 6.11. Here, the 37B results are presented in the two groups as shown in Table 6.2. Figure 6.1 shows that the results of 37B data sets 1-7 are statistically different from those of Tu686 and 686LN, while the results of both 37B data sets 8-23 and the M4e data are difficult to be differentiated from those of Tu686 and 686LN due to the large statistical variations with these data. In Fig. 6.11(c), the optimized initial z-locations of cells z_0 are distributed in a wide range, which explains the reason that the optimization results are not acceptable for the fixed z_0 = 26 μm.

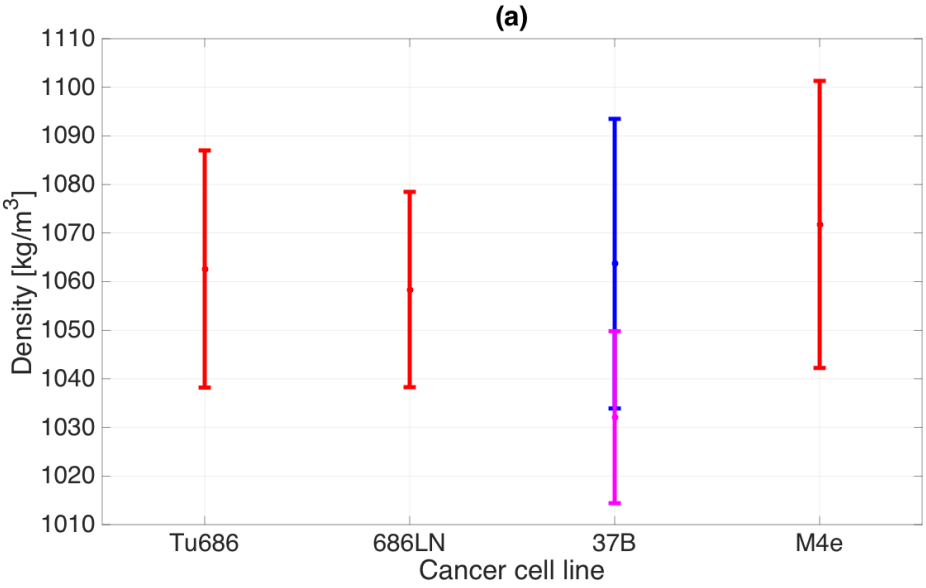

Fig. 6.11: Average and standard deviation of four cancer cells' properties with initial height z_0 set as optimization variable. (a) Average and standard deviation of cell's density. (b) Average and standard deviation of cell's compressibility. (c) Distribution of cell's initial z-locations. The pink curves represent the results from experimental data sets 1-7 and the blue curves represent the results from experimental data sets 8-23.

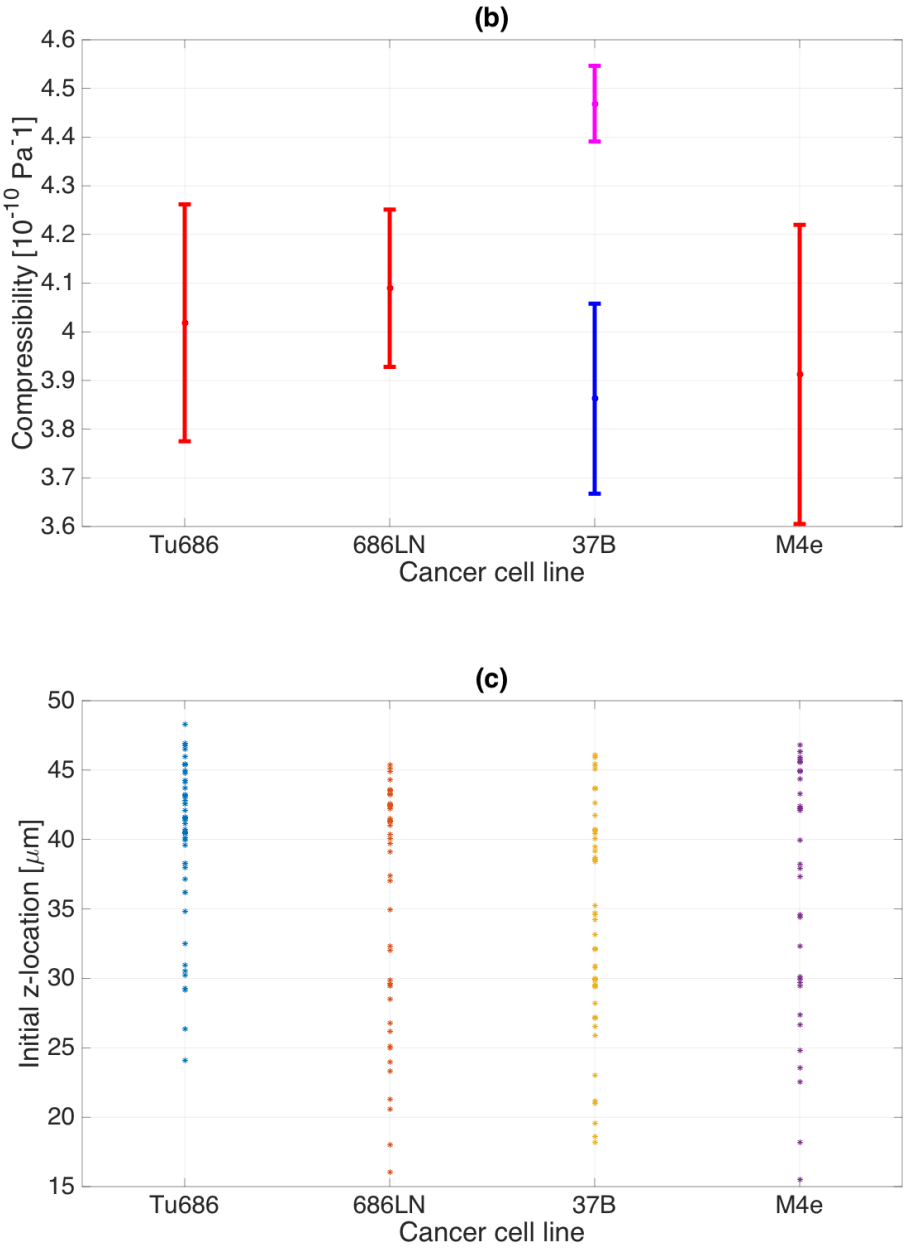

Fig. 6.11: Continued.

6.2.4. Effects of Cell/Microparticle's Radius and Temperature

In the microchannel, the cell/microparticle drops based on the balance between the gravity, buoyant and viscous drag forces, expressed as

$$\left(\rho_p - \rho_0\right)V_p g = 6\pi\eta a v_{pz} \tag{6.4}$$

where a is the radius of the cell/microparticle, V_p is the volume, $V_p = 4\pi a^3/3$. Therefore, the cell/microparticle's density is expressed as

$$\rho_p = \frac{9\eta v_{pz}}{2ga^2} + \rho_0 \tag{6.5}$$

Here, the density ρ_p is considered as a function of a and temperature T and its differential is expressed as

$$\delta\rho_p = -\frac{9\eta v_{pz}}{ga^3}\delta a + \frac{\partial\rho_0}{\partial T}\delta T \tag{6.6}$$

In the y-direction, the force equilibrium equation is

$$\frac{\pi P_a^2 V_p \beta_0}{2\lambda}\left[\frac{5\rho_p - 2\rho_0}{2\rho_p + \rho_0} - \frac{\beta_p}{\beta_0}\right]\sin\left(2ky\right) = 6\pi\eta a v_{py}\,, \tag{6.7}$$

and the cell/microparticle's compressibility is expressed as

$$\beta_p = \frac{5\rho_p - 2\rho_0}{2\rho_p + \rho_0}\beta_0 - \frac{18\eta v_{py}}{P_a^2 a^2 k\sin\left(2ky\right)}\,. \tag{6.8}$$

Then, the differential of β_p is written as

$$\begin{aligned}\delta\beta_p = {} & \frac{9\rho_0\beta_0}{\left(2\rho_p + \rho_0\right)^2}\delta\rho_p - \frac{9\rho_p\beta_0}{\left(2\rho_p + \rho_0\right)^2}\frac{\partial\rho_0}{\partial T}\delta T + \frac{36\eta v_{py}}{P_a^2 a^3 k\sin\left(2ky\right)}\delta a \\ & + \frac{18\eta v_{py}\left[\sin\left(2ky\right) + 2ky\cos\left(2ky\right)\right]}{P_a^2 a^2\left[k\sin\left(2ky\right)\right]^2}\frac{\partial k}{\partial T}\delta T\end{aligned} \tag{6.9}$$

By using $k = \omega/c_0$ and Eq. (6.6), Eq. (6.9) can be manipulated as

$$\delta\beta_p = \left[-\frac{81\rho_0\beta_0\eta v_{pz}}{\left(2\rho_p+\rho_0\right)^2 g a^3} + \frac{36\eta v_{py}}{P_a^2 a^3 k \sin\left(ky\right)} \right]\delta a + \left[-\frac{9\left(\rho_p-\rho_0\right)\beta_0}{\left(2\rho_p+\rho_0\right)^2}\frac{\partial\rho_0}{\partial T} - \frac{18\eta\omega v_{py}\left[\sin\left(2ky\right)+2ky\cos\left(2ky\right)\right]}{P_a^2 c_0^2 a^2\left[k\sin\left(2ky\right)\right]^2}\frac{\partial c_0}{\partial T} \right]\delta T \tag{6.10}$$

Eq. (6.6) and (6.10) are used to calculate the uncertainty due to the variation of the cell/microparticle's radius and temperature. Based on the experiment, the parameters are used as P_a = 10^5 Pa, v_{pz} = 2.7 μm/s, v_{py} = 30 μm/s, f = 1.97 MHz, a = 10 μm, T = 20 °C and $y = 3L_y/4$. Therefore, the uncertainty of ρ_p and β_p are calculated as

$$\Delta\rho_p = \sqrt{\left(2.480\times10^6\Delta a\right)^2 + \left(0.269\Delta T\right)^2} \tag{6.11a}$$

$$\Delta\beta_p = \sqrt{\left(1.396\times10^{-5} da\right)^2 + \left(1.409\times10^{-13} dT\right)^2} \tag{6.11b}$$

Assuming the uncertainty Δa = 0.5 μm and ΔT = 5 °C, the following equation is obtained.

$$\Delta\rho_p = \sqrt{1.240^2 + 1.346^2} = 1.830\,\mathrm{kg/m^3} \tag{6.12a}$$

$$\Delta\beta_p = \sqrt{\left(6.980\times10^{-12}\right)^2 + \left(0.704\times10^{-12}\right)^2} = 7.015\times10^{-12}\,\mathrm{P_a^{-10}} \tag{6.12b}$$

It is obvious that the effects of the cell/microparticle's radius and temperature variation are insignificant.

6.3. Conclusion

The model for analyzing the acoustophoretic motion of the cancer cells and microparticles in the cross section of the rectangular microchannel is used for both the

excitation pressure calibration inside the microchannel and the identification of the cells' density and compressibility. The forces applied on the cells and microparticles include the acoustophoretic force, the viscous drag force, the gravitational force, and the buoyant force. Here, the acoustic streaming and the wall effects are also taken into account for the accurate identification of the biomechanical properties. Based on the acoustophoretic model, the procedure for identifying the density and compressibility of the cells is proposed. By analyzing the motion of the PS beads inside the microchannel, the excitation acoustic pressure distribution inside the microchannel is calibrated. The excitation pressure levels vary along the *x*-direction and are different in the upper and lower half channel, which may come from the asymmetric vibration excited by using the PZT actuators. Based on the calibrated excitation pressure, the density and compressibility of the four head and neck cancer cells are identified by fitting the simulated trajectories into the experimental cancer cells' trajectories. The identified biomechanical properties of 686LN, Tu686 and the first part of the 37B experimental data are statistically meaningful, while the results of the rest of the 37B data and the M4e data have the large statistical variations. A further investigation in the near future need to be made to reduce these large statistical variations.

7. DOUBLE-WIDTH SEPARATION MICROCHANNEL

It is of great interest to separate cells/microparticles depending on differences in their mechanical properties without tagging labels at high throughput. However, using traditional acoustophoretic separation devices, it is difficult to separate cells/microparticles with "subtle" mechanical property differences due to the low separation resolution of these devices. In this chapter, a novel, acoustophoretic, microfluidic design is proposed to address this problem.

7.1. Traditional Design of Microfluidic Microparticle Separation Device

The acoustophoretic cell/microparticle separation has gained significant interest in recent years and various microfluidic, acoustophoretic separation devices have been designed and tested to separate cells and microparticles depending on their vibro-acoustic properties. In these devices, the final location of a specific cell or particle is determined at a location where acoustophoretic force is in balance with viscous drag force. In order to explain this force balance, a simple microchannel is illustrated in Fig. 7.1.

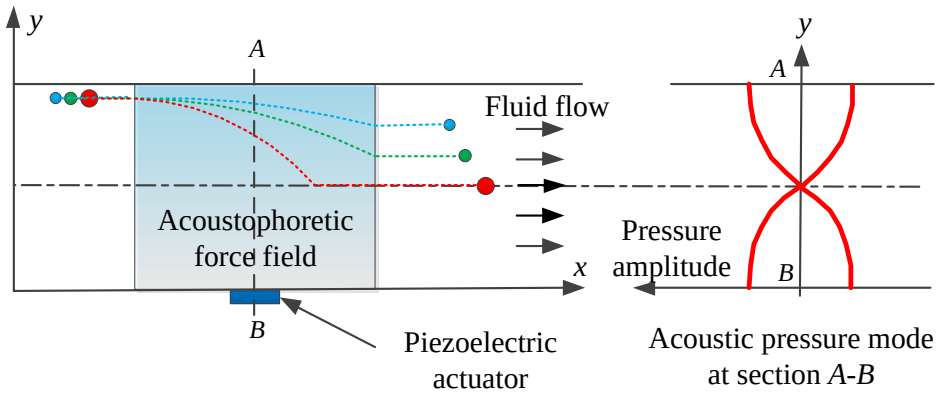

Fig. 7.1: Illustration of cell/microparticle separation inside microchannel (top view).

In the microchannel shown in Fig. 7.1, the piezoelectric actuator attached to the sidewall or the bottom of the channel generates an acoustic standing wave inside the microchannel (as shown in the acoustic pressure mode at section *A*-*B*), forming the acoustic pressure nodal line (i.e., zero acoustic pressure line) in the middle of the channel and the acoustical pressure anti-nodal lines at the sidewalls. In the *xy* plane, two forces are applied on a microparticle or cell: i.e., the acoustophoretic force induced by the acoustic excitation and the viscous drag force induced by the fluid flow. When cells/microparticles with different mechanical properties flow into the area of the acoustic standing waves, the acoustophoretic force induces the cells/microparticles to move towards the pressure node or antinode in the *y*-direction, while these cells/microparticles are also moving with the fluid medium flowing in the *x*-direction. The acoustophoretic and viscous drag forces determined by the different cell/microparticle's properties finally move these particles to different *y*-locations as shown in Fig. 7.1.

One advantage of the microfluidic device design in Fig. 7.1 is that the viscous drag force can be easily introduced with the fluid flow without special equipment. A traditional design of microfluidic channels is shown in Fig. 7.2. This microfluidic device is composed of one straight main channel, two inlets, and three outlets. However, the separation resolution of this device is generally low: i.e., the property difference of two different cells/microparticles needs to be larger enough to be separated into the two different outlets.

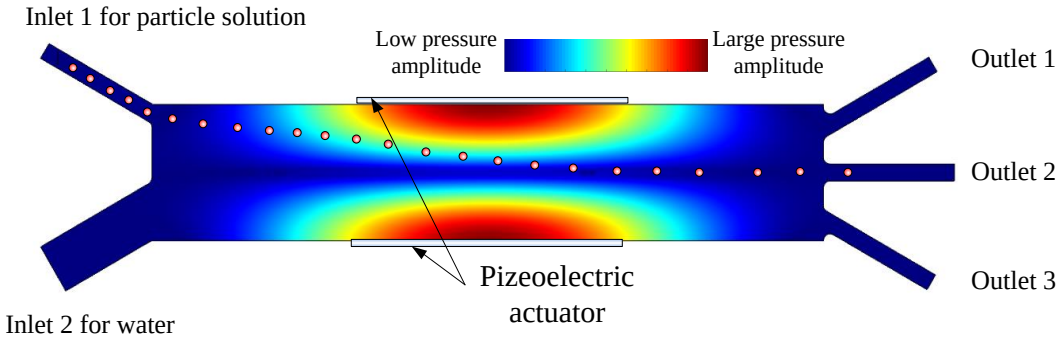

Fig. 7.2: Conventional design for microfluidic, acoustophoretic separation of cells/microparticles. The main separation segment is a straight microchannel in the middle. By making the fine adjustment of the fluid medium flow and the excitation level of the piezoelectric actuator, different cells/microparticles can flow into different outlets depending on their mechanical properties.

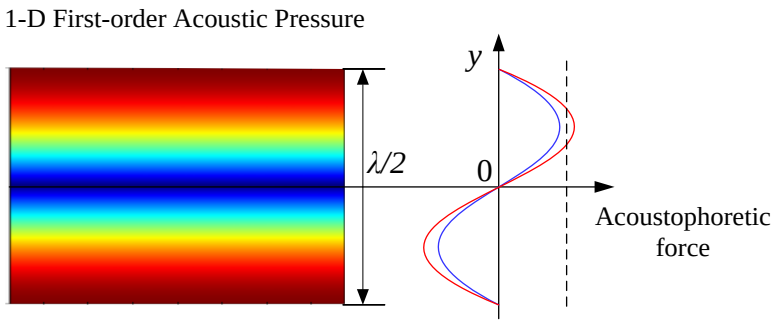

Fig. 7.3: 1-D acoustophoretic forces applied on two microparticles with two different sets of mechanical properties. The solid red and blue lines represent the acoustophoretic forces applied on two microparticles with different mechanical properties. The black dashed line represents an external force, whose magnitude is between the magnitudes of the two acoustophoretic forces, leading to have the two net forces to be in the opposite directions to each other.

In order to have further understanding on the separation process, the 1-D acoustophoretic force is plotted by using Eq. (1.3) in Fig. 7.3. The acoustophoretic forces applied on two microparticles with two different sets of mechanical properties have the largest difference at $y = \lambda/8$ away from the pressure node. In general, this subtle force difference is not distinguishable enough to make a detectable displacement difference in the y-direction, leading to a poor separation resolution in conventional, acoustophoretic, microfluidic separation devices. In general, the detectable displacement difference requires a significant large difference in the mechanical properties of the cells/microparticles.

In order to separate the cells/microparticles with the subtle acoustophoretic force difference shown in Fig. 7.3, it is here proposed to introduce an external force, in the opposite direction to the acoustophoretic force, of which the force magnitude is between

the magnitudes of the two acoustophoretic forces (see the dashed line in Fig. 7.3). Then, the net forces (i.e., the summation of the acoustophoretic force and the external force) at $y = \lambda/8$ will be positive with the small acoustophoretic force and negative with the large acoustophoretic force. Then, the two particles at this location will move in the opposite directions to each other with the external force regardless of their subtle property difference.

7.2. Novel Design of Microfluidic Microparticle Separation Device

In order to separate the cells/microparticles depending on their subtle mechanical property difference based on the aforementioned idea, a novel, innovative microchannel design is proposed as shown in Fig. 7.4. In this design, the fluid medium flow is used to generate a large flow gradient in the separation area so that the viscous drag force is induced by the flow as the external force in balance with the acoustophoretic forces. In the separation segment in Fig 7.4, the fluid medium flow has the *y*-direction velocity component, depending on the width ratio of outlets 1 to 2, while the acoustophoretic forces are applied mainly along the *y*-direction. Therefore, in the *y*-direction, if the magnitude of the viscous drag force due to the fluid flow is in-between the two acoustophoretic forces, the combination of both the forces can move the cells/microparticles to different outlets.

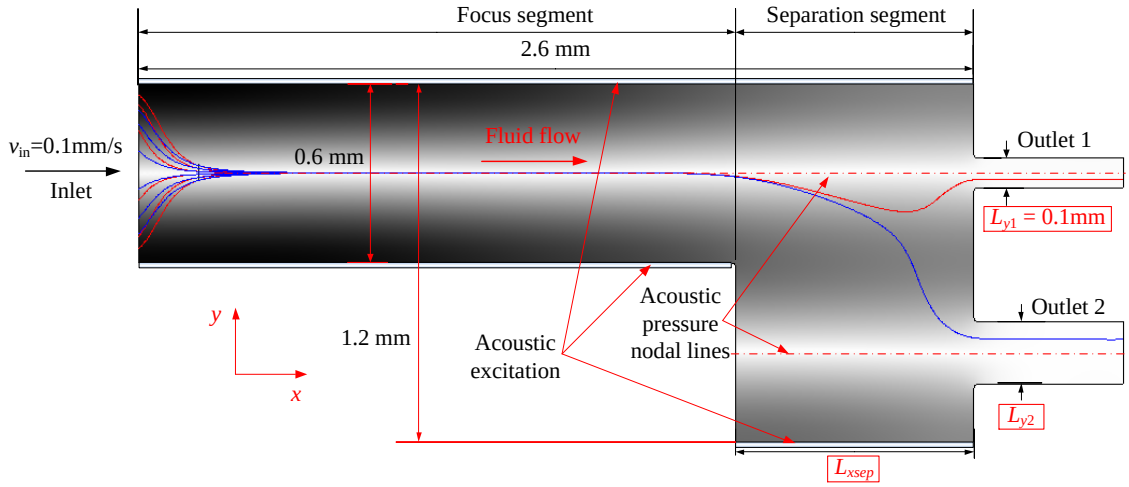

Fig. 7.4: Numerical simulation of microparticle separation in double-width microchannel. The red and blue lines represent the trajectories of polystyrene (PS) and polymethyl methacrylate (PMMA) beads, respectively. The fluid flow speed is 0.1 mm/s. Dimensions of double-width separation device are determined. Here, L_{y1}, L_{y2} and L_{xsep} are the parameters to be determined.

In Fig. 7.4, the red and blue lines represent the numerically analysed trajectories of a polystyrene (PS) bead and a polymethyl methacrylate (PMMA) bead, respectively. The size of both the beads is 10 μm in diameter, and the density and compressibility of the PS and PMMA beads are 1050 kg/m^3 and 1180 kg/m^3, and 2.65×10^{-10} Pa^{-1} and 3.67×10^{-10} Pa^{-1}, respectively. The numerically simulated trajectories in Fig. 7.4 show that both the microparticles can be separated successfully, moving the PS beam to outlet 1 and the PMMA to outlet 2.

One advantage of the proposed microfluidic channel design is that in the "focus segment", the cells/microparticles can be aligned to the pressure nodal line in the middle of the channel under the effects of the acoustophoretic force before entering the "separation segment". This alignment of the cells/microparticles can provide an

accurate control of their initial *y*-positions before entering the separation segment, promoting the high separation resolution.

For the microfluidic channel in Fig. 7.4, its dimensions and excitation level can be optimally determined to further improve the separation resolution. The important dimensions are the outlet widths (L_{y1} and L_{y2}) and the separation segment width (L_{xsep}) that will control the viscous drag forces. Here, the width of outlet 1 is first set to be L_{y1} = 0.1 mm and thus the L_{xsep} and L_{y2} are to be optimally determined based on the outlet 1 width.

Figure 7.5(a) shows the required excitation velocity range (i.e., subtraction of the minimum excitation velocity level from the maximum) that can be used to separate both the beads as the functions of L_{xsep} and L_{y2}. In this figure, the black circle represents the areas for the optimal design that gives the maximum excitation velocity range. In the middle of this optimization area, the channel dimensions can be determined as L_{xsep} = 0.64 mm and L_{y2} = 0.37 mm with the excitation velocity range of 0.4 mm/s. However, in the maximum pressure amplitude plot (Fig. 7.5(b)), the corresponding acoustic pressure amplitude is about 5.7×10^5 Pa, which requires a high input power. Therefore, the red circle in Fig. 7.5(a) indicates the second optimal area where the compromise between the excitation velocity range and the acoustic pressure amplitude can be made. In the middle of the red circle, the dimensions can be selected as L_{xsep} = 0.98 mm and L_{y2} = 0.19 mm where the excitation velocity range is 0.11 mm/s, and the corresponding pressure amplitude is about 2.54×10^5 Pa. Based on these two selected dimensions, microfluidic devices will be manufactured and tested. Other microfluidic device with the dimensions

of L_{xsep} = 0.95 mm, L_{y2} = 0.21 mm, and L_{y1} = 0.05 mm has already been fabricated and tested, as presented in the following section.

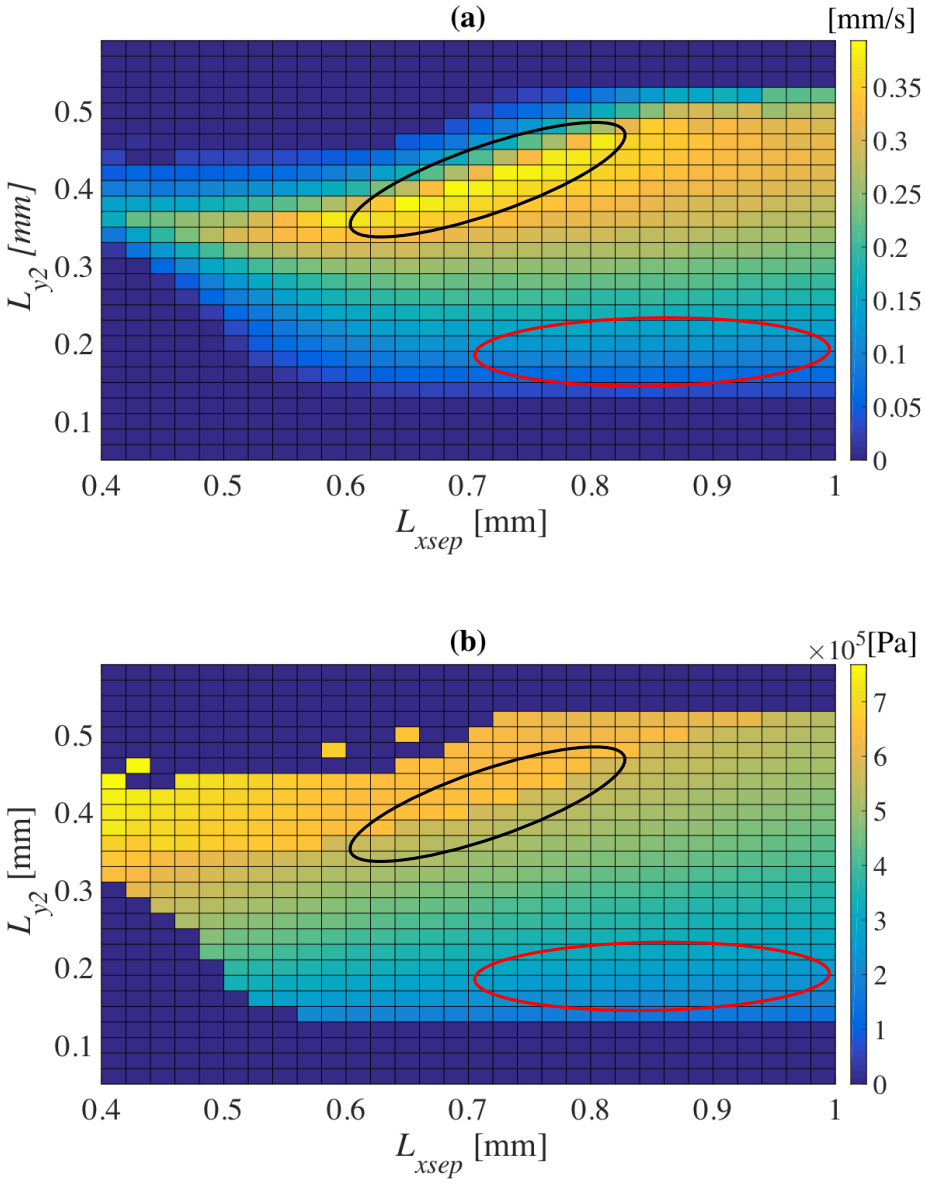

Fig. 7.5: Optimal design for double-width microfluidic separation device. (a) Excitation velocity range required for separation of PS and PMMA particles. (b) Maximum acoustic pressure amplitude. The maximum acoustic pressure amplitude is calculated at the maximum excitation velocity for the separation of the PS and PMMA beads.

7.3. Experiment and Future Work

Prior to the optimization of the dimensions in the previous section, a microchannel has been fabricated with the dimensions of L_{xsep} = 0.95 mm, L_{y1} = 0.05 mm, and L_{y2} = 0.21 mm. The experiment setup is shown in Fig. 7.6(a). Here, the microfluidic channel is etched on a silicon chip and a PDMS layer is attached on the silicon chip to form a closed microfluidic channel as shown in Fig. 7.6(b). A PZT actuator is attached to the bottom of the device using wax. The photos of the experimental setup and the fabricated channel are shown in Figs. 7.6(c) and 7.6(d).

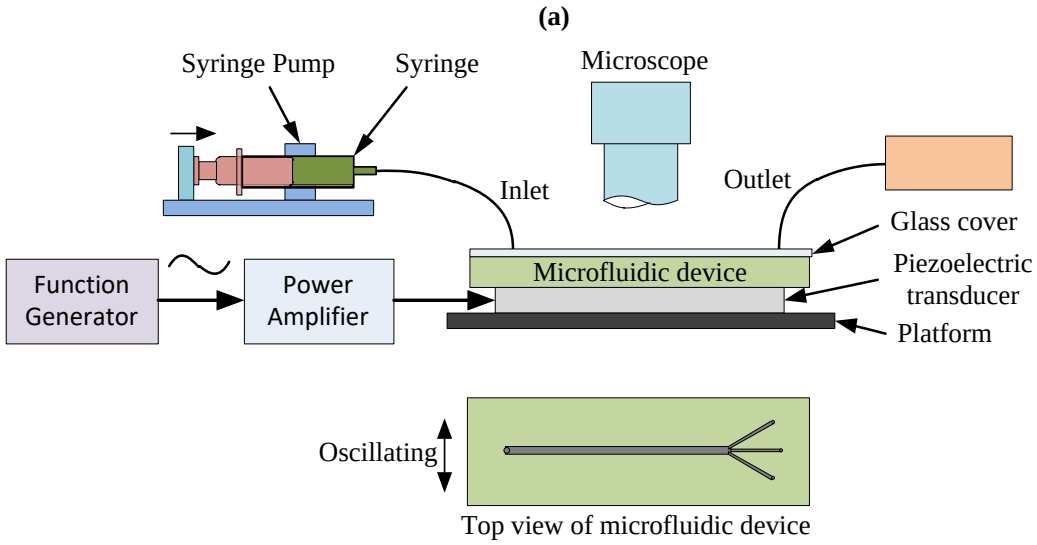

Fig. 7.6: Experiment setup of double-width microparticle separation. (a) Schematic of experimental setup. (b) Cross-sectional view of microfluidic device. (c) Photo of experimental setup. (d) Top view of microchannel captured by using microscope. The polymer beads are injected into the microfluidic device through the syringe pump. The PZT transducer excites the microfluidic device sinusoidally.

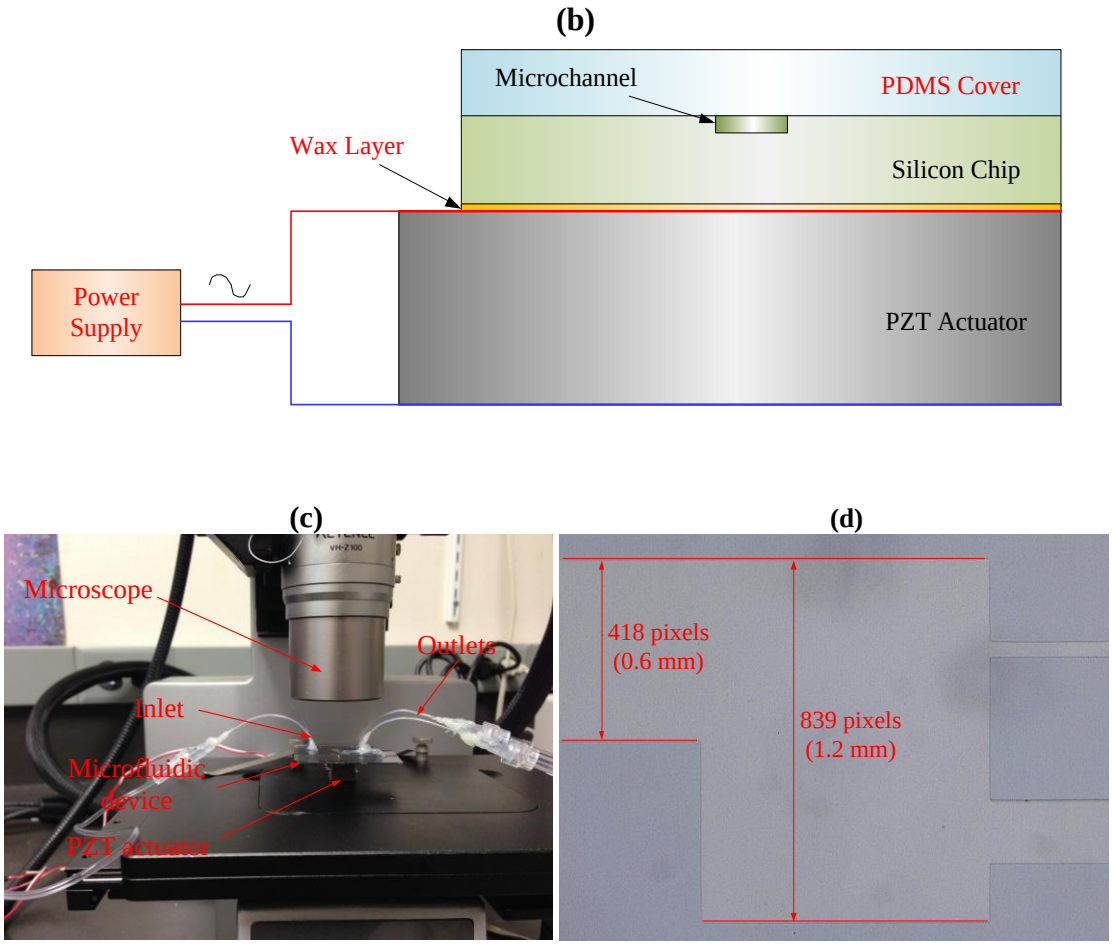

Fig. 7.6: Continued.

To experimentally test the proposed device, the PS and PMMA beads were injected to the device with water. The diameter for both the particles is 10 μm. The density of the PS and PMMA are 1050 kg/m^3 and 1180 kg/m^3, respectively and the compressibility are 2.65×10^{-10} Pa^{-1} and 3.67×10^{-10} Pa^{-1}.

In the experiment, a National Instruments (NI) Arbitrary Waveform Generator (Model: PXI-5421) was used to provide a sinusoidal signal to the PZT actuator via an ultrasonic power amplifier. However, the acoustophoresis phenomenon was not

observed for the beads. In order to explain this abnormality, the material properties of the microfluidic device were investigated. As shown in Table 3, the PDMS used as the top cover of the device (Fig. 7.6(b)) is very soft and its shear wavelength is significantly shorter than the shear wavelength in the other materials, which negatively affects the formation of the resonant standing wave inside the microchannel. The effects of the PDMS cover on the resonant standing wave were further investigated numerically by modelling the cross-section of the device in Fig. 7.6(b) in a commercial software package, COMSOL. In addition, the glass and PDMS covers are compared by building the COMSOL models with the two difference covers. In the model, the Young's modulus of the PDMS is set to be 10^7 Pa for a fast computation with a relatively small number of meshes, although the realistic value of 10^6 Pa in Table 3 gives worse results than the case of 10^7 Pa in terms of the resonant standing wave formation. The compliance and coupling matrices used to model the piezoelectric (PZT) actuator can be found in Ref. 89. The damping for the PZT, glass and PDMS is assumed to be 0.001.

Table 7.1: Material properties used to model cross-section of microfluidic device

Material	Density [kg/m^3]	Young's modulus [Pa]	Poisson's Ratio	Pressure wave		Shear wave	
				Wave speed [m/s]	Wavelength [mm]	Wave speed [m/s]	Wavelength [mm]
Glass	2210	7.4e10	0.3	6713.8	5.44	3588.7	2.91
PDMS	967[90]	1e6[91]	0.4999	1312	1.06	18.56	0.015
Silicon	2329	17e10	0.28	9660	7.82	5339.7	4.32
PZT	7600	8.0e10	0.35	3016	2.44	1974	1.60

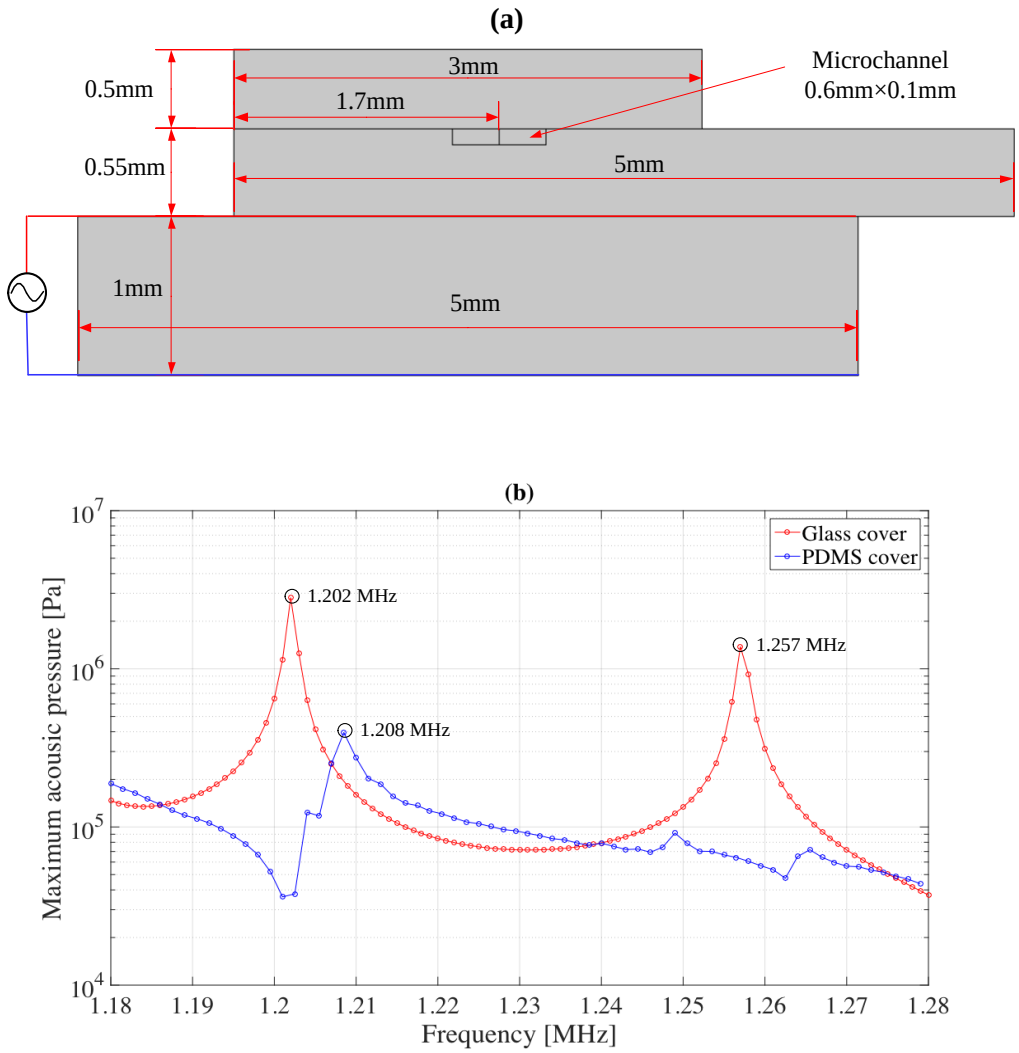

Fig. 7.7: Cross-sectional dimensions of microfluidic device for COMSOL modeling and numerical analysis results. (a) Cross-sectional dimensions of microfluidic device. (b) Maximum acoustic pressure inside microchannel as function of excitation frequency. (c) Acoustic pressure distribution inside microchannel for glass cover at 1.198 MHz. (d) Acoustic pressure distribution inside microchannel for PDMS cover at 1.28 MHz.

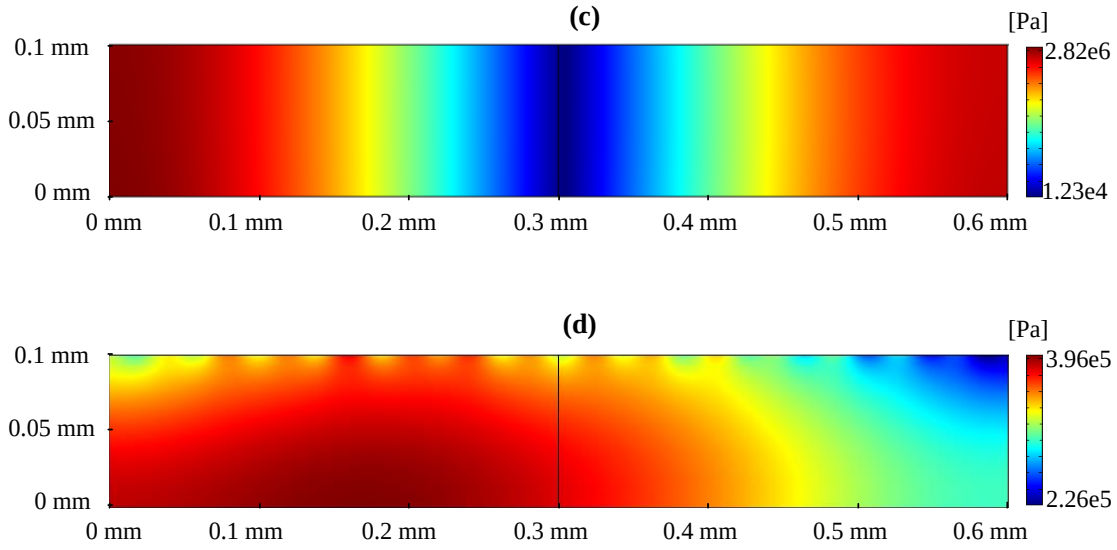

Fig. 7.7: Continued.

In the COMSOL model, the microchannel's width and height are set to be 0.6 mm and 0.1 mm, respectively. The other dimensions are selected arbitrarily as shown in Fig. 7.7(a). It is also assumed that the PZT actuator is directly attached to the bottom of the device without a bonding layer. In Fig. 7.7(b), the maximum acoustic pressure amplitude inside the microchannel is calculated as a function of the excitation frequency with the PDMS and glass covers. The results of the two covers are different significantly from each other. From the maximum acoustic pressure with the glass cover, the resonance peaks are observed obviously, e.g., at 1.202 MHz, while it is difficult to identify the resonance peaks for the PDMS cover in Fig. 7.7(b). The peak frequency 1.257 MHz in Fig. 7.7(b) is found not to be the resonance of the microchannel and this amplitude peak is attributed to the resonance of the whole device. The acoustic pressure distribution inside the microchannel at 1.202 MHz is shown in Fig. 7.7(c) for the case of the glass cover. The frequency of 1.202 MHz is selected here since it is close

to the first acoustic resonant frequency of the microchannel. Fig. 7.7(c) shows the resonant acoustic pressure distribution in which there are the acoustic pressure nodal lines in the middle of the channel and the acoustic pressure anti-nodes at the sidewalls. The acoustic pressure distribution with the PDMS cover is shown in Fig. 7.7(d) at 1.208 MHz which is a peak frequency, in Fig. 7.7 (b), close to the first acoustic resonance frequency. As for the case of the PDMS cover, an acoustic resonance inside the microchannel cannot be observed at all from the acoustic pressure distribution. The acoustic pressure distributions at other excitation frequencies are similar to the one in Fig. 7.7(d). Since the PDMS is soft, it dissipates the acoustic energy significantly, preventing the formation of the acoustic resonance inside the microchannel. Therefore, for the acoustophoretic manipulation of the cells/microparticles at the acoustic resonance frequencies, a hard material should be used to fabricate the microfluidic channel. In particular, the hard glass cover is recommended in place of the soft PDMS cover.

7.4. Conclusion

Here, the novel design of the acoustophoretic microfluidic separation device was proposed and validated numerically. Through the numerical simulation, it is shown that the two-stage double width device can be excited at a single frequency to generate the acoustic resonant standing waves in both the focus and separation segments. Thus, the acoustic excitation can be achieved with a simple piezoelectric actuator. It is also shown that the dimensions of the device can be further optimized to maximize the excitation velocity range for the separation of the particles with subtle mechanical property difference by using the COMSOL models.

In designing an acoustophoretic microfluidic device, the materials used to fabricate the device have a crucial role in the generation of the acoustic resonance inside the microchannel. The device materials and the structure have an important effect on the formation of the acoustic resonance. Through the numerical analysis results of the two COMSOL models with the PDMS and glass covers, it was shown that the PDMS cover could not give any acoustic resonances inside the microchannel due to the energy dissipation caused by this soft material, while the glass cover could provide high-level acoustic resonances. Therefore, in manufacturing the device in the near future, the materials should be selected carefully, to minimize any acoustic energy dissipation.

8. SUMMARY

In this dissertation, two types of acoustophoresis are introduced and validated numerically and experimentally. The first acoustophoresis is the one in the microfluidic devices. Here, it is proposed to develop a numerical modeling method that includes the effects of the moving fluid media and the temperature variation. Through the modeling analyses using the proposed numerical method, it was shown that the fluid medium flow and the temperature variation affected the acoustophoretic forces and the acoustic streaming significantly. Based on the modeling method, two applications are developed as following. (1) The trajectories of the cancer cells or PS beads were analyzed by using the proposed modelling approach. By fitting experimental trajectories into the predicted one, the acoustic pressure distribution inside the microchannel were calibrated first and then the mechanical properties of the cells could be identified. (2) Based on the proposed modeling approach, a novel separation device design was proposed to separate the cells or microparticles depending on their subtle compressibility differences. The device consists of two stages where cells/microparticles are first aligned in the center of the microchannel and then separated depending on their subtle compressibility differences.

The second acoustophoresis is generated around cells/microparticles. A new analytical algorithm is proposed to significantly improve computational efficiency as well as computational accuracy in the farfield. The proposed algorithm is validated by comparing the results of the proposed method against those of a traditional method.

Based on the analytical modelling approaches, the following applications have been investigated in this dissertation. The frequency responses of the acoustophoretic forces and acoustic streaming around the cells or microparticles were calculated and then the resonance frequencies were identified at the local maxima of the acoustic streaming velocities. Then, the experiments on the acoustic streaming around a cancer cell MCF-7 and PLGA microparticle were conducted and the local maxima of the acoustic streaming velocities were picked, and thus the properties of those particles were identified that agrees with the published data.

REFERENCES

[1] L. Kang, B. G. Chung, R. Langer and A. Khademhosseini, "Microfluidics for drug discovery and development: from target selection to product lifecycle management," *Drug Discov Today*, 2008, **13**, 1-13.

[2] M. Eisenstein, "Cell sorting: divide and conquer," *Nature*, 2006, **441**, 1179–1185.

[3] H. Jönsson, A. Nilsson, F. Petersson, M. Allers, and T. Laurell, "Particle separation using ultrasound can be used with human shed mediastinal blood," *Perfusion*, 2005, **20**, 39-43.

[4] C. W. Yung, J. Fiering, A. J. Mueller and D. E. Ingber, "Micromagnetic-microfluidic blood cleansing device," *Lab Chip*, 2009, **9**, 1171–1177.

[5] D. R. Gossett, W. M. Weaver, A. J. Mach, S. C. Hur, H. T. K. Tse, W. Lee, H. Amini, and D. D. Carlo, "Label-free cell separation and sorting in microfluidic systems," *Anal. Bioanal. Chem.*, 2010, **397**, 3249-3267.

[6] A. Lenshof and T. Laurell, "Continuous separation of cells and particles in microfluidic systems," *Chem. Soc. Rev.*, 2010, **39**, 1203-1217.

[7] H. Tsutsui and C.-M. Ho, "Cell separation by non-inertial force fields in microfluidic systems," *Mech. Res. Commun.*, 2009, **36**, 92-103.

[8] K. H. Han, A. Han and A. B. Frazier, "Microsystems for isolation and electrophysiological analysis of breast cancer cells from blood," *Biosens. Bioelectron.*, 2006, **21**, 1907-1914.

[9] J. Takagi, M. Yamada, M. Yasuda and M. Seki, "Continuous particle separation in a microchannel having asymmetrically arranged multiple branches," *Lab Chip*, 2005, **5**, 778-784.

[10] A. A. S. Bhagat, S. S. Kuntaegowdanahalli and I. Papautsky, "Continuous particle separation in spiral microchannels using dean flows and differential migration," *Lab Chip*, 2008, **8**, 1906-1914.

[11] L. R. Huang, E. C. Cox, R. H. Austin and J. C. Sturm, "Continuous particle separation through deterministic lateral displacement," *Science*, 2004, **304**, 987-990.

[12] S. Kapishnikov, V. Kantsler, and V. Steinberg, "Continuous particle size separation and size sorting using ultrasound in a microchannel," *J. Stat. Mech. Theor. Exp.*, 2006, P01012-1742.

[13] F. Petersson, L. Aberg, A.-M. Swärd-Nilsson, and T. Laurell, "Free flow acoustophoresis: microfluidic-based mode of particle and cell separation," *Anal. Chem.*, 2007, **79**, 5117-5123.

[14] M. Evander, A. Lenshof, T. Laurell, and J. Nilsson, "Acoustophoresis in wet-etched glass chips," *Anal. Chem.*, 2008, **80**, 5178-5185.

[15] J. Shi, H. Huang, Z. Stratton, Y. Huang, and T. J. Huang, "Continuous particle separation in a microfluidic channel via standing surface acoustic waves (SSAW)," *Lab Chip*, 2009, **9**, 3354-3359.

[16] J. Nam, Y. Lee, and S. Shin, "Size-dependent microparticles separation through standing surface acoustic waves," *Microfluid Nanofluid*, 2011, **11**, 317-326.

[17] L.V. King, "On the acoustic radiation pressure on spheres," *Proceedings of the Royal Society of London, Ser. A,* 1934, **147**, 212-240.

[18] K.Yosioka and Y.Kawasima, "Acoustic radiation pressure on a compressible sphere," *Acustica,* 1955, **5**, 167-173.

[19] L. P. Gorkov, "On the forces acting on a small particle in an acoustical field in an ideal fluid," *Soviet Physics-Doklady*, 1962, **6**, 773-775.

[20] W.L. Nyborg, "Radiation pressure on a small rigid sphere," *J. Acoust. Soc. Am.*, 1967, **42**, 947-952.

[21] A. Eller, "Force on a bubble in a standing acoustic wave," *J. Acoust. Soc. Am.*, 1968, **43**, 170-171.

[22] L. A. Crum, "Acoustic force on a liquid droplet in an acoustic stationary wave," *J. Acoust. Soc. Am.*, 1971, **50**, 157-163.

[23] A. A. Doinikov, "Acoustic radiation pressure on a compressible sphere in a viscous fluid," *J. Fluid Mech.*, 1994, **267**, 1-22.

[24] A. A. Doinikov, "Acoustic radiation force on a spherical particle in a viscous heat-conducting fluid. I. General formula," *J. Acoust. Soc. Am.*, 1997, **101**, 713-721.

[25] M. Settnes and H. Bruus, "Forces acting on a small particle in an acoustical field in a viscous fluid," *Phy. Rev. E,* 2012, **85**, 016327.

[26] S.M. Hagsäter, A. Lenshof, P. Skafte-Pedersen, J.P. Kutter, T. Laurell, and H. Bruus, "Acoustic resonances in straight micro channels: Beyond the 1D-approximation," *Lab Chip,* 2008, **8**, 1178-1184.

[27] H. Bruus, *Theoretical microfluidics*, Oxford University Press, Oxford, UK, 2008, 19-27, 255-271.

[28] M.F. Hamilton and D.T. Blackstock, *Nonlinear acoustics*, Academic Press, San Diego, California, USA, 1998, 25-37, 279-284.

[29] M. Wiklund, R. Green, and M. Ohlin, "Acoustofluidics 14: Applications of acoustic streaming in microfluidic devices," *Lab Chip*, 2012, **12**, 2438-2451.

[30] L. Rayleigh, "On the circulation of air observed in Kundt's tubes, and some allied acoustical problems," *Philos. Trans. R. Soc. London*, 1884, **175**, 1-21.

[31] H. Schlichting, "Berechnung ebener periodischer grenzschichtstromungen (calculation of plane periodic boundary layer streaming)," *Physikalische Zeitschrift*, 1932, **33**, 327-335.

[32] P. J. Westervelt, "The theory of steady rotational flow generated by a sound field," *J. Acoust. Soc. Am.*, 1953, **25**, 60-67.

[33] W. L. Nyborg, "Acoustic streaming near a boundary," *J. Acoust. Soc. Am.*, 1958, **30**, 329-339.

[34] M. F. Hamilton, Y. A. IIinskii, and E. A. Zabolotskaya, "Acoustic streaming generated by standing waves in two-dimensional channels of arbitrary width," *J. Acoust. Soc. Am.*, 2003, **113**, 153-160.

[35] M. F. Hamilton, Y. A. Ilinskii, and E. A. Zabolotskaya, "Thermal effects on acoustic streaming in standing waves," *J. Acoust. Soc. Am.*, 2003, **114**, 3092-3101.

[36] P. B. Muller, *Acoustofluidics in microsystems: investigation of acoustic streaming*, Master Thesis, Department of Micro- and Nanotechnology, Technical University of Denmark, Copenhagen, Denmark, 2012.

[37] S.M. Hägsater, T.G. Jensen, H. Bruus, and J.P. Kutter, "Acoustic resonances in microfluidic chips: full-image micro-PIV experiments and numerical simulations," *Lab Chip*, 2007, **7**, 1336-1344.

[38] B. Gustafsson, *High order difference methods for time dependent PDE*, Springer Verlag, Berlin, Germany, 2008, 81-114.

[39] P. B. Muller, R. Barnkob, M. J. H. Jensen, and H. Bruus, "A numerical study of microparticle acoustophoresis driven by acoustic radiation forces and streaming-induced drag forces," *Lab Chip*, 2012, **12**, 4617-4627.

[40] H. Lamb, *Hydrodynamics*, Dover Publications, New York, USA, 1945, 473-475.

[41] E. Ackerman, "Resonances of biological cells at audible frequencies," *Bull. Math. Biophys.*, 1951, **13**, 93-106.

[42] E. Ackerman, "An extension of the theory of resonances of biological cells I effects of viscosity and compressibility," *Bull. Math. Biophys.*, 1954, **16**, 141-150.

[43] E. Ackerman, "Mechanical resonances of amphiuma erythrocytes," *J. Acoust. Soc. Am.*, 1954, **26**, 257-258.

[44] W. H. Reid, "The oscillations of a viscous liquid drop," *Quart. Appl. Math.*, 1960, **18**, 86-89.

[45] C. A. Miller and L. E. Scriven, "The oscillations of a fluid droplet immersed in another fluid," *J. Fluid Mech.*, 1968, **32**, 417-435.

[46] E. A. Evans and R. M. Hochmuth, "Membrane viscoelasticity," *Biophys. J.*, 1976, **16**, 1-11.

[47] R. M. Hochmuth, P. R. Worthy, and E. A. Evans, "Red cell extensional recovery and the determination of membrane viscosity," *Biophys. J.*, 1979, **26**, 101-114.

[48] E. A. Evans and R. Skalak, *Mechanics and thermodynamics of biomembrane*, CRC Press, Boca Raton, Florida, USA, 1980.

[49] P. V. Zinin, V. M. Levin, and R. G. Mayev, "Natural oscillations of biological microspecimens," *Biophys. J.* , 1987, **32**, 202-210.

[50] P. V. Zinin, J. S. A. III, and V. M. Levin, "Mechanical resonances of bacteria cells," *Phys. Rev. E*, 2005, **72**, 061907.

[51] L. H. Ford, "Estimate of the vibrational frequencies of spherical virus particles," *Phys. Rev. E*, 2003, **67**, 051924.

[52] Y.-H. Pao and C.-C. Mow, *Diffraction of elastic waves and dynamic stress concentrations*, Crane Russak, New York, USA, 1973, 45, 49, 600-625.

[53] M. L. Rodriguez, P. J. McGarry, and N. J. Sniadecki, "Review on cell mechanics experimental and modeling approaches," *Appl. Mech. Rev.*, 2013, **65**, 06080-1-41.

[54] W. P. Raney, J. C . Corelli, and P. J. Westervelt, "Acoustical streaming in the vicinity of a cylinder," *J. Acoust. Soc. Am.*, 1954, **26**, 1006-1014.

[55] J. Holtsmark, I. Johnsen, T. Sikkeland, and S. Skavlem, "Boundary layer flow near a cylindrical obstacle in an oscillating incompressible fluid, " *J. Acoust. Soc. Am.*, 1954, **26**, 26-39.

[56] C. A. Lane, "Acoustical streaming in the vicinity of a sphere," *J. Acoust. Soc. Am.*, 1955, **27**, 1082-1086.

[57] C.-Y. Wang, "The flow field induced by an oscillating sphere," *J. Sound Vib.*, 1965, **2**, 257-269.

[58] N. Riley, "On a sphere oscillating in a viscous liquid," *Q. J. Mech. Appl. Math.*, 1966, **19**, 461-472.

[59] C. P. Lee and T. G. Wang, "Near-boundary streaming around a small sphere due to two orthogonal standing waves," *J. Acoust. Soc. Am.*, 1989, **85**, 1081-1088.

[60] C. P. Lee and T. G. Wang, "Outer acoustic streaming," *J. Acoust. Soc. Am.*, 1990, **88**, 2367-2375.

[61] H. Zhao, S. S. Sadhal, and E. H. Trinh, "Internal circulation in a drop in an acoustic field," *J. Acoust. Soc. Am.*, 1999, **106**, 3289-3295.

[62] A. Y. Rednikov, H. Zhao, and S. S. Sadhal, "Steady streaming around a spherical drop displaced from the velocity antinode in an acoustic levitation field," *Q. J. Mech. Appl. Math.*, 2006, **59**, 377-397.

[63] A. A. Doinikov and A. Bouakaz, "Acoustic microstreaming around a gas bubble," *J. Acoust. Soc. Am.*, 2009, **127**, 703-709.

[64] A. A. Doinikov and A. Bouakaz, "Acoustic microstreaming around an encapsulated particle," *J. Acoust. Soc. Am.*, 2010, **127**, 1218-1227.

[65] P. L. Marston and R. E. Apfel, "Acoustically forced shape oscillation of hydrocarbon drops levitated in water," *J. Colloid Interface Sci.*, 1979, **68**, 280-286.

[66] P. L. Marston and R. E. Apfel, "Quadrupole resonance of drops driven by modulated acoustic radiation pressure-experimental properties," *J. Acoust. Soc. Am.*, 1980, **67**, 27-37.

[67] A. E. Pelling, S. Sehati, E. B. Gralla, J. S. Valentine, and J. K. Gimzewski, "Local nanomechanical motion of the cell wall of saccharomyces cerevisiae," *Science*, 2004, **305**, 1147-1150.

[68] F. Jelinek, J. Pokorny, J. Vanis, J. Hasek, and J. Simsa, "Measurement of electrical and mechanical oscillations of yeast cells membrane in acoustic frequency range," *14th Conference on Microwave Techniques*, 2008, Prague, Czech Republic.

[69] M. Radmacher, M. Fritz, C. M. Kacher, J. P. Cleveland and P. K. Hansma, "Measuring the viscoelastic properties of human platelets with the atomic force microscope, " *Biophys. J.*, 1996, **70**, 556-567.

[70] G. W. Schmidschonbein, K. L. P. Sung, H. Tozeren, R. Skalak and S. Chien, "Passive mechanical properties of human leukocytes, " *Biophys. J.*, 1981, **36**, 243-256.

[71] S. Henon, G. Lenormand, A. Richert and F. Gallet, "A new determination of the shear modulus of the human erythrocyte membrane using optical tweezers," *Biophys. J.*, 1999, **76**, 1145-1151.

[72] N. Wang, J. P. Butler, and D. E. Ingber, "Mechanotransduction across the cell surface and through the cytoskeleton," *Science*, 1993, **260**, 1124-1127.

[73] M. A. H. Weiser and R. E. Apfel, "Extension of acoustic levitation to include the study of micro-size particles in a more compressible host liquid," *J. Acoust. Soc. Am.*, 1982, **71**, 1261-1268.

[74] D. Hartono, Y Liu, P. L. Tan, X. Y. S. Then, L.-Y. L. Yung and K.-M. Lim, "On-chip measurements of cell compressibility via acoustic radiation," *Lab Chip*, 2011, **11**, 4072-4080.

[75] R. Barnkob, P. Augustsson, T. Laurell and H. Bruus, "Measuring the local pressure amplitude in microchannel acoustophoresis," *Lab Chip*, 2010, **10**, 563-570.

[76] R. Barnkob, P. Augustsson, C. Magnusson, H. Lilja, T. Laurell and H. Bruus, "Measuring density and compressibility of white blood cells and prostate cancer cells by microchannel acoustophoresis," *15th International Conference on Miniaturized Systems for Chemistry and Life Sciences*, 2011, Seattle, Washington, USA.

[77] W. M. Haynes, *CRC handbook of chemistry and physics*, CRC Press, Cleveland, Ohio, USA, 2012, 6-1-251.

[78] Reddy, *An introduction to the finite element method*, McGraw-Hill, New York, USA, 1993, 404-429.

[79] M. Farrashkhalvat, J. P. Miles, *Basic structured grid generation with an introduction to unstructured grid generation*, Butterworth-Heinemann, Boston, Massachusetts, USA, 2003, 76-108.

[80] X. Yu, W. Weng, P.A. Taylor and D. Liang, "Relaxation factor effects in the non-linear mixed spectral finite difference model of flow over topographic features," *Bound.-Layer Meteor.*, 2011, **140**, 23-35.

[81] H. Wang, Z. Liu, S. Kim, C. Koo, Y. Cho, D. Jang, Y.-J. Kim and A. Han, "Microfluidic acoustophoretic force based low-concentration oil separation and detection from the environment," *Lab Chip*, 2013, **14**, 947-956.

[82] J.-H. Han, Y.-J. Kim, and M. Karkoub, "Modeling of wave propagation in drill strings using vibration transfer matrix method," *J. Acoust. Soc. Am.*, 2013, **134**, 1920-1931.

[83] M. E. Dokukin, N. V. Guz and I. Sokolov, "Quantitative study of the elastic modulus of loosely attached cells in AFM indentation experiments," *Biophys. J.*, 2013, **104**, 20123-2131.

[84] S. Chandrasekhar, *Hydrodynamic and hydromagnetic stability*, Cambridge University Press, Oxford, UK, 1961, 222-223.

[85] http://www-mdp.eng.cam.ac.uk/web/library/enginfo/cueddatabooks/materials.pdf

[86] J. Happel and H. Brenner, *Low Reynolds number hydrodynamics*, Martinus Nijhoff Publishers, Boston, USA, 1983, 235-285, 286-357.

[87] P. Ganatos, R. Pfeffer and S. Weinbaum, "A strong interaction theory for the creeping motion of a sphere between plane parallel boundaries. Part 2. Parallel motion," *J. Fluid Mech.*, 1980, **99**, 755-783.

[88] L. Lobry and N. Ostrowsky, "Diffusion of brownian particles trapped between two walls: Theory and dynamic-light-scattering measurements," *Phys. Rev. B*, 1996, **53**, 12050-12056.

[89] https://www.americanpiezo.com/apc-materials/piezoelectric-properties.html

[90] http://en.wikipedia.org/wiki/Polydimethylsiloxane

[91] I. D. Johnston, D. K. McCluskey, C. K. L. Tan and M. C. Tracey, "Mechanical characterization of bulk Sylgard 184 for microfluidics and microengineering," *J. Micromech. Microeng.*, 2014, **24**, 035017.

[92] S. Suresh, "Biomechanics and biophysics of cancer cells," *Acta Mater.*, 2007, **55**, 3989-4014.

[93] Y. Chen and S. Lee, "Manipulation of biological objects using acoustic bubbles: a review," *Integr. Comp. Biol.*, 2014, **54**, 959-68.

[94] Y. Xu, A. Hashmi, G. Yu, X. Lu, H.-J. Kwon, X. Chen, J. Xu, "Microbubble array for on-chip worm processing," *Appl. Phys. Lett.*, 2013, **102**, 023702.

[95] S. Chung and S. Cho, "On-chip manipulation of objects using mobile oscillating bubbles," *J. Micromech. Microeng.*, 2008, **18**, 125024.

[96] T. Tandiono, D. S.-W. Ow, L. Driessen, C.-H. Chin, E. Klaseboer, A.-H. Choo, W.-W. Ohl, C.-D. Ohl, "Sonolysis of escherchia coli and pichia pastoris in microfluidics," *Lab Chip*, 2012, **12**, 780-786.

[97] P. Marmottant and S. Hilgenfeldt, "Controlled vesicle deformation and lysis by single oscillating bubbles," *Nature*, 2003, **423**, 153-156.

[98] Ponder, "The relationship between red blood cell density and corpuscular hemoglobin concentration," *J. Biol. Chem.*, 1942. **144**, 333-338.

[99] K. Astafyeva et al., "Properties of theranostic nanoparticles determined n suspension by ultrasonic spectroscopy," *Phys. Chem. Chem. Phys.*, 2015, **17**, 25483.

[100] P. Gentile et al, "An overview of poly(lactic-coglycolic) acid(PLGA)-based biomaterials for bone tissue engineering," *Int. J. Mol. Sci.*, 2014, **15**, 3640-3659.

[101] Z. Liu, H. Wang, A. Han and Y.-J. Kim, "Effects of fluid medium flow and spatial temperature variation on acoustophoretic motion of microparticles in microfluidic channels," *J. Acoust. Soc. Am.*, 2016, **139**, 332-349. Copyright 2016 Acoustical Society of America.

[102] Z. Liu and Y.-J. Kim, "Acoustic streaming around a spherical microparticle/cell under ultrasonic wave excitation," *Proceedings of Inter-Noise 2015,* San Francisco, California, USA, 2015. Copyright 2015 Institute of Noise Control Engineering of USA.

APPENDIX A

TRANSFORM OF EQ. (2.10b) TO EQ. (2.11b)

For the linear terms, the following equation is obtained as

$$\frac{\partial \rho_1}{\partial t} = -\rho_0 \vec{\nabla} \cdot \mathbf{v}_1 . \tag{A.1}$$

Therefore, the second term in RHS of Eq. (2.10b) is converted as

$$\left\langle \rho_1 \frac{\partial \mathbf{v}_1}{\partial t} \right\rangle = -\left\langle \mathbf{v}_1 \frac{\partial \rho_1}{\partial t} \right\rangle = \left\langle \rho_0 \mathbf{v}_1 \left(\vec{\nabla} \cdot \mathbf{v}_1 \right) \right\rangle . \tag{A.2}$$

Taking curl on both sides of Eq. (2.10b), the terms in LHS are processed as

$$\vec{\nabla} \times \nabla p_{20} = \mathbf{0} , \tag{A.3a}$$

$$\vec{\nabla} \times \eta \nabla^2 \mathbf{v}_{20} = \eta \nabla^2 \left(\vec{\nabla} \times \mathbf{v}_{20} \right), \tag{A.3b}$$

$$\vec{\nabla} \times \beta \eta \nabla \left(\vec{\nabla} \cdot \mathbf{v}_{20} \right) = \mathbf{0} . \tag{A.3c}$$

Considering Eq. (A.3), Eq. (2.11b) is obtained.

APPENDIX B

CHARACTERISTIC EQUATION OF COMPLEX FLUID MODEL

By setting $z_o = k_o a$, $z_i = k_i a$, $\xi_i = \chi_i a$, $\xi_o = \chi_o a$, the characteristic equation can be expressed as

$$\begin{bmatrix} z_o h_n^{'}(z_o) & g_f^{12} & -z_i j_n^{'}(z_i) & g_f^{14} \\ h_n(z_o) & g_f^{22} & -j_n(z_i) & g_c^{24} \\ g_f^{31} & g_f^{32} & g_f^{33} & g_f^{34} \\ g_f^{41} & g_f^{42} & g_f^{43} & g_f^{44} \end{bmatrix} \begin{bmatrix} B_n \\ C_n \\ D_n \\ E_n \end{bmatrix} = -A_n \begin{bmatrix} z_o j_n^{'}(z_o) \\ j_n(z_o) \\ b_f^3 \\ b_f^4 \end{bmatrix} \tag{B.1}$$

where

$$g_f^{12} = -n(n+1) h_n(\xi_o)$$

$$g_f^{14} = n(n+1) j_n(\xi_i)$$

$$g_f^{22} = -\left[h_n(\xi_o) + \xi_o h_n^{'}(\xi_o) \right]$$

$$g_f^{24} = j_n(\xi_i) + \xi_i j_n^{'}(\xi_i)$$

$$g_f^{31} = -\left(\frac{i\rho_o c_o^2 z_o^2}{\omega} + (\beta_o - 1)\eta_o z_o^2 \right) h_n(z_o) + 2\eta_o z_o^2 h_n^{''}(z_o)$$

$$g_f^{32} = 2n(n+1)\eta_o \left[h_n(\xi_o) - \xi_o h_n^{'}(\xi_o) \right]$$

$$g_f^{33} = \left(\frac{i\rho_i c_i^2 z_i^2}{\omega} + (\beta_i - 1)\eta_i z_i^2 + n(n+1)\frac{i2K_A}{\omega a} \right) j_n(z_i) + \left(\frac{2T_o - 4K_A}{a}\frac{iz_i}{\omega} - n(n+1)\frac{T_0}{a}\frac{iz_i}{\omega} \right) j_n^{'}(z_i) - 2\eta_i z_i^2 j_n^{''}(z_i)$$

$$g_f^{34} = n(n+1)\left(-i\frac{2T_o - 2K_A}{\omega a} + i\frac{T_0}{\omega a}n(n+1) - 2\eta_i\right) j_n(\xi_i)$$
$$+n(n+1)\left(2\eta_i\xi_i - \frac{i2K_A\xi_i}{\omega a}\right) j_n'(\xi_i)$$

$$g_f^{41} = -2\eta_o h_n(z_o) + 2\eta_o z_o h_n'(z_o)$$

$$g_f^{42} = -(n-1)(n+2)\eta_o h_n(\xi_o) - \eta_o \xi_o^2 h_n''(\xi_o)$$

$$g_f^{43} = \left(2\eta_i - i\frac{K_A + 2\mu}{\omega a}n(n+1) + i\frac{2\mu}{\omega a}\right) j_n(z_i) - \left(2\eta_i - \frac{i2K_A}{\omega a}\right) z_i j_n'(z_i)$$

$$g_f^{44} = \left[n(n+1)\left(\eta_i - i\frac{K_A - 2\mu}{\omega a}\right) - 2\eta_i - i\frac{2\mu}{\omega a}\right] j_n(\xi_i)$$
$$+\left[n(n+1)i\frac{K_A + 2\mu}{\omega a} - i\frac{2\mu}{\omega a}\right] \xi_i j_n'(\xi_i) + \eta_i \xi_i^2 j_n''(\xi_i)$$

$$b_f^3 = -\left(\frac{i\rho_o c_o^2 z_o^2}{\omega} + (\beta_o - 1)\eta_o z_o^2\right) j_n(z_o) + 2\eta_o z_o^2 j_n''(z_o)$$

$$b_f^4 = -2\eta_o j_n(z_o) + 2\eta_o z_o j_n'(z_o)$$

APPENDIX C

CHARACTERISTIC EQUATION OF SOLID ELASTIC SPHERE

By setting $z_o = k_o a$, $z_i = k_i a$, $\xi_i = \chi_i a$, $\xi_o = \chi_o a$, the characteristic equation can be expressed as

$$\begin{bmatrix} z_o h_n^{'}(z_o) & g_s^{12} & i\omega z_i j_n^{'}(z_i) & g_s^{14} \\ h_n(z_o) & g_s^{22} & i\omega j_n(z_i) & g_s^{24} \\ g_s^{31} & g_s^{32} & g_s^{33} & g_s^{34} \\ g_s^{41} & g_s^{42} & g_s^{43} & g_s^{44} \end{bmatrix} \begin{bmatrix} B_n \\ C_n \\ D_n \\ E_n \end{bmatrix} = -A_n \begin{bmatrix} z_o j_n^{'}(z_o) \\ j_n(z_o) \\ b_s^3 \\ b_s^4 \end{bmatrix} \tag{C.1}$$

where

$$g_s^{12} = -n(n+1)h_n(\xi_o)$$

$$g_s^{14} = -i\omega n(n+1)\, j_n(\xi_i)$$

$$g_s^{22} = -h_n(\xi_o) - \xi_o h_n^{'}(\xi_o)$$

$$g_s^{24} = -i\omega j_n(\xi_i) - i\omega\xi_i j_n^{'}(\xi_i)$$

$$g_s^{31} = \left(-\frac{i\rho_0 c_0^2 z_o^2}{\omega} - (\beta+1)\eta z_o^2 + 2\eta n(n+1) \right) h_n(z_o) - 4\eta z_o h_n^{'}(z_o)$$

$$g_s^{32} = 2\eta n(n+1)h_n(\xi_o) - 2\eta n(n+1)\xi_o h_n^{'}(\xi_o)$$

$$g_s^{33} = \left[(\lambda + 2\mu) z_i^2 - 2\mu n(n+1) \right] j_n(z_i) + 4\mu z_i j_n^{'}(z_i)$$

$$g_s^{34} = -2\mu n(n+1)\, j_n(\xi_i) + 2\mu n(n+1)\xi_i j_n^{'}(\xi_i)$$

$$g_s^{41} = 2\eta z_o h_n^{'}(z_o) - 2\eta h_n(z_o)$$

$$g_s^{42} = \left[-2\eta\left(n^2 + n - 1\right) + \eta\xi_o^2 \right] h_n\left(\xi_o\right) + 2\eta\xi_o h_n^{'}\left(\xi_o\right)$$

$$g_s^{43} = -2\mu z_i j_n^{'}\left(z_i\right) + 2\mu j_n\left(z_i\right)$$

$$g_s^{44} = \left[2\mu\left(n^2 + n - 1\right) - \mu\xi_i^2 \right] j_n\left(\xi_i\right) - 2\mu\xi_i j_n^{'}\left(\xi_i\right)$$

$$b_s^3 = \left[-\frac{i\rho_0 c_0^2 z_o^2}{\omega} - \left(\beta + 1\right)\eta z_o^2 + 2\eta n\left(n+1\right) \right] j_n\left(z_o\right) - 4\eta z_o j_n^{'}\left(z_o\right)$$

$$b_s^4 = 2\eta z_o j_n^{'}\left(z_o\right) - 2\eta j_n\left(z_o\right)$$

APPENDIX D

SOLUTION TO HOMOGENEOUS BIHARMONIC EQUATION

The Biharmonic Equation for a vector is presented as

$$\nabla^2\nabla^2\mathbf{\Psi} = \mathbf{0}\,. \tag{D.1}$$

For a vector $\mathbf{g}(z)$, the solution to $\nabla^2\mathbf{g}(z) = \mathbf{0}$ can be expressed as

$$\mathbf{g}(z) = \hat{i}_\phi \sum_{n=0}^{\infty}\left(d_{1n}z^n + d_{2n}z^{-(n+1)}\right)P_n^1(\cos\theta), \tag{D.2}$$

where d_1 and d_2 are the expansion coefficients. Therefore, the solution of Eq. (D.1) can be expressed as

$$\nabla^2\mathbf{\Psi} = \hat{i}_\phi \sum_{n=0}^{\infty}\left(d_{1n}z^n + d_{2n}z^{-(n+1)}\right)P_n^1(\cos\theta), \tag{D.3}$$

and the function $\mathbf{\Psi}$ is expanded in associated Legendre polynomials as

$$\mathbf{\Psi} = \vec{e}_\phi \sum_{n=0}^{\infty}\psi_n P_n^1(\cos\theta)\,. \tag{D.4}$$

The substitution of Eq. (D.4) into Eq. (D.3) gives

$$\frac{d^2\psi_n}{dz^2} + \frac{2}{z}\frac{d\psi_n}{dz} - \frac{n(n+1)\psi_n}{z^2} = \frac{1}{a^2}\left(d_{1n}z^n + d_{2n}z^{-(n+1)}\right). \tag{D.5}$$

By using the results in Appendix E, the function $\psi_n(z)$ is solved as

$$\psi_n = z^{-(n+1)}\left(-\int \frac{z^{n+2}}{2n+1}\left(d_{1n}z^n + d_{2n}z^{-(n+1)}\right)dz - d_{3n}\right) + z^n\left(\int \frac{z^{-(n-1)}}{2n+1}\left(d_{1n}z^n + d_{2n}z^{-(n+1)}\right)dz - d_{4n}\right). \tag{D.6}$$

By expanding the integral and collecting the coefficients of z, the final expression is obtained as

$$\psi_n = C_{1n}z^{-(n-1)} + C_{2n}z^{-(n+1)} + C_{3n}z^n + C_{4n}z^{n+2}, \tag{D.7}$$

where the C_{1n}, C_{2n}, C_{3n} and C_{4n} are the unknown coefficients. In Eq. (D.3), d_{1n} and d_{2n} are included in these unknown coefficients.

APPENDIX E

SOLUTION TO ORDINARY DIFFERENTIAL EQUATIONS

The ordinary differential equation is generalized as

$$f'' + \frac{2}{z} f' - \frac{n(n+1)}{z^2} f = g(z), \tag{E.1}$$

where $f(z)$ is the unknown function and $g(z)$ is a known (or excitation) function. The two fundamental solutions for the homogeneous equation of Eq. (E.1) is

$$f_1 = z^{-(n+1)}, \quad f_2 = z^n, \tag{E.2}$$

where f_1 and f_2 are the general solutions. The particular solution is then expressed as

$$f_p = u_1(z) z^{-(n+1)} + u_2(z) z^n. \tag{E.3}$$

The derivative of f_p is expressed as

$$f_p' = u_1' z^{-(n+1)} - (n+1) u_1 z^{-(n+2)} + u_2' z^n + n u_2 z^{n-1}. \tag{E.4}$$

Here, it is set that

$$u_1' z^{-(n+1)} + u_2' z^n = 0. \tag{E.5}$$

Then, Eq. (E.4) is rewritten as

$$f_p' = -(n+1) u_1 z^{-(n+2)} + n u_2 z^{n-1}. \tag{E.6}$$

The second derivative of f_p is

$$f_p'' = -(n+1) u_1' z^{-(n+2)} + (n+1)(n+2) u_1 z^{-(n+3)} + n u_2' z^{n-1} + (n-1) n u_2 z^{n-2}. \tag{E.7}$$

The substitution of Eqs. (E.3), (E.6) and (E.7) into Eq. (E.1) results in

$$-\left(n+1\right)u_1^{'}z^{-\left(n+2\right)}+nu_2^{'}z^{-\left(n+3\right)}=g\left(z\right). \tag{E.8}$$

By considering Eqs. (E.5) and (E.8), the expression for $u_1(z)$ and $u_2(z)$ are determined as

$$u_1=-\int\frac{z^{n+2}}{2n+1}g\left(z\right)dz \text{ and } u_2=-\int\frac{z^{-\left(n-1\right)}}{2n+1}g\left(z\right)dz\,. \tag{E.9}$$

By considering the particular solution Eqs. (E.2) and (E.9), the expression of $f(z)$ is obtained as

$$\begin{aligned} f\left(y\right)&=z^{-\left(n+1\right)}\left[u_1\left(z\right)-C_1\right]+z^n\left[u_2\left(z\right)-C_2\right]\\ &=z^{-\left(n+1\right)}\left(-\int\frac{z^{n+2}}{2n+1}g\left(z\right)dz-C_1\right)+z^n\left(\int\frac{z^{-\left(n-1\right)}}{2n+1}g\left(z\right)dz-C_2\right), \end{aligned} \tag{E.9}$$

where C_1 and C_2 are unknown coefficients to be determined from the boundary conditions.

APPENDIX F

IN-HOUSE PROGRAM OF TRAJECTORY EXTRACTION

In the experiment, the motion of cell/microparticle is recorded as a serial of images in the format of “jpg”, “tiff” and so on. The in-house program is built by using Matlab and it consists two programs: one is for manual trajectory extraction and the other is for automatic trajectory extraction. The manual program is recommended since it gives smoother trajectories compared with automatic one. This instruction should be read with the in-house programs.

In the manual program, the display of the image is based on the size of your screen so some parameters needs to be adjusted. First of all, make sure that the names of your images are consistent for easy read. For example, Image_1, Image_2, Image_3, and so on. Before running the code, some parameters need to be determined: the file path of those images and the channel lower and upper boundaries in the unit of pixel. Both jobs are done manually. After running the code, there is an image displayed in the screen with a blue circle. Here, the blue circle is used to locate the position of the target cell/microparticle, and it can be moved using mouse or arrow key. The mouse is for coarse movement while the arrow keys are for fine movement. Use the mouse to drag the circle to the target cell/microparticle, then press “Enter” to confirm the location. Then the image is switched to a new one as following. Next, use arrow keys to move the blue circle and then press “Enter” to confirm the position again. Repeat the procedure again and again until the required trajectory is completed. Then, press “ESC” to escape

the code and the trajectories is automatically saved into the same folder.

For the automatic program, it requires that the image must be very clear. Then the file path and the channel boundary need to be entered into the code. To detect the cell/microparticle, the upper and lower limits of cell/microparticle radius are required. The cutoff threshold is estimated to convert the raw colorful images into black and white images. The maximum missing step, minimum data point number, maximum movement in the *x*-direction are also required. Then, run the code. Several trajectories are display while a dialog shows up to let you enter the trajectories to be saved. Enter the number and press the "Enter" and the trajectories are saved. It seems that the automatic program saves time. However, the parameters listed above have to be adjusted a few time to get a reasonable trajectory and sometimes it is difficult to obtain good trajectories.